The virtual knife

Hansen, Mads Fogtmann

Publication date:
2009

Document Version
Publisher's PDF, also known as Version of record

The Virtual Knife

Mads Fogtmann Hansen

Kongens Lyngby 2009
IMM-PHD-2009-213

Technical University of Denmark
Informatics and Mathematical Modelling
Building 321, DK-2800 Kongens Lyngby, Denmark
Phone +45 45253351, Fax +45 45882673
reception@imm.dtu.dk
www.imm.dtu.dk

IMM-PHD: ISSN 0909-3192

Abstract

Since post World War II and until 2008 the Danish pig producing industry (DPPI) has been in a continuing state of growth. In spite of an ever fiercer competition DPPI has managed to protect its position as export leader by maintaining a focus on research and development. Today, DPPI is in a state of recession and must increase the efficiency if not to reduce the production capacity further.

The industry recognizes that a more efficient use of the raw materials is one of the largest and most important challenges. To meet this challenge it is a necessity to get a better understanding of the biological variation of pigs. The development of models for describing the biological variation of pigs is one of the key components needed to attain a better sorting of the pig carcasses and an improved cutting in the abattoirs. Such models can be related to possible products, which can be related to potential yield and order books.

The Danish Meat Research Institute (DMRI) is currently constructing a representative database of virtual representations of pigs using X-ray Computed Tomography (CT). The database will serve as the foundation for the diversity modeling of pigs and for extracting predictors of quality and optimal use.

This thesis integrates well-known techniques from the medical image analysis into the development of tools for automated analysis of the morphology of pigs. E.g. elastic image matching has been applied to establish spatial correspondence between the virtual representations of pigs in the database. The establishment of spatial correspondence is an essential preprocessing step for most automated analysis using the database.

The main application of the thesis is a so-called cutting atlas which provides the functionality to construct combination of virtual cuts on the virtual representations of pigs. The cutting atlas application uses the spatial normalization to transfer anatomical information from a reference pig to the entire database of pigs, which are subsequently used to guide the virtual cuts. The ability to consistently perform and experiment with virtual cuts on a representative set of pigs provide the link between biological variation and possible product ranges. The thesis also provides a pilot study on evaluation of the consistency between virtual products and real products. A cutting atlas is of little value unless the virtual cuts resemble the real cuts from the abattoirs.

As a final note, the thesis contains a fairly comprehensive chapter on image registration with an emphasis on elasticity and a number of image registration papers, which may be interesting for readers outside the pig and food industry.

Resume

Den danske svineindustri (DSI) har siden anden verdenskrig og indtil 2008 været i konstant vækst. På trods af en voksende konkurrence har DSI formået at forsvare sin position som førende eksportør ved en løbende satsning på forskning og udvikling. Vækst er i dag erstattet med recession, og DSI er derfor nødsaget til at øge effektiviteten, hvis produktion ikke skal sænkes ydereligere.

Det er anerkendt i branchen, at en af de primære udfordringer ligger i en forbedring af udnyttelsen af råmaterialet. For at imødekomme denne udfordring er det en nødvendighed, at der opnås en bedre forståelse for den biologiske variation i svin. Udviklingen af modeller, som kan beskrive denne variation, er en af nøglekomponenterne for at opnå forbedret sortering af slagtekroppe samt en mere optimal udskæring på slagterierne. Disse modeller kan relateres til mulige produkter, som kan relateres til afkast og ordrebøger.

Slagteriens forskningsinstitut er p.t. i gang med at skabe en database af virtuelle repræsentationer af svin vha. røntgen Computer Tomografi (CT). Denne database skal udgøre det datamæssige grundlag for konstruktionen af modeller af den biologiske variation i svin samt udtrækning af prædiktorer for kvalitet og optimal udnyttelse af råmateriale.

Denne afhandling benytter anerkendte metoder fra medicinsk billedanalyse i udviklingen af værktøjer til automatisk form-analyse af svin. For eksempel er billedregistering blevet anvendt til at opnå rumlig korrespondence mellem de virtuelle repræsentationer af svin.

Den primære applikation i denne afhandling er et såkaldt skæreatlas, som kan udføre virtuelle udskæringer på de virtuelle repræsentationer af svin. Skæreat-

lasset benytter den rumlige normalisering til at overføre anatomisk viden fra et referencesvin til databasen af svin, som dernæst bruges til at styre den virtuelle udskæring. Muligheden for at udføre og eksperimentere konsistent med virtuelle udskæringer på en representativ mængde af svin bygger bro mellem biologisk variation og mulige produkter. Desuden indeholder denne afhandling et indledende forsøg, som omhandler sammenligning af virtuelle og virkelige produkter. Et skæreatlas er af ringe værdi, hvis de virtuelle udskæringer ikke ligner de virkelige udskæringer fra slagterierne.

Til sidst skal det nævnes, at denne afhandling indeholder et omfangsrigt kapitel om billedregistrering med fokus på elasticitet og flere artikler om billedregistrering, der kan være interessante for læsere udenfor svin- og fødevareindustrien.

Preface

This thesis was prepared at the Image Analysis and Computer Graphics group at DTU Informatics (IMM) and submitted to the Technical University of Denmark in partial fulfilment of the requirements for the degree of Doctor of Philosophy in Informatics and Mathematical Modeling. The project was funded by DTU, the Virtual Slaughterhouse project and the ITMAN Graduate School programme.

The work herein represents selected parts of the research work carried out in the Ph.D. period. The thesis consists of an introductory part and six research papers. The reader is expected to have skills in linear algebra, mathematics, statistics and optimization on a basic university level to get a complete understanding of the covered material.

The work was carried out in a close collaboration with the Danish Meat Research Institute (DMRI) of the Danish Meat Association. Part of the research was conducted at the University of California, San Francisco, USA, under the supervision of Associate Professor Colin Studholme. The project was supervised by Professor Rasmus Larsen, IMM, and Ph.D. Lars Bager Christensen, DMRI.

The 2nd edition differs from the 1st edition by having fewer spelling errors, a revised bibliography and some corrections to the formulas. A larger revision, which includes the comments the assessment committee, remains a project of the future.

Kgs. Lyngby, April 2010

Mads Fogtmann Hansen

List of Published Papers

Listed here are peer-reviewed scientific papers, technical reports and abstracts prepared during the course of the Ph.D. program.

Journal papers:

- M. Vester-Christensen, S. G. H. Erbou, M. F. Hansen, E. V. Olsen, L. B. Christensen, M. Hviid, B. K. Ersbøll, R. Larsen Virtual Dissection of Pig Carcasses. Meat Science. 2008.

Conference papers:

- M. F. Hansen, R. Larsen, B. Ersbøll, L. B. Christensen. Coupled Shape Model Segmentation of Pig Carcasses,. *ICPR*. 2006.
- M. F. Hansen, S. G. Erbou, M. Vester-Christensen, R. Larsen, L. B. Christensen. Surface-to-surface registration using level sets. *Scandinavian Conference on Image Analysis - SCIA*. 2007.
- M. F. Hansen, R. Blas, M R. Larsen. Mahalanobis Distance Based Iterative Closest Point. *SPIE Medical Imaging*. 2007.
- M. S. Hansen, M. F. Hansen, R. Larsen. Diffeomorphic Statistical Deformation Models. *ICCV, Workshop NRTL*. 2007.
- M. F. Hansen, M. S. Hansen, R. Larsen. Conditional Statistical model building. *SPIE Medical Imaging*. 2008.

- K. Kim, M. F. Hansen, P. A. Habas, F. Rousseau, O. A. Glenn, A. J. Barkovich, C. Studholme. Intersection-based registration of slice stacks to form 3D images of the human fetal brain. 5th IEEE International Symposium on Biomedical Imaging. 2008.
- M. F. Hansen, Jacob Andreas Bærentzen R. Larsen. Generating Quality Tetrahedral Meshes from Binary Volumes. *VISAPP*. 2009.

Technical reports:

- M. F. Hansen, L. B. Christensen, R. Larsen, Virtual Cutting Atlas. DTU Informatics, Technical University of Denmark. 2009.
- M. F. Hansen, R. Larsen, Validation of Virtual Cuts. DTU Informatics, Technical University of Denmark. 2009.

Abstracts:

- M. F. Hansen. Designing and analyzing virtual cuts in 3D models of pig bodies by mapping cuts from a statistical atlas. *European Congress of Chemical Engineering - ECCE6 - Special Symposium - Innovations in Food Technology*

Acknowledgement

This thesis is *not* by any means the sole product of the author, and it would never have been finished without the help, inspiration and support from a number of people. First of all I would like to thank my supervisor Rasmus Larsen for his guidance and supervision throughout the project – especially for pushing me through the final stretches of the project.

Friends, current and former colleagues at the imaging group at DTU Informatics I thank for providing an inspiring and relaxed working environment. Søren G. H. Erbou, Martin Vester-Christensen, Michael S. Hansen and Thomas H. Mosbech I foremost thank you for not complaining about my dirty mountain bike being parked in our office but also for your friendship, collaboration, help and for our discussions on numerous topics as well as off-topics. Furthermore, I owe Michael and Thomas my gratitude for proof-reading and commenting my thesis. I apologize to Jacob A. Bærentzen for my constant interruptions and questions about mesh generation and geometry in general, and I ensure you that your answers have been most helpful. Eina Boeck, whose unofficial title must be back bone of the imaging group, I give an extraordinary thank for constantly reminding me of the things I constantly forget, and for making practical problem go away.

The project would never have seen the light of the day without the help from the kind people at the Danish Meat Research Institute. The unconditional help and guidance from Lars B. Christensen have been a supporting foundation throughout the project. Eli V. Olsen, whom I'm sure never receive the credit she deserves, for making things happen and for taking a welcoming interest in the project. In addition, I would like to thank Claus Borggaard, Jesper Blom-

Hansen, Niels-Christian Kjærsgaard, Claus Søndergaard and Marchen Hviid and many others for their collaboration and help.

A special thanks to Colin Studholme for accepting my request for collaboration and for sharing his vast knowledge on the topic of image registration during my research stay at Department of Radiology, University of California, San Francisco. To my office mates at UCSF Kio Kim and Piotr Habas, who I shared a small mice infected office with in the basement of a building at the Parnassus campus, I would like to offer my gratitude for allowing me to take up valuable space, their help and many interesting discussions.

Heartfelt thanks to my family and friends for their understanding and support through the entire thesis period. It is my hope that the completion of my doctoral dissertation marks the beginning of a time, where I can worry about those things which are truly important in life, and where I can spend more time with the people whom I love and care for.

Finally, I would like to thank my Ph.D. committee, consisting of Ruzena Bajcsy, Jan Modersitzki and Allan Aasbjerg Nielsen, for taking the time to read, comment, assess my thesis as well as providing many interesting questions at my thesis defence.

I dedicate this thesis to my beloved grandmother and uncle who were taken away during the period of the study.

Contents

Part I

Introduction

Chapter 1

Introduction

With the first recorded shipment of Danish bacon arriving in England in 1847 [4] Denmark embarked on the journey of becoming the world largest exporter of pork. At the time of the establishment of the Federation of Danish Cooperative Bacon Factories[1] (1890s) 90% of the export of Danish Bacon was bound for the UK. Since post World War II the production of pork has grown steadily to an astonishing 26 million pigs/year, and the export markets have been expanded to include more that 130 countries world-wide. In 2007, the export of pork accounted for 5% of the total Danish export or 27 billion DKK [5], which makes the pig producing industry a significant part of the Danish economy.

By maintaining a focus on food safety, quality and efficiency through research the Danish Pig Producing Industry (DPPI) has managed to protect its position as market and export leader for decades despite difficult challenges such a high salary pressure and stringent safety restriction. To quantify these challenges it can be mentioned, that the cost of producing meat is twice as high in Denmark compared to international competitors U.S. and Brazil [6], and the hourly salary of a Danish butcher was 210DKK in 2005 which contrasts the mere 90DKK salary of a butcher in the neighboring country of Germany. The increase in oil and fodder prices through 2007 and 2008 has put additional pressure on the DPPI to the extend that the Danish pig producers have lost 352DKK per produced pig in the first quarter of 2008[9]. Forecasts estimate

[1] Known today as the Danish Meat Association

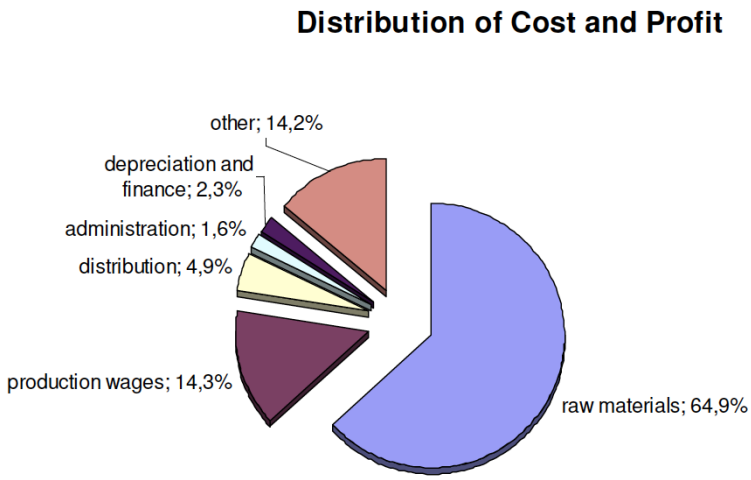

Figure 1.1: Distribution of cost and profit of the Danish production of pigs (Courtesy of Kjærsgaard[87]).

that the population of pigs in Denmark will have dropped with 5-10% at end of 2008 [8, 9].

To avoid further recession in the pig production DPPI need to continue or rather intensify the process of improving the efficiency in the abattoirs. As the companies behind the abattoirs are completely owned by the Danish pig producers, their main goal is to maximize the price, which they can pay for the raw material (pigs). To increase the pay to the Danish pig producers the abattoirs need to cut production wages by reducing the use of manual labor and to improve the utilization of the raw material. The graph in Figure 1.1 visualizes the distribution of cost and profit in the modern abattoirs. As the production wages in the modern abattoirs are relative small compared to the price of the raw material the hypothesis is, that there is more money to be made in a better utilization of the raw materials than in a further reduction in the use of manual labor.

As pigs are a biological material they exhibit a natural dispersion in weight and in the local and global distribution of meat and fat. In the modern abattoirs pig carcasses are sorted after their weight and a global estimate of the lean meat content obtained using an ultrasonic measuring device known as AutoFom [160]. The lack of local information and a considerable uncertainty in a global estimate of the lean meat content imply that the sorting of pig carcasses and the resulting utilization of the pig carcasses are far from optimal. The work by Kjærsgaard

et al. [87] confirmed that an improvement of the carcass measurement will result in a substantial improvement in profit due to a better utilization of the carcasses. Better measurements will also result in more uniform and higher quality products which may have a considerable strategic value in the future.

Before a better raw material utilization can be achieved the DPPI is faced with a number of challenges:

1. **Improvement of the online measuring in the abattoirs.**
   The online measuring devices in the abattoirs have to be improved to provide more local information with less uncertaincy. The industry is currently in the process of investigating the possibility of constructing an industrial CT scanner which can be used for online measuring in the abattoirs.
2. **Better understanding of the biological variation in pigs.**
   A crucial step on the road for better raw material utilization is the construction of a model of the biological variation in pigs. Today, the biological variation of pigs is mostly described in terms of the variation in weight and lean meat content.
3. **Development of methods for relating the biological variation with the optimal use.**
   Given an improved model of the biological variation of pigs the subsequent step is to relate the model to the possible product ranges, which then can be linked to the order books and the potential yield.

To develop better methods for determining the lean meat content and for modeling the biological variation in pigs the Danish Meat Research Institute (DMRI)[2] turned their attention to the non-invasive imaging technique X-ray Computed Tomography and initiated the Virtual Slaughterhouse (VSH) project in collaboration with DTU Informatics in 2006. The primary reason for using CT as the imaging modality in the VSH project is that the tissue types of interest (meat, fat and bone) are clearly distinguishable on a CT scan. This Ph.D. project is partially sponsored the VSH.

1.1 Objective

The primary objectives of this thesis are to study the morphology of pigs and to construct tools which can aid to bridge the gap between the *virtual abattoirs*

[2]DMRI is owned by the Danish pig producers through DMA.

and the *actual* abattoirs. More formally the aims of thesis are:

- To construct a deformable pig atlas from CT scans of pigs carcasses which can be used to analyze the biological variation of pigs.
- To build a prototype for a virtual cutting tool upon the deformable pig atlas which can imitate the real cuttings from abattoirs.
- To construct a methodology for validating the virtual cuts against the real cuts from abattoirs.

1.2 Thesis outline

This thesis consists of an introductory part (chapter 1-5), a contribution part of papers (chapter 6-12) and a discussion part (chapter 13).

Chapter 2 gives the unacquainted reader an introduction to the Danish meat industry. This chapter provides additional motivation for this thesis and the VSH project in general.

Chapter 3 introduces the concept of morphology and gives a brief overview of image based morphology. The chapter can be skipped by the familiar reader as it primarily is a small literature study.

Chapter 4 describes the fundamental building blocks of image registration. The chapter focuses on elastic deformation modeling which has been used extensively in this thesis.

Chapter 5 takes image registration to the practical level of discretization and optimization. The emphasis of the chapter is placed on the discretize-optimize approach which is the applied method for solving the image registration problem. In addition, it offers a small comparison of non-parametric and parametric image registration.

Chapter 6 gives a quick summery of the contributions of this thesis and an overview of the functionality of the RegLab registration framework.

Chapter 7 introduces the concept of a cutting atlas and its applicability. It further describes the construction of the *Horsens cutting atlas* and presents concrete examples of virtual cuts.

Chapter 8 visualizes the gap between virtual cutting and real cutting. 37 virtual *back 2* products are geometrically compared to the corresponding real back 2 products after spatial normalization. The validation of the virtual cuts is vital for the success of the VSH.

Chapter 9 presents an approach for aligning a set of 3D surfaces without correspondences using signed distance maps for shape representation. The alignment approach is compared with the well-known *iterative closest point* algorithm on a set of pelvic bones from pigs.

Chapter 10 deals with the construction of diffeomorphic deformation models. The chapter provides a theoretical discussion and solution to the problem of constructing deformation models which are guaranteed to be diffeomorphic. The solution is tested by registration of a set of 2D Magnetic Resonance Images (MRIs) of the Corpus Callosum.

Chapter 11 presents an approach for constructing conditional statistical priors on compositional parameterized deformation models. The ability to capture biological variation is tested on a set of 2D MRIs of the Corpus Callosum.

Chapter 12 presents an approach for tessellating binary shapes with Tetrahedra. The tetrahedral mesh is the basis for the finite element based discretization applied in this thesis.

Chapter 13 discusses the contribution of the thesis and finishes the thesis with a conclusion.

1.3 Nomenclature

1.3.1 Basic Linear algebra

Vectors are represented in columns and typeset in italic, lower-case, boldface using spaces to separate elements: $\boldsymbol{v} = [v_1\ v_2\ v_3]^T$.

Matrices are represented row wise and typeset in italic, upper-case, boldface: $\boldsymbol{M} = \begin{bmatrix} m_{11} & m_{12} \\ m_{21} & m_{22} \end{bmatrix}$.

Vector functions are typeset in italic boldface: $\boldsymbol{f}(\boldsymbol{v}) = \boldsymbol{v}+\boldsymbol{v}$ and $\boldsymbol{F}(\boldsymbol{v}) = \boldsymbol{v}\boldsymbol{v}^T$.

1.3.2 Norms, function and operators

Inner product is typeset using angle parentheses or central dot $< \boldsymbol{a}, \boldsymbol{b} >= \boldsymbol{a} \cdot \boldsymbol{b} = \sum_{i=1}^{n} a_i b_i$.

Tensor product is denoted by $\otimes$. For matrices (Kronecker product) we have

$$\boldsymbol{A} \otimes \boldsymbol{B} = \begin{bmatrix} A_{11}\boldsymbol{B} & \cdots & A_{1n}\boldsymbol{B} \\ \vdots & \ddots & \vdots \\ A_{m1}\boldsymbol{B} & \cdots & A_{mn}\boldsymbol{B} \end{bmatrix}.$$

The outer product (tensor product of vectors) $\boldsymbol{a} \otimes \boldsymbol{b}$ will be treated as the Kronecker product and therefore not produce the usual $m \times n$ matrix $\boldsymbol{a}\boldsymbol{b}^T$ but a vector with length mn.

The trace operator is denoted $\mathrm{tr}(\boldsymbol{M}) = \sum_{i=1}^{n} m_{ii} = \sum_{i=1}^{n} \lambda_i$.

***p*-norm** is a sequence of norms of the form $\|\boldsymbol{x}\|_p = (\sum_{i=1}^{n} |x_i|^p)^{\frac{1}{p}}$.

Weighted 2-norm is denoted by $\|\boldsymbol{x}\|_{\boldsymbol{M}} = \|\boldsymbol{M}^{\frac{1}{2}}\boldsymbol{x}\|_2$.

Frobenius norm is denoted by $\|\boldsymbol{M}\| = \mathrm{tr}(\boldsymbol{M}^2)^{\frac{1}{2}}$.

The Vectorization operator is denoted with vect. In general, $\mathrm{vect}(\boldsymbol{M})$ produces a lexicographically ordered vector with the elements of $\boldsymbol{M}$. If $\boldsymbol{M}$ is a $n \times n$ symmetric matrix $\mathrm{vect}(\boldsymbol{M})$ produces an vector of length $n!$ of the upper diagonal elements, where the first n elements are the diagonal elements, and the remaining elements are lexicographically ordered.

The determinant is denoted $\det(\boldsymbol{M}) = \prod_{i=1}^{n} \lambda_i$.

The element quotient is denoted $\boldsymbol{a}./\boldsymbol{b} = \begin{bmatrix} a_1/b_1 & a_2/b_2 & \cdots & a_n/b_n \end{bmatrix}$.

The floor operator floors the elements of a vector and is denoted $\lfloor \boldsymbol{x} \rfloor$.

The remainder operator returns the remainder after a floor operation and is denoted $\rfloor \boldsymbol{x} \lfloor = \boldsymbol{x} - \lfloor \boldsymbol{x} \rfloor$.

Floor lattice operator upon the lattice $\mho$ is denoted $\lfloor \boldsymbol{x} \rfloor_{\mho} = \lfloor (\boldsymbol{x} - \boldsymbol{x}_0)./\boldsymbol{\Delta} \rfloor$.

Remainder lattice operator upon the lattice $\mho$ is denoted $\rfloor \boldsymbol{x} \lfloor_{\mho} = (\boldsymbol{x} - \boldsymbol{x}_0)./\boldsymbol{\Delta} - \lfloor (\boldsymbol{x} - \boldsymbol{x}_0)./\boldsymbol{\Delta} \rfloor$.

The convolution operator of the function f and g is denoted $(f * g)(t) = \int_{-\infty}^{\infty} f(\tau) g(t - \tau) d\tau$.

1.3.3 Symbols and constants

Symbol	Explanation
Ω	Domain of an image.
$\mathcal{C}^n$	The space of functions where the nth derivative is continuous.
$\mho$	A rectangular lattice (a.k.a. regular grid) is represented by the tuple $(\boldsymbol{x0}, \boldsymbol{\Delta}, \boldsymbol{S})$, where $\boldsymbol{x_0}$ is the first point in the lattice, $\boldsymbol{\Delta}$ is the spacing between the points, and $\boldsymbol{S}$ is the size of the lattice.
$I(\boldsymbol{x})$	An image function.
$R(\boldsymbol{x})$	A reference image function.
$T(\boldsymbol{x})$	A template image function.
$\mathcal{I}$	A discrete image.
$\boldsymbol{\phi}(\boldsymbol{x})$	Warp function or geometrical transformation.
$\boldsymbol{u}(\boldsymbol{x})$	Displacement function.
$\boldsymbol{R}$	Orthonormal or rotation matrix.
$\boldsymbol{E}$ or $\boldsymbol{E}(\boldsymbol{x})$	Strain tensor.
$\boldsymbol{F}$ or $\boldsymbol{F}(\boldsymbol{x})$	Deformation gradient tensor.
$\boldsymbol{U}$ or $\boldsymbol{U}(\boldsymbol{x})$	The right stress tensor.
$\boldsymbol{C}$ or $\boldsymbol{C}(\boldsymbol{x})$	The right Cauchy-Green deformation tensor.
$\mathcal{D}$	Dissimilarity measure.
$\mathcal{S}$	Regularizer.
$\mathbb{R}^n$	n dimensional space of real numbers.
$\boldsymbol{I}$	The identity matrix.

1.3.4 Acronyms and abbreviations

CT	X-ray Computed Tomography
DMA	Danish Meat Association
DMRI	Danish Meat Research Institute
DPPI	Danish Pig Producing Indutry
HU	Hounsfield Units
IRP	Image Registration Problem
MRI	Magnetic Resonance Imaging
US	Ultrasound
VSH	Virtual Slaughterhouse

Chapter 2

Background

This chapter gives the unacquainted reader an introduction to DDPI, the modern abattoirs, pig carcass classification and CT. The acquainted reader can jump directly to the last section of this chapter which provides a small description of the data sets used in this thesis

2.1 The Danish meat industry

The Danish meat industry is essentially a large cooperative society of meat producers who have chosen to unite on a number of areas such as research and development, food safety, veterinary alert systems, marketing, communication, administration and financial management. These responsibilities are handled by the branch organization Danish Meat Association (DMA) which is owned by the cooperative companies running the abattoirs. All research and development within DMA is carried out by DMRI which was founded back in 1956. DMRI is responsible for handling all research branches of the pig production process from the time the pigs are picked up at the farmers to consumption.

The core research areas of DMRI are:

- Product quality.
- Food safety.
- Automatization and product efficiency.

The topic of this thesis lies within the last of these research areas.

2.2 The modern abattoirs

Figure 2.1 gives a schematic overview of the modern abattoirs. In a modern abattoir the pigs enter the *black slaughter-line* (marked by A in Figure 2.1), where they are sedated using carbon dioxide, bled-to- death and finally cleaned with a number of contraptions. At the black slaughter-line the carcasses are graded/-classified with the AutoFom measuring device. From the black slaughter-line the pigs enter the *white slaughter-line* (marked by B in Figure 2.1), where intestines are removed and the carcasses are split through the middle of the spine. From the white slaughter-line the carcasses are moved into a cooling facility where they are chilled and sorted into batches. The day after slaughtering the chilled carcasses enter the cutting line (marked by C in Figure 2.1), where they are trisected into the fore-end, the pork middle and the ham part. The fore-end, the pork middle and the ham part are subsequently cut into a number of products depending on the grading.

2.3 Classification

To optimize the use of the pig carcasses the pigs have been graded with an objective measure since the 1930s. The *lean meat percentage* (LMP) is the standard measure today and is defined as the ratio between the weight of the meat and the total weight of the carcass without organs. As the pig carcasses enter the cooling facility they are sorted into batches using the LMP and the weight of the carcasses. Today, all carcasses in a batch are cut into the same range of products. In modern abattoirs, the AutoFom system estimates the LMP from an ultrasonic measure of the fat thickness at a number of anatomical positions along the back of the pig. Approximately every decade the measures of the fat thicknesses are calibrated against the LMP by having specially trained butchers

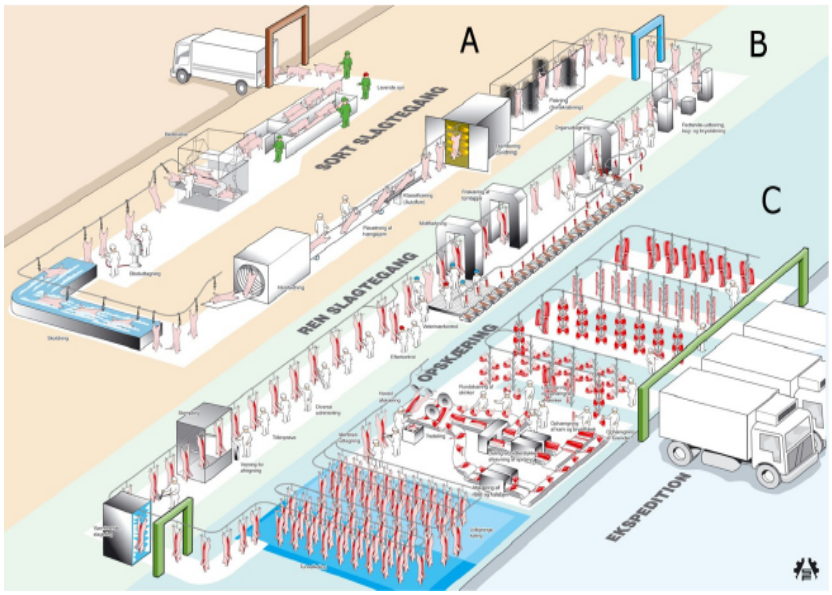

Figure 2.1: The slaughter-line. Part A: Sedation, killing and cleaning. Part B: Removal of organs, inspection and grading. Part C: Chilling and major cut. Courtesy of DMA.

dissect a representative set of pigs. A relatively high uncertainty in both the dissected LMP and the fat thickness measures (due to inter-butcher variation and to ultrasonic measuring problems with distinguishing between different tissue transitions) questions the reliability of the estimates of the LMP. A newly development algorithm for virtual dissection using CT by Vester-Christensen et. al. [167] has however lowered the uncertainty of the dissected LMP to a negligible level.

Even though future estimates of the LMP may be more precise, the global nature of the LMP implies, that it does not provide enough information to guarantee an optimal sorting and raw material utilization. Therefore, one of the main challenges is to identity new local predictors of quality which will lead to an improvement of the utilization of raw material.

2.3.1 The virtual slaughterhouse

The search for new predictors was one of the primary reasons that DMRI in 2004 invested in their first medical CT-scanner. Simultaneously with acquisition of the scanner DMRI initiated a new research collaboration with the DTU Informatics which resulted in establishment of the Virtual Slaughterhouse (VSH) project in 2006. The VSH project focuses on the development of morphological tools for investigating and analyzing 3D models of pig carcasses. It is the belief that these tools can aid the identification of the new quality predictors, the optimization of raw material use, the development of new cutting robots and the development of new products.

2.4 Computed tomography

CT was the first non-invasive imaging technique to construct a 3D image of the internals of an object. The word tomography arises from the greek words tomos (slice) and graphy (describing) and refers to the fact a 3D CT image is often represented as a series of 2D slices. The theoretical foundation of the CT system was publicized by Allan McLeod Cormack in 1963 and in 1964 . However, little attention was given to the technique until Godfrey Newbold Hounsfield build the first CT scanner in 1972. Both scientist received the nobel prize in 1979 for their contribution to medical imaging.

In X-ray computed tomography an X-ray tube (source / photon emitter) is rotated around a given object while detectors on the opposite side of the source

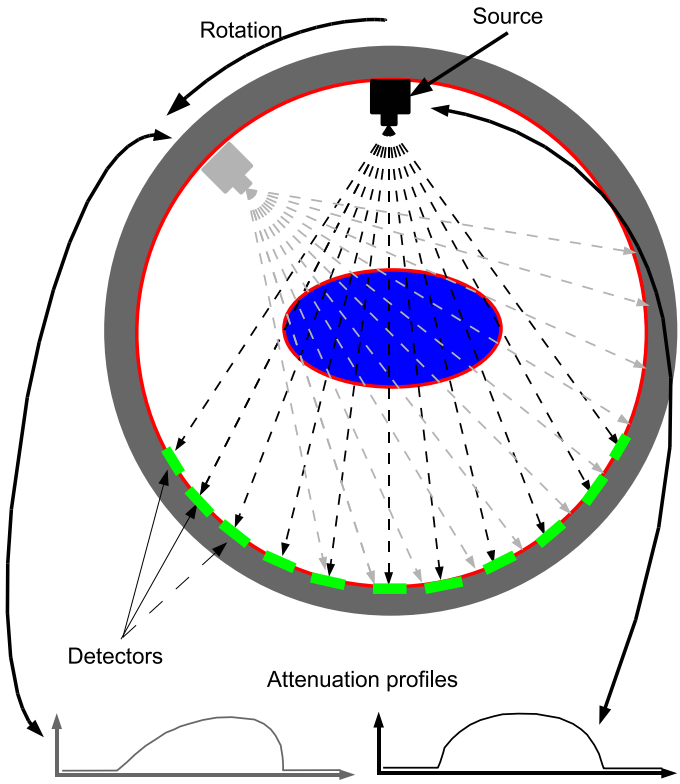

Figure 2.2: The principle of CT.

measure the attenuations of the rays. Figure 2.2 illustrates the principle. As different tissues have different densities and attenuations, an image of the interior of an object can be constructed by estimating the spatial distribution of the linear attenuation coefficient. In practice, this means to recover the linear attenuation coefficients at a finite number of spatial positions (regular grid). The mean number of recorded photons from a ray traveling along a line L is in theory given by

$$b \exp^{-\int_L \mu_0(\boldsymbol{x}) dl}, \tag{2.1}$$

where $\mu_0(\boldsymbol{x})$ is the linear attenuation coefficient and b is a constant. The field or image of linear attenuation coefficients is traditionally reconstructed from the recorded attenuation profiles by applying filtered backprojection (cf. [30] and [147]) which reduces to an inverse Radon transform of the line integrals (Eq. 2.1) and the application of high-pass filters to eliminate blurring.

The reconstructed attenuation coefficient image is scaled or calibrated against

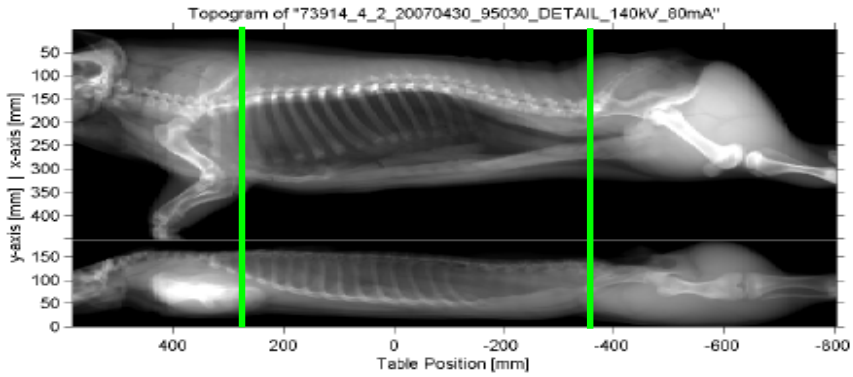

Figure 2.3: Topogram of full body scan of half pig carcasses . The two green lines approximately mark the beginning and the end of the part of the pig known as pork middle.

the Hounsfield scale such that the attenuation of air receives HU -1000, and the attenuation of distilled water receives HU 0.

2.5 Data sets

The section gives a brief description of the data sets which have been used in this thesis. Two of three data sets consist of CT scans of the pork middle which is the area of the half pig carcass marked by the green lines in Figure 2.3.

2.5.1 Thisted

The Thisted data set consists of 37 paired CT scans of the pork middle and the resulting products (back bacon, streaky, ribs and spine) from the pork middle cutting robot[7]. Voxel dimensions are $[0.87 \times 0.87 \times 10]\text{mm}^3$ with a 10mm spacing between consecutive slices. The data set was created with a reconstruction algorithm which emphasizes bone. As a consequence of this choice the meat and fat tissue areas are noisy and affected by shade artifacts from the bone areas. This data set was acquired in early 2006 at the Danish Crown abattoir in Thisted.

2.5.2 Horsens

The Horsens pork middle data set consists of 300 CT scans of the pork middle of carcasses of mixed breeds and representative of the Danish pig population w.r.t. weight and LMP. Voxel dimensions are $[0.87 \times 0.87 \times 10]\text{mm}^3$ with a 10mm spacing between consecutive slices. This data set was acquired in early 2007 at the Danish Crown abattoir in Horsens.

2.5.3 Duroc

The Duroc data set consists of 40 full body CT scans of 40 half pig carcasses of the breed Duroc, both gender. Voxel dimensions are $[0.87 \times 0.87 \times 10]\text{mm}^3$ with a 10mm spacing between consecutive slices. 7 of the 40 observations were discarded due to missing structures.

Chapter 3

A short introduction to morphology

Morphology is the study of *form*, *shape* and *structure* of objects. The history of morphology dates back to ancient Greece, where *Aristotle* in his work *Historia animalium*[2] offered numerous descriptions of species and their anatomy. The dissections and the concurrent illustrations of human bodies by Andreas Vesalius (*De humani corporis fabrica*, 1543) are one of the earliest signs of scientific morphology, as we know it today. In the 1970s the world of morphology was revolutionized by the introduction of 3D non-invasive imaging techniques such as CT and MRI. Since the pioneering work on elastic matching of images by Broit [24] and Bajcsy et. al. [13–15, 141] the descriptive power of morphology has grown almost exponentially with continuing development of models for shape and deformation representation, and statistical methods for relating the morphological information to biological functioning (*physiology*). Today, morphometry is one of the most valuable and applicable tool in medical and biological science.

Shape is an abstract idea or concept which makes the task of describing the shape of an object complicated. The shape or structure of an object is to some extent related to the configuration of the surface of the object. If you ask a person to describe the shape of an apple you will probably get the answer "it is kind of round" or the answer "it is almost shaped like a ball". In almost every

case people will describe the shape of an object in terms of its deviation from some simple but similar geometric entity (circle, triangle etc.). Interestingly, it is probably easier to explain the difference in shape between two apples than to describe the shape of one of them. The point to be made is that shape is a relative quantity, or rather it is measured relatively to some known reference. This is also reflected in the definition of shape proposed by Kendall [84] which will be used throughout this thesis.

Definition 3.1 Shape is all the geometrical information that remains when location, scale and rotational effects are filtered out from an object.

Thus, a reference shape is needed in order to fix a reference coordinate frame, to filter out location, scale and rotational effects and to measure the remaining geometrical information. The process of transforming two or more shapes to the same coordinate system is called *alignment*. To quantify the remaining geometrical information in term of deviation or distance between shapes it is necessary to have the correspondence between the shapes. We call the process of establishing this correspondence for *registration*.

In the early years of image based morphology, registration was done manually by landmarking – placing points of correspondence along the boundaries or surfaces of the objects. Shape alignment using e.g. generalized Procrustes analysis [67] followed the landmarking procedure, leading the way for a subsequent covariance-based analysis of shape. Landmark based representation of shape is still today one of the most applied forms of shape representation but the use is often hindered (especially in 3D) by the reliance on manual landmarking. Methods such as the Iterative Closest Point (ICP) [27] and the Minimum Description Length method for correspondence optimization (MDL) [46] have partially eliminated the need for manual landmarking. The applicability of the MDL method is limited to surfaces of the objects which are topologically equivalent to a sphere. The standard ICP algorithm applies the Euclidean distance to measure the distance between corresponding points and hereby assumes, that all point classes are normally distributed with the same standard deviation. Hansen et. al. [75] proposed an extension to the usual ICP algorithm which uses the Mahalanobis distance with a spatially dependent covariance matrix instead of the Euclidean distance. The spatially dependent covariance matrix is updated iteratively during the alignment.

Image registration or spatial normalization as coined by the neuroimaging community establishes correspondences between two images by maximizing the similarity w.r.t. a spatial deformation of one of the images. The underlying assump-

tion being that the present anatomical structures begin to match spatially as the images becomes more similar.

In most registration schemes, a regularizer is applied to ensure a *valid* spatial deformation which is *smooth* and *topology preserving*. The majority of regularization approaches find their motivation in continuum mechanics. Broit [24] initially proposed the idea of using linear elastic body forces to regularize the deformation which was later adapted into a registration algorithm by Bajcsy et. al. [15]. Pennec et. al. [122] introduced Riemannian elasticity which in contrast to linear elasticity is rotation invariant and therefore capable of capturing much larger deformations. Rohlfing et. al. [128] and Tanner et. al. [159] essentially performed elastic image registration by incorporating volume-preserving soft constraints in registration of pre- and post-contrast MRIs of female breasts. Almost similarly, Haber and Modersitzki [71] used volume-preserving hard constraints together with linear elasticity for the registration of pre- and post-contrast MRIs. Fisher and Modersitzki [56] proposed diffusive regularization which is the squared Fröbenius norm of the displacement gradient.

Christensen [31] introduced the use of viscous-fluid priors which regularize the flow of the deformation rather than the relative spatial displacements. Fluid registration has become widely popular in the neuroimaging community [25, 26, 40, 43, 62, 63, 152, 168] because of its ability to model large deformations.

Rueckert et. al. [135] reduced the dimensionality of the image registration problem and ensured a smooth deformation field by using B-splines to describe the deformations between images. Many research groups have since adapted this approach – among those Studholme et. al. [26, 151, 155] , Thevenaz et. al. [148, 162], Kybic et. al. [91, 92], Rohlfing et. al. [127–129] and Hansen et. al. [77]. Other typical parameterizations of the deformation field are the cosine kernel proposed by Cootes et. al. [37] and different kinds of radial basis functions [60, 61, 65, 102, 126, 146].

In morphometry studies, image registration can in be divided into two groups:

Intra-subject, which refers to the case where two images of the *same* subject are registered to each other.

Inter-subject, which refers to the case where two images of *different* subjects are registered to each other.

Intra-subject registration is typically used in surgical planning applications [66, 80, 100, 153, 174], in comparisons of pre- and post-operative images [132, 140], in clinical diagnostics, e.g. registration of pre- and post-contrast images [71,

129, 134, 159], and in neurodegenerative studies [40, 62, 63, 138, 152].

Inter-subject registration is in most cases interchangeable with atlas registration, where a set of target images is registered to a reference image. The simplest way of constructing a model or atlas image is simply to choose an image of a *normal* subject among the targets. An unbiased atlas can be constructed by selecting an initial reference image which is registered to the remaining images and subsequently updated with the mean deformation of the registrations [82]. Spatial normalization against an atlas is an essential part of population based morphometry studies, as it allows for an morphological comparison between a set of *abnormal* subjects and a control group of *normal* subjects [3, 25, 112, 116, 130, 150]. Also, atlases are commonly used for automated segmentation by mapping labels from the atlas image to spatially normalized targets [19, 49, 53, 98, 101]. The construction of statistical atlases by incorporating statistical deformation priors from a set of previously registered images has been proposed by Rueckert et. al. [133] and Cootes et. at. [37]. The constructed statistical deformation models were however unable to capture the statistics of the deformations with a sufficient accuracy which perhaps can be contributed to a relative small set of training samples. Closely related to the notion of a statistical atlas is the active appearance model (AAM) proposed by Cootes [35], which combines statistical spatial deformation modes with statistical synthesis of texture from a training set of annotated images.

Chapter 4

Image registration

The *image* registration problem (IRP) is the task of uncovering a *suitable geometrical transformation*, which transforms a template image such that it becomes *similar* to a reference image. More formally, it can be formulated as the minimization of the objective function

$$C[R, T; \phi] = \mathcal{D}[R, T \circ \phi] + \alpha \mathcal{S}[\phi], \tag{4.1}$$

where R and T are the reference and the template images, ϕ is the transformation, $\mathcal{D}$ is the (dis)similarity measure, $\mathcal{S}$ is a regularizer and finally α is trade-off constant. This chapter contains a comprehensive but not exhaustive description of the four fundamental building blocks of image registration

Image representation: Of the four building blocks the representation of an image is probably the most neglected as it on a first hand basis may seem trivial. A correct and suitable representation may have a dramatic influence on the convergence of the optimization and have a significant impact on the final accuracy of the registration. The most widely spread misconception is the computation of the image derivatives. Many people choose to compute the image derivatives by approximating the derivatives on the data lattice using e.g. a finite difference scheme and then interpolate the finite difference derivatives. The correct approach is to compute the derivatives directly from the chosen interpolation scheme. Not doing

so leads to a mismatch between the image values and image derivatives, which at best leads to a slower convergence and in some cases makes the optimization fail to produce the correct optimum. The theory of scale-space is another important aspect of image representation which reduces the chance of falling into a local minimum. Image interpolation, image derivatives and scale-space theory will be discussed in this chapter.

Similarity measure: The ability to measure the degree of similarity or rather the dissimilarity between two images is the basis of image registration. The (dis)similarity measure provides the forces which drive the registration between two images. The measures presented in this thesis are all dissimilarity measures, and thus return a non-negative score, which quantifies the degree of dissimilarity between the reference and template images. Zero implies that the two images are *identical* or *completely similar*. Therefore, dissimilarity measures are often conceived as being distance functions, which is unfortunate as most dissimilarity measures are not distance functions or metrics in a strict mathematical sense. This chapter will provide an overview of the most widely used measures and discuss their applicability.

Geometrical Transformation: In the literature, it is customary to differentiate between two types of transform representations; parametric and non-parametric. While this distinction exists in theory it becomes somewhat blurry in practice, as the discretized transformation in either case is in the linear form $\boldsymbol{x} + \boldsymbol{w}^T\boldsymbol{q}$. This statement will be discussed further in the next chapter 5 *Discretization and optimization*. The representation $\boldsymbol{\phi}(\boldsymbol{x}) = \boldsymbol{x}+\boldsymbol{u}(\boldsymbol{x})$ will be used throughout this thesis, where $\boldsymbol{x}$ is the spatial position to be displaced and $\boldsymbol{u}(\boldsymbol{x})$ is the *displacement*. In the parametric case, the representation will be extended to $\boldsymbol{\phi}(\boldsymbol{x};\boldsymbol{w}) = \boldsymbol{x}+\boldsymbol{u}(\boldsymbol{x};\boldsymbol{w})$ where $\boldsymbol{w}$ is some displacement parameter. Parameterization can be interpreted as a restriction of the space of possible transformations from the space of all transformation to a subset, which is homeomorphic to some parameter space[1]. In many cases there are large advantages in using a parametric representation to model the transformation in terms of fast optimization, dimensionality reduction and stability. On the other hand, it may not always be feasible to model the set of possible deformations using a parametric representation, and doing so may lead to sub-quality registrations. An overview of parameterization types will be given and discussed.

Regularization: The IRP is in almost every circumstance an *ill-posed* problem and thus requires additional information to be solved. Regularization e.g. by imposing smoothness restrictions is probably the best method to add the information which is needed to make the problem *well-posed*. A good

[1]Normally $\mathbb{R}^M$ where M is the number of parameters.

parametric model is sometimes enough to guarantee that all transformations are *suitable*. For this reason some researchers consider parameterization to be a form of *implicit regularization*. Indisputably, a parameterization restricts the space of possible transformations, but it can only be considered to be a very crude form for regularization as it assumes a uniform distribution on the space of possible transformations. It is the view of the author that the label *implicit constraint* gives a much better understanding of parameterization than *implicit regularization*. Most regularizers belong to one of two categories of regularizers or perhaps even both; Bayesian motivated regularizers where the interpretation of regularization is a matter of imposing a prior on the parameters, or physically motivated regularizers where neighboring particles interact with each other and thus exert force upon each other under deformation caused by external forces. In image registration, we are mostly interested in regularizers which are rotation and scale invariant. This chapter focuses on elastic regularization as the majority of these regularizers fall into the category of *elastic regularization*. Basic *elasticity theory* will be covered in this chapter and examples of *elasticity energies* will be given and compared.

4.1 The notion of an image

If you decide to look up the word *image* in the Merriam-Webster dictionary [107] you will find the following definition

> A reproduction or imitation of the form of a person or thing...

In most ways this definition fully captures our understanding of an image but it gives no information on the representation of an image. For a more formal definition we turn our attention to the world of mathematics where image is a synonym for *range*.

Definition 4.1 (Range) Let $f : \Omega \to \boldsymbol{Y}$ be a function over the domain Ω, then the *range* of f is defined as the set of all values that f can take as its argument varies over Ω, i.e.,

$$\text{Range}(f) = f(\Omega) = \{f(\boldsymbol{X}) : \boldsymbol{X} \in \Omega\}$$

While the definition of range is precise it does not harmonize with our understanding of an image. Range provides the tools for describing the colors of an object but not shape and placement of the object. In order for us to reproduce or describe an object we need to combine spatial information with spectral information. E.g. if we wanted to describe the famous Venus de Milo Statue we could make a map which relates all psychical positions in Louvre (domain) with a value telling whether a given position is inside or outside the statue. As such an image is just a function which relates some type of information to physical positions. In this thesis the notion of an image will be restricted to the set of functions which have a smooth mapping from a subset of the Cartesian space to the space of real numbers.

Definition 4.2 (Image) An image is a $\mathcal{C}^1$ function $I : \Omega \to \mathbb{R}$ where $\Omega \subseteq \mathbb{R}^N$.

In practice, image acquisition devices return image data uniformly sampled and not a smooth function. In this thesis, a rectangular lattice is represented by the tuple $\mho = (\boldsymbol{x}_0, \boldsymbol{\Delta}, \boldsymbol{S})$, where $\boldsymbol{x}_0$ is the physical position of the first point in the lattice, $\boldsymbol{\Delta}$ is the spacing between the points and finally $\boldsymbol{S}$ is the size of the lattice. This leads to the definition of a discrete image

Definition 4.3 (Discrete image) A discrete image $\mathcal{I}$ of an image I is the set of samples

$$\mathcal{I} = (I(\boldsymbol{x}), \mho) = \{(\boldsymbol{x}_0, I(\boldsymbol{x}_0)), (\boldsymbol{x}_1, I(\boldsymbol{x}_1)), \dots (\boldsymbol{x}_{n-1}, I(\boldsymbol{x}_{n-1}))\}, n = \prod_i^N S_i,$$

where $\mathcal{I}_i = I(\boldsymbol{x}_i)$ is the sampled intensity at the sample point $\boldsymbol{x}_i$. The samples are lexicographically ordered such that first dimension has the most frequent oscillations.

To bridge the gap between the discrete image and image function we introduce the concept of an interpolator.

Definition 4.4 (Interpolator) A function $I_{\mathcal{I}} : \Omega \to \mathbb{R}^N$ is an interpolator of $\mathcal{I}$ if $\forall_i I_{\mathcal{I}}(\boldsymbol{x}_i) = \mathcal{I}_i$.

Interpolation is the special case of regression where the error/noise term is assumed to be zero. As such it relies on the assumption that the two samples $\mathcal{I}_0 = I(\boldsymbol{x}_0)$ and $\mathcal{I}_{\boldsymbol{h}} = I(\boldsymbol{x}_0 + \boldsymbol{h})$ are correlated. It is customary to model this correlation by representing $I_{\mathcal{I}}$ as a weighted sum of basis functions, i.e.

$$I_{\mathcal{I}}(\boldsymbol{x}; \boldsymbol{w}) = \sum_{i=1}^{n} w_i k_i(\boldsymbol{x}) = \langle \boldsymbol{k}(\boldsymbol{x}), \boldsymbol{w} \rangle \,. \tag{4.2}$$

4.1.1 Interpolation of regularly sampled data

This thesis will restrict the field of interpolation to the case, where data are sampled on a rectangular lattice. Techniques such as kriging [103] can be applied in the case of irregularly sampled data as well as regular.

Since image interpolation is frequently used in image registration we require an interpolator which can be evaluated quickly. For this reason, the scope of considered basis functions is further limited the to subset which fulfill the constraints:

- The basis functions can be represented as the tensor product of a set of 1D uniform basis functions.
- The basis functions are compactly supported.
- The knots of the basis functions coincide with the sample points of the discrete image, and thus it is possible to represent the weight coefficients $\boldsymbol{w}$ of the basis functions as a discrete image $\mathcal{W}$ with same dimensionality as $\mathcal{I}$.

The uniform B-spline described in Eq. 4.8 is an example of such a mentioned 1D function. The tensor product of these 1D functions spans the space of the desired $\boldsymbol{k}$. As $\boldsymbol{k}$ is compactly supported most entries are equal to zero, and we can represent the non-zero elements by a tensor product of l translates of our 1D function. These translates are represented by $\boldsymbol{b}$. To be able to compute the inner

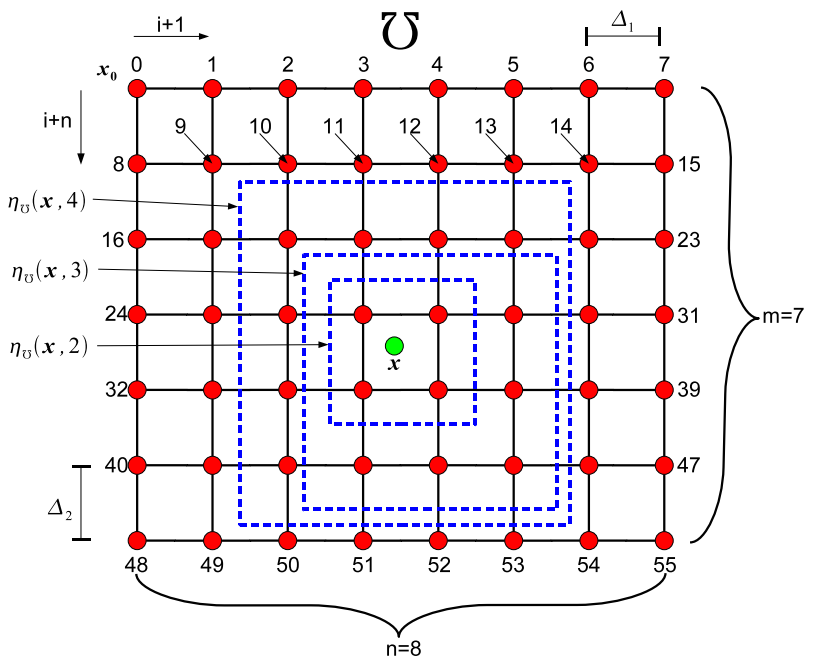

Figure 4.1: The neighborhood index operator returns the indices of the knots within blue box in a lexicographical ordering.

product between the non-zero elements of $\boldsymbol{k}(\boldsymbol{x})$ and the corresponding weights, we introduce the neighborhood index operator $\eta_{\mho}(\boldsymbol{x}, l)$ upon the lattice $\mho$ which returns the set of weight indices given $\boldsymbol{x}$. The functioning of the neighborhood index operator is illustrated in 4.1.

With the introduction of the above definitions it is possible to rewrite Eq. 4.2 to

$$\begin{aligned} I_{\mathcal{I}}(\boldsymbol{x}) &= \left\langle \boldsymbol{b}^{\otimes}(\tilde{\boldsymbol{x}}), \mathcal{W}_{\eta_{\mho}(\boldsymbol{x},l)} \right\rangle \\ &= \left\langle \boldsymbol{b}(\tilde{x}_N) \otimes \boldsymbol{b}(\tilde{x}_{N-1}) \otimes \ldots \otimes \boldsymbol{b}(\tilde{x}_1), \mathcal{W}_{\eta_{\mho}(\boldsymbol{x},l)} \right\rangle, \end{aligned} \tag{4.3}$$

where $\tilde{\boldsymbol{x}} = \rfloor \boldsymbol{x} \lfloor_{\mho}$, $\boldsymbol{b}(t)$ is a 1D basis function and $\mathcal{W}_{\eta_{\mho}(\boldsymbol{x},n+1)}$ is a vector containing the weights given by the neighborhood index operator.

An advantage of these basis functions is that the computation of the spatial

derivatives reduces to

$$\begin{aligned}\frac{\partial I_{\mathcal{I}}(\boldsymbol{x})}{\partial x_i} &= \left\langle \frac{\partial \boldsymbol{b}^{\otimes}(\tilde{\boldsymbol{x}})}{\partial x_i}, \mathcal{W}_{\eta_{\mathcal{K}\mathfrak{I}}(\boldsymbol{x},l)} \right\rangle \\ &= \left\langle \boldsymbol{b}(\tilde{x}_N) \otimes \ldots \otimes \Delta_i \frac{\partial \boldsymbol{b}(\tilde{x}_i)}{\partial \tilde{x}_i} \otimes \ldots \otimes \boldsymbol{b}(\tilde{x}_1), \mathcal{W}_{\eta_{\mathcal{K}\mathfrak{I}}(\boldsymbol{x},l)} \right\rangle . \quad (4.4)\end{aligned}$$

The special case, where $\mathcal{W} = \mathcal{I}$, is designated *classical interpolation*. Typical examples of basis functions, which satisfy the constraint, are the *linear interpolation kernel*, *cosine interpolation kernel* and the *Hermite cubic interpolation kernel*.

Linear interpolation kernel:

$$\boldsymbol{b}_{\text{lin}}(t) = \begin{bmatrix} 1-t \\ t \end{bmatrix} = \begin{bmatrix} 1 & -1 \\ 0 & 1 \end{bmatrix} \begin{bmatrix} 1 \\ t \end{bmatrix} \quad (4.5)$$

Cosine interpolation kernel:

$$\boldsymbol{b}_{\cos}(t) = \frac{1}{2} \begin{bmatrix} (1 + cos(\pi t)) \\ (1 - cos(\pi t)) \end{bmatrix} = \frac{1}{2} \begin{bmatrix} 1 & 1 \\ 1 & -1 \end{bmatrix} \begin{bmatrix} 1 \\ cos(\pi t)) \end{bmatrix} \quad (4.6)$$

Hermite cubic interpolation kernel:

$$\boldsymbol{b}_{\text{hrm}}(t) = \begin{bmatrix} 0 & \alpha & -2\alpha & \alpha \\ 1 & 0 & -\alpha - 3 & \alpha + 2 \\ 0 & -\alpha & 2\alpha + 3 & -\alpha - 2 \\ 0 & 0 & \alpha & -\alpha \end{bmatrix} \begin{bmatrix} 1 \\ t \\ t^2 \\ t^3 \end{bmatrix}, \quad (4.7)$$

where α controls the behavior of the cubic interpolator. Common choices of α ranges from -0.5 to -0.75. The recipe for constructing cubic interpolation splines was proposed by Keys [85].

Uniform B-splines or *basis splines* can be used as an alternative to the above kernels [72]. The jth basis B-spline of degree n defined upon the knot sequence $t_0 \leq t_2 \leq \ldots \leq t_m$ ($t_i \in [0\ 1]$) can be computed with the Cox-de Boor recursion formula [79]

$$b_{j,0}(t) = \begin{cases} 1 & \text{if } t_j \leq t < t_{j+1} \\ 0 & \text{otherwise} \end{cases} \quad (4.8)$$

$$b_{j,n}(t) = \frac{t - t_j}{t_{j+n} - t_j} b_{j,n-1}(t) + \frac{t_{j+n+1} - t}{t_{j+n+1} - t_{j+1}} b_{j+1,n-1}(t). \quad (4.9)$$

In the case of uniform B-splines (equivalent spaced knots t_i), the translates of degree 1, 2 and 3 are:

Linear B-spline kernel ($n = 1$):

$$\boldsymbol{b}_{\mathrm{bs1}}(t) = \begin{bmatrix} 1 & -1 \\ 0 & 1 \end{bmatrix} \begin{bmatrix} 1 \\ t \end{bmatrix} \tag{4.10}$$

Quadratic B-spline kernel ($n = 2$):

$$\boldsymbol{b}_{\mathrm{bs2}}(t) = \frac{1}{2} \begin{bmatrix} 1 & -2 & 1 \\ 1 & 2 & -2 \\ 0 & 0 & 1 \end{bmatrix} \begin{bmatrix} 1 \\ t \\ t^2 \end{bmatrix} \tag{4.11}$$

Cubic B-spline kernel ($n = 3$):

$$\boldsymbol{b}_{\mathrm{bs3}}(t) = \frac{1}{6} \begin{bmatrix} 1 & -3 & 3 & -1 \\ 4 & 0 & -6 & 3 \\ 1 & 3 & 3 & -3 \\ 0 & 0 & 0 & 1 \end{bmatrix} \begin{bmatrix} 1 \\ t \\ t^2 \\ t^3 \end{bmatrix} \tag{4.12}$$

To apply the B-splines for interpolation the weight coefficients have to be calculated, which requires computing the solution of a large but sparse linear system of equations. For the 1D cubic B-spline the linear system of equations becomes

$$\boldsymbol{B}\boldsymbol{w} = \frac{1}{6} \begin{bmatrix} 1 & 4 & 1 & 0 & \cdots & 0 \\ 0 & \ddots & \ddots & \ddots & \ddots & \vdots \\ \vdots & \ddots & \ddots & \ddots & \ddots & 0 \\ 0 & \cdots & 0 & 1 & 4 & 1 \end{bmatrix} \boldsymbol{w} = \mathcal{I}_{:}. \tag{4.13}$$

Note, this problem is under-resolved as there are $n+2$ columns but only n rows.

4.1.2 Short note on the boundary value problem

The boundary value problem arises in tensor spline interpolation when the size of the translates become larger than two. In these cases, the number of basis function required to interpolate the entire domain, surpasses the number of data samples, and the regression problem becomes ill-posed. This problem is redeemed by including a set of additional constraints on the boundary, called *boundary conditions*. Most common is probably the zero Dirichlet boundary condition which assumes that the weights of the knots placed outside the domain of the image are equal to zero. Hence, the first and last elements of $\boldsymbol{w}$ are

removed together with the first and last columns of $\boldsymbol{B}$

$$\boldsymbol{B}_{\text{zero}} = \frac{1}{6}\begin{bmatrix} 4 & 1 & 0 & \cdots & 0 \\ 1 & \ddots & \ddots & \ddots & \vdots \\ 0 & \ddots & \ddots & \ddots & 0 \\ \vdots & \ddots & \ddots & \ddots & 1 \\ 0 & \cdots & 0 & 1 & 4 \end{bmatrix}. \tag{4.14}$$

Another common boundary condition is the circular boundary condition, which in the 1D case means that the left neighbor of the left most knot in the lattice is the right most knot. The new $\boldsymbol{B}$ matrix becomes

$$\boldsymbol{B}_{\text{circ}} = \frac{1}{6}\begin{bmatrix} 4 & 1 & 0 & \cdots & 0 & 1 \\ 1 & \ddots & \ddots & \ddots & \ddots & 0 \\ 0 & \ddots & \ddots & \ddots & \ddots & \vdots \\ \vdots & \ddots & \ddots & \ddots & \ddots & 0 \\ 0 & \ddots & \ddots & \ddots & \ddots & 1 \\ 1 & 0 & \cdots & 0 & 1 & 4 \end{bmatrix} \tag{4.15}$$

Due to the uniformity of the knot placement (rectangular lattice) and the periodic boundary condition the system arising from $\boldsymbol{B}_{\text{circ}}$ can be solved quickly using the *discrete cosine transform*. The interested reader is referred to [171].

4.1.3 Scale-space

Scale-space theory provides a way of representing image structures at different scales. The motivation emerges from the fact that objects in the real-world appear different depending of the scale of observation. E.g. a snowflake will appear visually different depending on the distance from where it is observed. From afar it is just a white dot, but as you zoom in closer and closer a finer and finer ice crystal structure will appear with more and more branches. This is illustrated in Figure 4.2. In image registration you decrease the chance of falling into a local minimum dramatically by registering the coarser structures first and gradually incorporating finer and finer structures. In practice this is done by performing a sequence of image registrations in a course-to-fine manner, where the final result of scale k is used an initial guess on scale $k-1$.

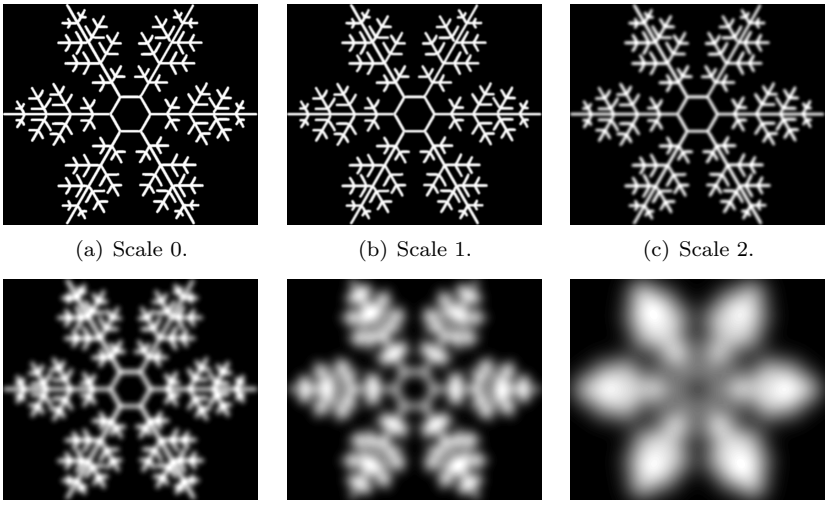

(a) Scale 0. (b) Scale 1. (c) Scale 2.

(d) Scale 3. (e) Scale 4. (f) Scale 5.

Figure 4.2: Scale space representation of a snowflake.

4.1.3.1 Gaussian scale-space

The most widely applied type of scale-space is the *Gaussian scale-space* which can be derived from a small set of scale-space axioms [96, 97]. In Gaussian scale-space a sequence of signals $\{L(\boldsymbol{x}, t)\}$ is derived from an image $I(\boldsymbol{x})$ by convolving the image with the Gaussian kernel $G(\boldsymbol{x}, t) = \frac{1}{\sqrt{2\pi t}^N} e^{-\frac{1}{2t}\|\boldsymbol{x}\|^2}$

$$L(\boldsymbol{x}, t) = G(\boldsymbol{x}, t) * I(\boldsymbol{x}). \tag{4.16}$$

4.1.3.2 Smoothing splines

As an alternative to Gaussian scale-space one can merge the concept of scale-space with the concept of an interpolator using *smoothing splines* [79]. That is instead of solving a linear system equation to get the weights $\boldsymbol{w}$ from Eq. 4.2 we compute

$$\arg\min_{w} \|\mathcal{I}_{:} - \boldsymbol{K}\boldsymbol{w}\|^2 + \alpha\|\boldsymbol{w}\|_{\Theta}^2, \tag{4.17}$$

where

$$\Theta = \sum_{i=1}^{N}\sum_{j=1}^{N}\int_{\Omega} \frac{\partial^2 \boldsymbol{k}(\boldsymbol{x})}{\partial x_i \partial x_j} \frac{\partial^2 \boldsymbol{k}(\boldsymbol{x})}{\partial x_i \partial x_j}^T d\boldsymbol{x} \tag{4.18}$$

and $\boldsymbol{K} = [\boldsymbol{k}(\boldsymbol{x_1}) \ldots \boldsymbol{k}(\boldsymbol{x}_n)]^T$ and α is a smoothing parameter. The last term of E.q. 4.17 penalizes curvature.

4.2 Geometrical Transformation

As mentioned, it is customary to distinguish between two general types of geometrical transformation representations. The non-parametric representation stores a displacement for every single point in some chosen mesh topology with a suitable resolution, and the parametric representation represents the entire deformation field or transformation with a finite number of parameters. The advantages with the parametric representation are the inherit dimensionality reduction and the fact that the transformation derivatives can be computed directly, while they have to be approximated using e.g. finite differences in the non-parametric case. These advantages will often lead to a faster and a more stable optimization. On the other hand, the non-parametric representation can represent *any* transformation down to some resolution, while it may difficult to find a suitable parametric representation for complex deformations. The best choice of representation is naturally depended on the application – e.g. if you tracking the 2D rigid motion of an object there are only three degrees of freedom (one rotation and two translations), which implies that the displacement field can be modeled using only three parameters.

Independent of your choice of representation a rule of thumb in medical image registration is that a transformation as a minimum should be *diffeomorphic*. The word diffeomorphic is a contraction of *differentiable* and *homeomorphic*.

Definition 4.5 (Diffeomorphism) A function f between two topological spaces X and Y is called a *diffeomorphism* if

- f is a bijection
- f and the inverse mapping f^{-1} are $\mathcal{C}^1$.

The diffeomorphism definition translates into the requirement that a deformation field has to be *smooth* and may not contain *tears* or *folds*. If f and the inverse mapping f^{-1} are only $\mathcal{C}^0$, we say that f is a *homeomorphism*.

The diffeomorphism constraints surface due to practical circumstances rather

than from real demands. In inter-subject image registration of biological objects the homeomorphism assumption may even conflict with reality. There may be structures in the human brain of one individual which do not exist in the brain of another individual, and some pigs have more ribs than others. The lack of topological equivalence between images is difficult to handle so we simply choose to ignore it. How do you represent a transformation where a displacement in a point $\boldsymbol{x}$ may or may not exists, and how do we detect it? And even if we could handle topological difference problems, we often want to do statistical analysis on the displacement fields afterwards. The lack of one-to-one correspondence can easily complicate the statistical analysis. At last, it is impossible to apply a gradient based optimization technique if the transformation is not differentiable.

4.2.1 Parametric representation

All parametric transformations used in this thesis are on the form

$$\boldsymbol{\phi}(\boldsymbol{x};\boldsymbol{w}) = \boldsymbol{x} + \boldsymbol{u}(\boldsymbol{x};\boldsymbol{w}) = \boldsymbol{x} + \boldsymbol{A}(\boldsymbol{x})\boldsymbol{g}(\boldsymbol{w}), \tag{4.19}$$

where $\boldsymbol{A}$ is a spatial basis and $\boldsymbol{g}$ is a parameter kernel.

If $\boldsymbol{A}$ is linearly dependent on $\boldsymbol{x}$ we say that the transformation is *linear* w.r.t. $\boldsymbol{x}$, i.e.

$$\boldsymbol{A}_{\text{lin}} = \begin{bmatrix}\boldsymbol{x}^T & 1\end{bmatrix} \otimes \boldsymbol{I}. \tag{4.20}$$

Typical linear transformations are the *rigid* transformation, the *similarity* transformation and the *affine* transformation. In 3D these transformations are given by the following parameter basis

$$\begin{aligned}
\boldsymbol{g}_{\text{sim}}\left(\begin{bmatrix}\boldsymbol{\alpha}\\ s\\ \boldsymbol{t}\end{bmatrix}\right) &= s\begin{bmatrix}\text{vect}\left(\prod_{i=1}^{3}\boldsymbol{R}_i(\alpha_i) - \boldsymbol{I}\right)\\ \boldsymbol{t}\end{bmatrix},\\
\boldsymbol{g}_{\text{rig}}\left(\begin{bmatrix}\boldsymbol{\alpha}\\ \boldsymbol{t}\end{bmatrix}\right) &= \boldsymbol{g}_{\text{sim}}\left(\begin{bmatrix}\boldsymbol{\alpha}\\ 1\\ \boldsymbol{t}\end{bmatrix}\right),\\
\boldsymbol{g}_{\text{aff}}(\boldsymbol{w}) &= \boldsymbol{w},
\end{aligned}$$

where $\boldsymbol{\alpha}$ are the rotation angles, $\boldsymbol{t}$ are the translations, $\boldsymbol{R}_i$ is the 2D rotation around the ith axis and s is the scale parameter.

$\boldsymbol{\phi}(\boldsymbol{x};\boldsymbol{w})$ models a non-rigid deformation when $\boldsymbol{A}$ has a non-linear dependency on $\boldsymbol{x}$. To ensure a fast evaluation it is customary to construct $\boldsymbol{A}$ from *compactly supported* basis functions, e.g. B-spline basis functions. If the knots of the basis functions are placed in a rectangular lattice topology it is most natural to use

the basis functions presented in Section 4.1.1 *Interpolation of regularly sampled data*. Compactly supported radial basis functions are another type of basis function which have been used frequently for modeling deformation in image registration [60, 61, 65, 102, 126, 146].

Most choices of $\boldsymbol{A}$ will guarantee that $\boldsymbol{\phi}$ is smooth with no tears, but there is no guarantee that it will not fold. If $\boldsymbol{A}$ is non-linear w.r.t. $\boldsymbol{x}$ and $\boldsymbol{\phi}$ is linear w.r.t. $\boldsymbol{w}$, e.g. $\boldsymbol{g}(\boldsymbol{w}) = \boldsymbol{w}$, then there exists an instance of $\boldsymbol{w}$ which produces a folding instance of $\boldsymbol{\phi}$ [78]. It is possible to construct a mapping $\boldsymbol{g} : \mathbb{R}^M \to \mathcal{P} \subset \mathbb{R}^M$, where $\mathcal{P}$ is a bounded subset of $\mathbb{R}^M$, which ensures that $\boldsymbol{\phi}$ is diffeomorphic for all $\boldsymbol{w}$. The included paper *Diffeomorphic Statistical Deformation Models* (Chapter 10) proposes a general solution to this problem.

4.3 Regularization

In this thesis all regularizers will be in the form

$$\mathcal{S}[\phi] = \int_{\Omega} r(\boldsymbol{\phi}; \boldsymbol{x}) d\boldsymbol{x}, \tag{4.21}$$

where $r(\boldsymbol{\phi}; \boldsymbol{x})$ is a *regularization density* function.

This thesis work has primarily been focussed on elastic regularization and secondarily on regularization from statistical priors on the displacement parameters. The section gives a thorough description of *elastic* regularization and a basic introduction to *Tikhonov* regularization for reasons of completeness. For details about regularization from statistical priors and statistical prior building the reader is referred to the included paper *Conditional Statistical Model Building* (Chapter 11).

4.3.1 Tikhonov based regularization

The simplest type of regularization is probably a quadratic penalty on the displacements

$$r_{\text{quad}}(\boldsymbol{\phi}; \boldsymbol{x}) = \|\boldsymbol{\phi}(\boldsymbol{x}) - \boldsymbol{x}\|^2_{\boldsymbol{Q}} = \|\boldsymbol{u}(\boldsymbol{x})\|^2_{\boldsymbol{Q}}. \tag{4.22}$$

where $\boldsymbol{Q}$ is a quadratic weighting matrix. This regularizer is for several reasons not suitable for image registration:

- It is not rotation or scale invariant. Semi-rigid deformation accounts for a significant part of the total deformation in many IRPs.

- It treats the displacement penalty in every point $\boldsymbol{x}$ independently. It is likely to assume that the displacement at $\boldsymbol{x}$ is correlated with the displacement of its neighborhood. In the case of parametric registration, it may not be such a big problem as the basis functions already model the correlation between neighboring points. Nevertheless, it makes little theoretical sense to assume correlation between neighboring points and then discard it. With a parametric representation of the transformation one could apply Tikhonov regularization directly on the displacement parameters $\boldsymbol{w}$

$$\mathcal{S}_{par}[\phi] = \|\boldsymbol{\Gamma}\boldsymbol{w}\|^2 = \|\boldsymbol{w}\|^2_{\boldsymbol{Q}}, \;\; \boldsymbol{Q} = \boldsymbol{\Gamma}^T\boldsymbol{\Gamma}, \tag{4.23}$$

  where $\boldsymbol{\Gamma}$ is the Tikhonov matrix.

To redeem the latter of the problems, it is possible to change the quadratic regularizer to work on the relative displacements represented by the displacement gradient $\nabla\boldsymbol{u}$

$$r_{\text{der}}(\boldsymbol{\phi};\boldsymbol{x}) = \|\text{vect}(\nabla\boldsymbol{u}(\boldsymbol{x}))\|^2_{\boldsymbol{Q}}. \tag{4.24}$$

For $\boldsymbol{Q} = \boldsymbol{I}$, this regularizer is known as the *diffusive regularizer* [56, 108]. The name diffusive regularizer originates from the observation that a generalized version of the diffusion equation can be obtained from the combination of Eq. 4.1 and Eq. 4.24 by setting the Gâteaux derivatives of Eq. 4.1 equal to zero.

The regularizer given by Eq. 4.24 will after discretization reduce to Eq. 4.23 in the case of parametric registration, and to the Tikhonov form

$$\mathcal{S}_{\text{tik}}[\boldsymbol{\phi}] = \|\boldsymbol{\Gamma}\hat{\boldsymbol{u}}\|^2 \tag{4.25}$$

in the case non-parametric registration, where $\boldsymbol{\Gamma}$ serves as a linearized differentiation operator with built-in weighting and $\hat{\boldsymbol{u}}$ is the discretized displacement field.

4.3.2 Elastic regularization

In physics, an elastic material will deform under *stress* (e.g. from external forces) but revert to its original shape when the stress is removed. The amount of relative displacement between neighboring particles is known as the *strain*. It is important to think of stress and strain as concepts rather than specific physical quantities as there are several ways of representing and defining them. Elastic deformation modeling is essentially a problem of relating stress to strain. This simplest way of relating stress and strain is through *Hooke's law* which states that stress and strain are proportional to each other. This is known as *linear elasticity*. For *hyperelastic* materials, the relationship between stress and strain

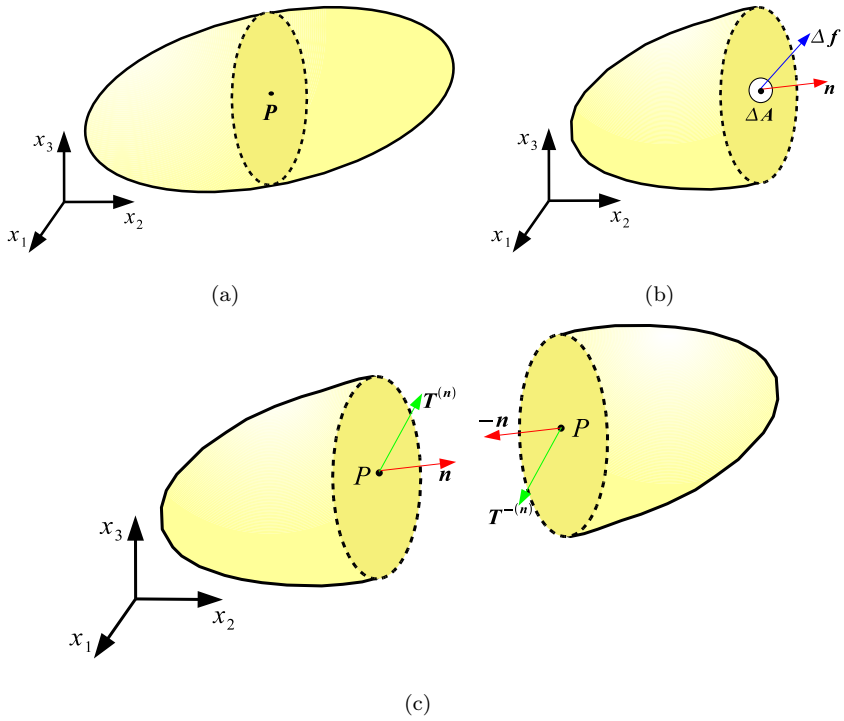

Figure 4.3: Stress illustration.

is modeled through a *strain energy density* function (elastic potential energy). The theory of elasticity covered in this thesis has been compiled from a number of articles and books [20, 50, 108, 122] and the author's own interpretation. For in-depth descriptions of the concepts of stress and strain the reader is referred to [50].

4.3.2.1 Cauchy Stress

Stress is the internal distribution of force per area which balances and reacts with the external forces. Let us assume that a body has been separated into a left and a right part by an imaginary plane defined by the point P and the normal $\boldsymbol{n}$ as shown in Figure 4.3. Due to the internal reaction the left part exerts a total force $\Delta \boldsymbol{f}$ in an area ΔA on the right part. If the body is in a state of equilibrium (no motion) the right part will exert an equally sized and opposite directional force on the left part. According to the *Cauchy stress principle* the limit of the ratio between $\Delta \boldsymbol{f}$ and ΔA, when ΔA shrinks around P, exists, and

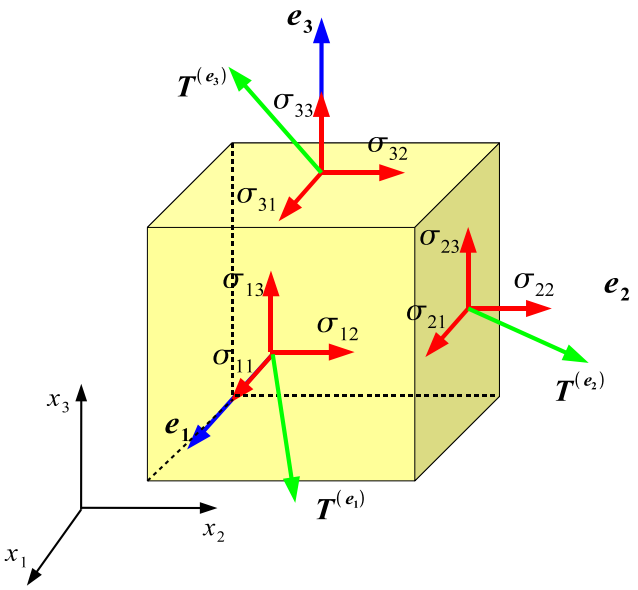

Figure 4.4: Stress tensor illustrated on an infinitesimally small cube.

the limit is called the *traction* or *stress vector* at the shrinkage point P

$$\boldsymbol{T}^{(\boldsymbol{n})} = \lim_{\Delta A \to 0} \frac{\Delta \boldsymbol{f}}{\Delta A} = \frac{d\boldsymbol{f}}{dA}. \tag{4.26}$$

The stress in a 3D body can by represented by a second-order Cartesian tensor defined in the reference coordinate system $V = \text{span}\{\boldsymbol{e}_1, \boldsymbol{e}_2, \boldsymbol{e}_3\}$

$$[\sigma_{ij}] = \begin{bmatrix} T^{(\boldsymbol{e}_1)} \\ T^{(\boldsymbol{e}_2)} \\ T^{(\boldsymbol{e}_3)} \end{bmatrix} = \begin{bmatrix} \sigma_{11} & \sigma_{12} & \sigma_{13} \\ \sigma_{21} & \sigma_{22} & \sigma_{23} \\ \sigma_{31} & \sigma_{32} & \sigma_{33} \end{bmatrix}. \tag{4.27}$$

$[\sigma_{ij}]$ is known as the *Cauchy stress tensor*. An illustration of the Cauchy stress tensor can be found in Figure 4.4. σ_{ii} and σ_{ij} with $i \neq j$ are entitled the normal stresses and the shear stresses, respectively. When the body is in an equilibrium state the shear stresses are equal across the diagonal elements $\sigma_{ij} = \sigma_{ji}$. As we are only interested in the final configuration of the deformed (registered) image and not the deformation path itself, this thesis will only deal with symmetric stress tensors. Thus, it is natural to represent the stress tensor by $\boldsymbol{\sigma} = \text{vect}([\sigma_{ij}]) = [\sigma_{11}\ \sigma_{22}\ \sigma_{33}\ \sigma_{12}\ \sigma_{13}\ \sigma_{23}]^T$.

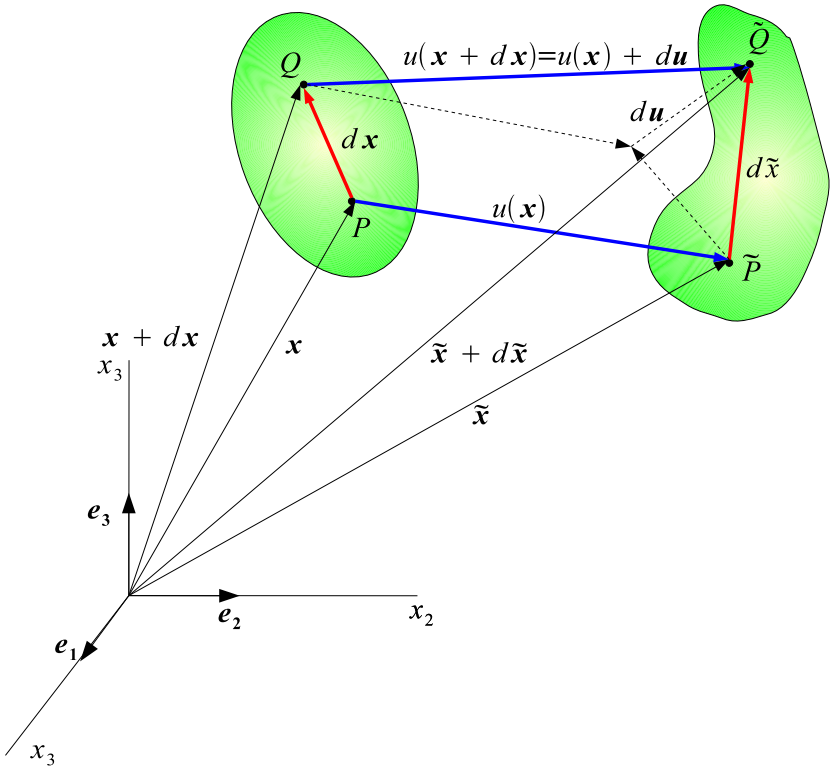

Figure 4.5: Deformation of a continuum body.

4.3.2.2 Deformation and strain

Consider the point P and the neighboring point Q in a material positioned at $\boldsymbol{x}$ and $\boldsymbol{x} + \Delta\boldsymbol{x}$, respectively. The material body undergoes a diffeomorphic deformation such that the points P and Q move to positions $\widetilde{P}$ and $\widetilde{Q}$ given by $\widetilde{\boldsymbol{x}}$ and $\widetilde{\boldsymbol{x}} + \Delta\widetilde{\boldsymbol{x}}$. Assuming that $\Delta\boldsymbol{x}$ and $\Delta\widetilde{\boldsymbol{x}}$ are infinitesimally small they can be replaced by $d\boldsymbol{x}$ and $d\widetilde{\boldsymbol{x}}$.

From Figure 4.5 it follows that

$$\begin{aligned} \widetilde{\boldsymbol{x}} + d\widetilde{\boldsymbol{x}} &= \boldsymbol{x} + d\boldsymbol{x} + \boldsymbol{u}(\boldsymbol{x} + d\boldsymbol{x}) \Leftrightarrow & (4.28)\\ d\widetilde{\boldsymbol{x}} &= \boldsymbol{x} - \widetilde{\boldsymbol{x}} + d\boldsymbol{x} + \boldsymbol{u}(\boldsymbol{x} + d\boldsymbol{x}) & (4.29)\\ &= d\boldsymbol{x} + \boldsymbol{u}(\boldsymbol{x} + d\boldsymbol{x}) - \boldsymbol{u}(\boldsymbol{x}). & (4.30) \end{aligned}$$

$d\boldsymbol{u} = u(\boldsymbol{x} + d\boldsymbol{x}) - u(\boldsymbol{x})$ is called the *relative displacement*. By performing a

first-order Taylor expansion of $\boldsymbol{u}(\boldsymbol{x}+d\boldsymbol{x})$ around P we get

$$d\widetilde{\boldsymbol{x}} \approx d\boldsymbol{x} + \boldsymbol{u}(\boldsymbol{x}) + \nabla_{\boldsymbol{x}}\boldsymbol{u}(\boldsymbol{x})d\boldsymbol{x} - \boldsymbol{u}(\boldsymbol{x}) = (\boldsymbol{I} + \nabla_{\boldsymbol{x}}\boldsymbol{u}(\boldsymbol{x}))d\boldsymbol{x} = \boldsymbol{F}(\boldsymbol{x})d\boldsymbol{x} \quad (4.31)$$

The tensor $\boldsymbol{F}(\boldsymbol{x}) = \nabla\boldsymbol{\phi}(\boldsymbol{x}) = \boldsymbol{I} + \nabla\boldsymbol{u}(\boldsymbol{x})$ is called the *material deformation gradient tensor* and describes the local deformation at the material point given by the position $\boldsymbol{x}$. As the tensor $\boldsymbol{F}$ is based on the displacement gradient it is translation invariant but not rotation invariant. However, $\boldsymbol{F}$ can be decomposed into an orthonormal tensor (representing the rotation) and a positive definite symmetric tensor (representing the stretch), i.e.

$$\boldsymbol{F} = \boldsymbol{R}\boldsymbol{U} = \boldsymbol{V}\boldsymbol{R}. \quad (4.32)$$

$\boldsymbol{U}$ and $\boldsymbol{V}$ are denoted the *right stretch tensor* and the *left stretch tensor* respectively. $\boldsymbol{U}$ and $\boldsymbol{V}$ have identical eigenvalues or *principal stretches* but different eigenvectors. The decomposition is illustrated in Figure 4.6

From the right stretch tensor we define a sequence of rotation and translation invariant tensors which are known as the *Lagrangian strain tensors*

$$\boldsymbol{E}_m = \frac{1}{2m}(\boldsymbol{U}^{(2m)} - \boldsymbol{I}). \quad (4.33)$$

These tensors essentially model the deviation of the right stretch tensor from the identity. The special case $\boldsymbol{E}_0 = \log(\boldsymbol{U})$ is called the *Hencky strain tensor* and is by many considered to be the natural strain tensor. The special case E_1 is called the *Green-Lagrangian tensor* or the *Green - St-Venant strain tensor* and is often written in the form

$$\boldsymbol{E}_1 = \frac{1}{2}(\boldsymbol{C} - \boldsymbol{I}), \quad (4.34)$$

where $\boldsymbol{C} = \boldsymbol{F}^T\boldsymbol{F}$ is the *right Cauchy-Green deformation tensor.*

4.3.3 *Hooke's law* and linear elasticity

After having visited stress and strain it is time to link the two concepts together. The theory of elasticity is governed by *Hooke's law* which states that the restoring force in a spring is directly proportional to extension or compression of the spring. As stress is related to force and strain to deformation the extension of *Hooke's law* to a 3D elastic material becomes

$$\begin{bmatrix}\sigma_{11}\\ \sigma_{22}\\ \sigma_{33}\\ \sigma_{12}\\ \sigma_{13}\\ \sigma_{23}\end{bmatrix} = \begin{bmatrix} s_{11} & \cdots & s_{16}\\ \vdots & \ddots & \vdots\\ s_{61} & \cdots & s_{66}\end{bmatrix}\begin{bmatrix}\epsilon_{11}\\ \epsilon_{22}\\ \epsilon_{33}\\ \epsilon_{12}\\ \epsilon_{13}\\ \epsilon_{23}\end{bmatrix}, \quad (4.35)$$

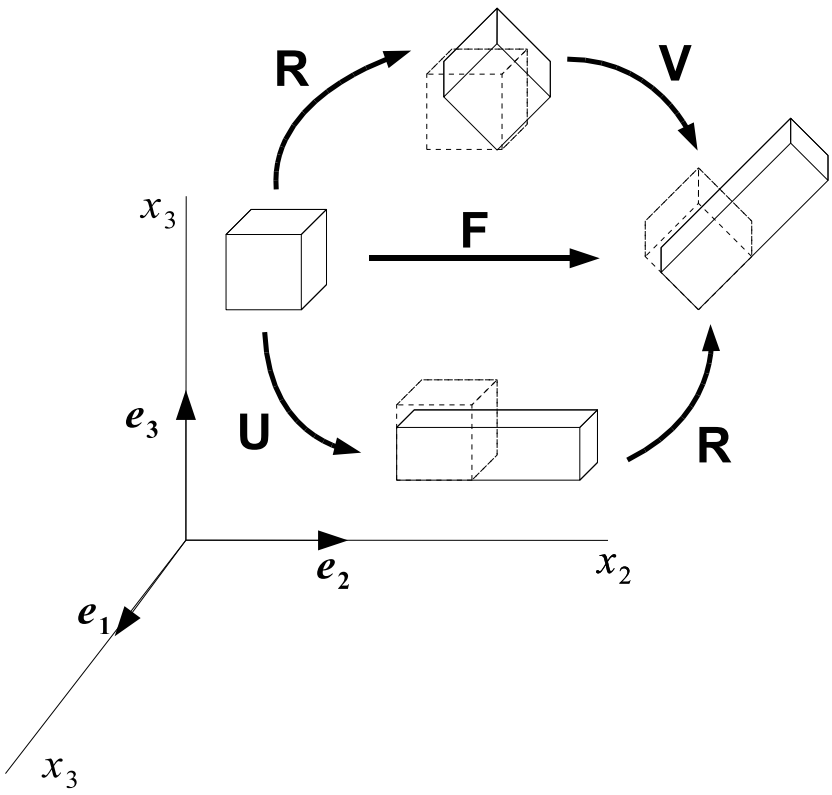

Figure 4.6: Polar decomposition of material deformation gradient tensor.

where $\boldsymbol{S} = [s_{ij}]$ is the stiffness matrix and ϵ_{ij} is the ijth element of the strain tensor. As the stress and strain tensors have 6 unique components the stiffness matrix is a 6×6 matrix which gives a total of 36 degrees of freedom. For an isotropic elastic material the stress and strain tensors share principal axes which implies that the linear relationship can be expressed through the principal components of the tensors. Hence,

$$\begin{bmatrix} \sigma_1 \\ \sigma_2 \\ \sigma_3 \end{bmatrix} = \begin{bmatrix} \tilde{s}_{11} & \tilde{s}_{12} & \tilde{s}_{13} \\ \tilde{s}_{21} & \tilde{s}_{22} & \tilde{s}_{23} \\ \tilde{s}_{31} & \tilde{s}_{32} & \tilde{s}_{33} \end{bmatrix} \begin{bmatrix} \epsilon_1 \\ \epsilon_2 \\ \epsilon_3 \end{bmatrix}, \tag{4.36}$$

where σ_i is the ith principal component of the stress tensor and ϵ_i is the ith principal component of the strain tensor. Furthermore, as the reaction must be independent of the direction, the diagonal elements of $[\tilde{s}_{ij}]$ must be equal and the off-diagonal elements of $[\tilde{s}_{ij}]$ must be equal. This leaves only two degrees of freedom for the case of an isotropic elastic material - yielding Hooke's law for an isotropic elastic material

$$\begin{bmatrix} \sigma_{11} \\ \sigma_{22} \\ \sigma_{33} \\ \sigma_{12} \\ \sigma_{13} \\ \sigma_{23} \end{bmatrix} = \begin{bmatrix} \lambda+\mu & \lambda & \lambda & 0 & 0 & 0 \\ \lambda & \lambda+\mu & \lambda & 0 & 0 & 0 \\ \lambda & \lambda & \lambda+\mu & 0 & 0 & 0 \\ 0 & 0 & 0 & 2\mu & 0 & 0 \\ 0 & 0 & 0 & 0 & 2\mu & 0 \\ 0 & 0 & 0 & 0 & 0 & 2\mu \end{bmatrix} \begin{bmatrix} \epsilon_{11} \\ \epsilon_{22} \\ \epsilon_{33} \\ \epsilon_{12} \\ \epsilon_{13} \\ \epsilon_{23} \end{bmatrix} = \boldsymbol{\Upsilon} \begin{bmatrix} \epsilon_{11} \\ \epsilon_{22} \\ \epsilon_{33} \\ \epsilon_{12} \\ \epsilon_{13} \\ \epsilon_{23} \end{bmatrix} \tag{4.37}$$

where μ and λ are the *Lamé* constants.

In *linear elasticity* it is customary to model stress with the *Cauchy's strain tensor*

$$\boldsymbol{E}_{\text{lin}} = \frac{1}{2}(\nabla \boldsymbol{u}(\boldsymbol{x})^T + \nabla \boldsymbol{u}(\boldsymbol{x})). \tag{4.38}$$

For an infinitesimal deformation $\|u(\boldsymbol{x})\| \ll 1$, $\|\nabla u(\boldsymbol{x})\| \ll 1$, the Cauchy's strain tensor is an approximation to the Green-Lagrangian tensor

$$\begin{aligned} \boldsymbol{E}_1 &= \frac{1}{2}(\boldsymbol{F}^T\boldsymbol{F} - \boldsymbol{I}) = \frac{1}{2}(\nabla \boldsymbol{u}(\boldsymbol{x})^T + \nabla \boldsymbol{u}(\boldsymbol{x}) + \nabla \boldsymbol{u}(\boldsymbol{x})^T \nabla \boldsymbol{u}(\boldsymbol{x})) \\ &\approx \frac{1}{2}(\nabla \boldsymbol{u}(\boldsymbol{x})^T + \nabla \boldsymbol{u}(\boldsymbol{x})) = \boldsymbol{E}_{\text{lin}}. \end{aligned}$$

The *linearized elastic potential energy* for an isotropic material is derived by integration of Eq. 4.37

$$W_{\text{lin}}(\boldsymbol{x}) = \|\text{vect}(\boldsymbol{E}_{\text{lin}})\|^2_{\Upsilon} = \mu \text{tr}(\boldsymbol{E}^2_{\text{lin}}(\boldsymbol{x})) + \frac{\lambda}{2}\text{tr}(\boldsymbol{E}_{\text{lin}}(\boldsymbol{x}))^2. \tag{4.39}$$

The use of linear elasticity in image matching was initially proposed by Chaim Broit in his doctoral dissertation [24] in 1981 and refined over the following years

by Bajcsy et al. [13–15, 141]. The linear elastic model with the Cauchy's strain tensor is still today the most widely used model in surgical simulators despite some limitations. The main drawback of linear elasticity is its lack of rotation invariance which is due to the small deformation assumption inherited from the use of Cauchy's strain tensor. Lets assume that a solid 2D body undergoes a rotation

$$\phi(\boldsymbol{x}) = \boldsymbol{R}\boldsymbol{x} = \boldsymbol{x} + (\boldsymbol{R} - \boldsymbol{I})\boldsymbol{x},\ \boldsymbol{R}^T\boldsymbol{R} = \boldsymbol{I},\ \boldsymbol{x} \in \mathbb{R}^2. \tag{4.40}$$

By inserting Eq. 4.40 into Eq. 4.38 we get

$$\boldsymbol{E}_{\text{lin}} = \frac{1}{2}(\boldsymbol{R}^T + \boldsymbol{R} - 2\boldsymbol{I}) = (\cos(\alpha) - 1)\boldsymbol{I} \tag{4.41}$$

and

$$W_{\text{lin}}(\boldsymbol{x}) = 2\mu(\cos(\alpha)^2 + 1 - 2\cos(\alpha)) + 2lambda(\cos(\alpha) - 1), \tag{4.42}$$

which shows that the energy is depended on the rotation angle α.

4.3.3.1 Hyperelastic

For hyperelastic materials the *strain energy density* function is the instrument in which the relationship between stress and strain is modeled. The definition of elasticity informs us, that work associated with a deformation of an elastic body is independent on deformation path, and only depends on the end configuration given by the deformation gradient $\boldsymbol{F}$. The strain energy density function quantifies the work/energy stored in an infinitesimal neighborhood due to the deformation. Hence, the strain energy density function $W(\boldsymbol{F})$ is a function of $\boldsymbol{F}$.

There are a number of requirements which one should take into account when designing a strain energy density function. First of all the energy should be zero in a stress free state (rotation invariance) and it should be monotonically increasing

$$W(\boldsymbol{F}) = 0 \text{ for } \boldsymbol{C} = \boldsymbol{F}^T\boldsymbol{F} = \boldsymbol{I} \text{ and } W(\boldsymbol{F}) \geq 0. \tag{4.43}$$

Furthermore, it should take an infinite amount of energy to do an infinite expansion and to do a *black hole* (collapse) deformation

$$W(\boldsymbol{F}) \to \infty \text{ for } \det(\boldsymbol{F}) \to \infty \text{ and for } \det(\boldsymbol{F}) \to 0. \tag{4.44}$$

If $\bar{W}(\boldsymbol{E}) = W(\boldsymbol{F})$ is a strain energy density function defined upon a some tensor $\boldsymbol{E}$ then the energy conjugate stress tensor is defined by

$$[\sigma_{ij}]_{\boldsymbol{E}} = \frac{\partial \bar{W}(\boldsymbol{E})}{\partial \boldsymbol{E}}. \tag{4.45}$$

The easiest way to design an energy function is probably just to define it in terms of the length or size of a suitable tensor $\boldsymbol{E}$. E.g. we can use the squared Fröbenius norm as the strain energy density function

$$\bar{W}_{\text{fro}}(\boldsymbol{E};\boldsymbol{x}) = \frac{1}{2}\|\boldsymbol{E}(\boldsymbol{x})\|^2_{\text{fro}} = \frac{1}{2}\text{tr}(\boldsymbol{E}(\boldsymbol{x})^2). \tag{4.46}$$

Many biological structures and shapes will often exhibit a preferred direction of deformation in the reference coordinate system. If such a priori information is available it is natural to base the energy function on the weighted quadratic form

$$\bar{W}_{\text{wgh}}(\boldsymbol{E};\boldsymbol{x}) = \|\text{vect}(\boldsymbol{E}(\boldsymbol{x}))\|^2_{\boldsymbol{Q}(\boldsymbol{x})}. \tag{4.47}$$

In the case of isotropic materials the above form can be rewritten into

$$\bar{W}_{\text{iso}}(\boldsymbol{E};\boldsymbol{x}) = \mu\text{tr}(\boldsymbol{E}(\boldsymbol{x})^2) + \frac{\lambda}{2}\text{tr}(\boldsymbol{E}(\boldsymbol{x}))^2, \tag{4.48}$$

where μ and λ are the *Lamé* constants. Note, the similarity to linearized elastic potential energy in Eq. 4.39.

The strain energy density function of an isotropic material is normally defined using the invariants[2] of the deformation and strain tensors. That is, the energy is expressed by unbiased combinations of the principal stretches (eigenvalues of $\boldsymbol{U}$). Common invariants are $I_1^E = \text{tr}(\boldsymbol{E})$, $I_2^E = \text{tr}(\boldsymbol{E}^2) - \text{tr}(\boldsymbol{E})^2$ and $I_3^E = \det(\boldsymbol{E})$.

4.3.3.2 Examples of isotropic elastic regularizers

The most natural isotropic regularizer to start with is the *St. Venant Kirchoff elasticity energy* [123]

$$r_{\text{svk}}(\boldsymbol{\phi};\boldsymbol{x}) = \bar{W}_{\text{iso}}(\boldsymbol{E}_1;\boldsymbol{x}) = \frac{\mu}{4}\sum_{i=1}^{N}(\varepsilon_i^2 - 1)^2 + \frac{\lambda}{8}\left(\sum_{i=1}^{N}(\varepsilon_i^2 - 1)\right)^2, \tag{4.49}$$

which is the extension of linear elasticity to large deformations. $\boldsymbol{\varepsilon}$ is the principal stretches. In contrast to linear elasticity, this energy is rotation invariant but its ability to handle large compression is questionable, i.e.

$$\bar{W}_{\text{iso}}(\boldsymbol{E}_1;\boldsymbol{x}) = \frac{N\mu}{4} + \frac{N^2\lambda}{8} \tag{4.50}$$

[2]Invariant w.r.t. reference frame.

when $\det(\boldsymbol{F}(\boldsymbol{x})) = 0$. Hence, it does not take an infinite amount of energy to do the back hole deformation. The energy as function of the principal stretches is visualized in Figures 4.7) with different material constants. From the figure we observe that the elasticity energy grows faster for expansion than compression.

Pennec et al. [122] proposed to replace the Green-Lagrangian tensor with the Hencky strain tensor and hereby introduced the *isotropic Riemannian elasticity energy*

$$r_{\text{rie}}(\boldsymbol{\phi}; \boldsymbol{x}) = \bar{W}_{\text{iso}}(\boldsymbol{E}_0; \boldsymbol{x}) = \frac{\mu}{2} \sum_{i=1}^{N} \log^2 \varepsilon_i + \frac{\lambda}{4} \left(\sum_{i=1}^{N} \log \varepsilon_i \right)^2 . \tag{4.51}$$

The Riemannian elasticity energy fulfills the requirements from Eq. 4.43 and Eq. 4.44. The energy as function of the principal stretches is visualized in Figure 4.8 with different material constants. From the figure, we observe that Riemannian elasticity energy almost mirrors the St. Vernant Kirchoff energy in the bottom-left to top-right diagonal in the displayed interval of the principal stretches, and that the energy landscape of the Riemannian elasticity energy matches the no-compression line.

It is possible exploit the incompressibility constraint $\det(\boldsymbol{F}) = 1$ to build a strain density energy function, i.e.

$$r_{\text{vol}}(\boldsymbol{\phi}; \boldsymbol{x}) = (\det(\boldsymbol{F})^K - 1)^{2M} = (\prod_{i=1}^{N} \varepsilon_i^K - 1)^{2M}, \tag{4.52}$$

where K and M are material constants. For $M > 0$ and $K \neq 0$, r_{vol} penalizes changes in volume. This energy as function of the principal stretches is visualized in Figure 4.9(a,b) with different material constants. For $K > 0$, this volumetric elasticity energy suffers from the same black hole defect as St. Venant Kirchoff elasticity energy.

Rohlfing et al. [128] used the absolute value of natural logarithm of the determinant of the deformation gradient as a soft constraint for the registration of pre-contrast and post-contrast MR breast images. A generalized version of this regularizer is

$$r_{\log}(\boldsymbol{\phi}; \boldsymbol{x}) = \log(\det(F))^{2M} = \left(\sum_{i=1}^{N} \log \varepsilon_i \right)^{2M} , \tag{4.53}$$

where M is a material constant. Note, for $M = 1$ this energy is equal to the second term of isotropic Riemannian elasticity energy (see Eq. 4.51). This energy as function of the principal stretches is visualized in Figure 4.9(c) with

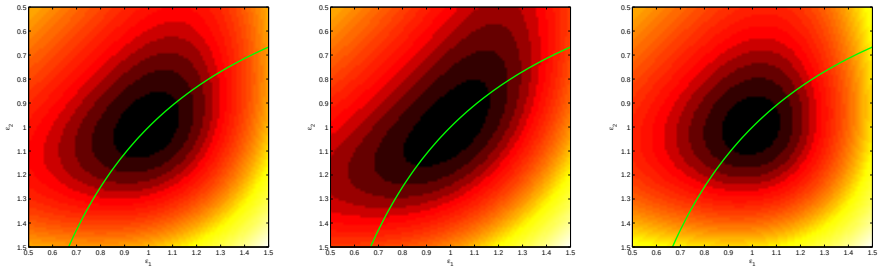

(a) r_{svk}, $\lambda = 1$, $\mu = 1$ (b) r_{svk}, $\lambda = 1$, $\mu = 3$ (c) r_{svk}, $\lambda = 3$, $\mu = 1$

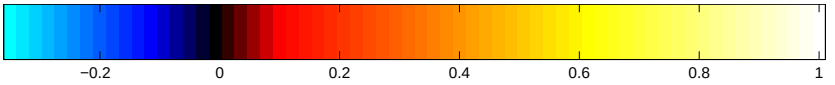

(d) Colorbar.

Figure 4.7: The St. Vernant Kirchoff density energy as a function of the principal stretches ε_1 and ε_2. The green line represents the no compression cases ($\det(\boldsymbol{F}) = \varepsilon_1\varepsilon_2 = 1$).

material constant $M = 1$. As could be expected the volumetric energies in Figure 4.9 follows the no-compression line.

Biological tissue behaves similar to natural rubber which means that is nearly incompressible and very compliant to shear. The best model for describing rubber-like materials is the *Ogden material model* [115]

$$r_{\text{ogden}}(\boldsymbol{\phi}; \boldsymbol{x}) = \sum_{p=1}^{M} \frac{\mu_p}{\alpha_p}(-N + \sum_{i=1}^{N} \varepsilon_i^{\alpha_p}). \tag{4.54}$$

where M, α_p and μ_i are material constants. For $M = 2, \alpha_1 = 2, \alpha_2 = -2$ the model reduces to the *Mooney-Rivlin solid*, and for $M = 1, \alpha_1 = 2$ it reduces to the *Neo-Hookean solid*. Example energies of the Ogden material model, the Mooney-Rivlin solid, and the Neo-Hookean solid are shown in Figure 4.10. Note, the Ogden material model assumes that the material is incompressible, and consequently is only valid when the constraint $\det(\boldsymbol{F}) = 1$ is fulfilled. This is the explanation for the negative energy areas found in Figure 4.10 – the energy functions are only valid along the green line. However, the Ogden material model can be extended to the compressible case by combining it with e.g. Eq. 4.52 or Eq. 4.53 and normalizing the principal stretches, i.e. $\hat{\varepsilon}_i = \varepsilon_i(\prod_{i=1}^{N} \varepsilon_i)^{-\frac{1}{N}}$.

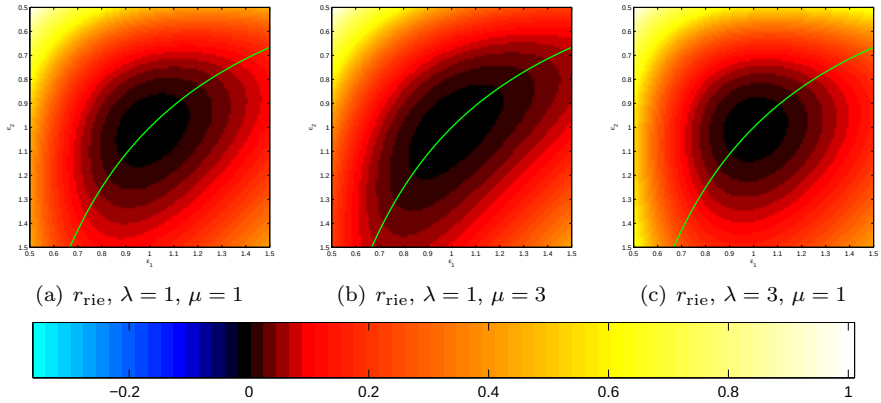

(a) r_{rie}, $\lambda = 1$, $\mu = 1$ (b) r_{rie}, $\lambda = 1$, $\mu = 3$ (c) r_{rie}, $\lambda = 3$, $\mu = 1$

(d) Colorbar.

Figure 4.8: The Riemannian density energy as a function of the principal stretches ε_1 and ε_2. The green line represents the no compression cases ($\det(\boldsymbol{F}) = \varepsilon_1\varepsilon_2 = 1$).

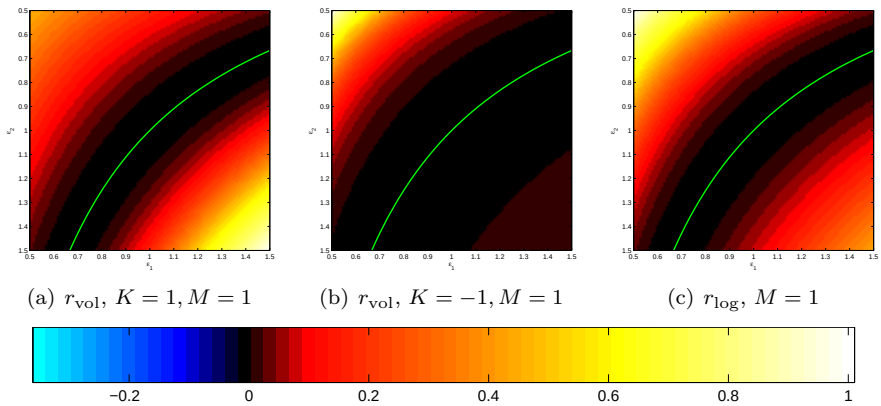

(a) r_{vol}, $K = 1, M = 1$ (b) r_{vol}, $K = -1, M = 1$ (c) $r_{\log}$, $M = 1$

(d) Colorbar.

Figure 4.9: Volumetric density energy as a function of the principal stretches ε_1 and ε_2. The green line represents the no compression cases ($\det(\boldsymbol{F}) = \varepsilon_1\varepsilon_2 = 1$).

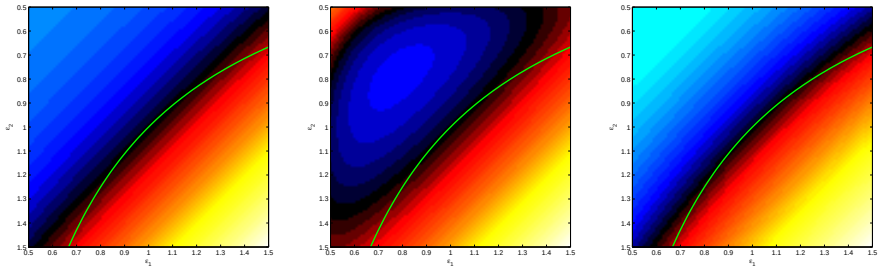

(a) r_{ogden}, $\alpha_1 = 2$, $\mu_1 = 4.225$ (Neo-Hookean rubber)

(b) r_{ogden}, $\alpha_1 = 2$, $\alpha_2 = -2$ $\mu_1 = 4.225$, $\mu_2 = -0.528$ (Mooney-Rivlin rubber)

(c) r_{ogden}, $\alpha_1 = 1.3$,, $\alpha_2 = 5$, $\alpha_3 = -2$, $\alpha 2 = -2$ $\mu_1 = 6.3$, $\mu_2 = 0.012$, $\mu_3 = 0.1$ (Ogden rubber)

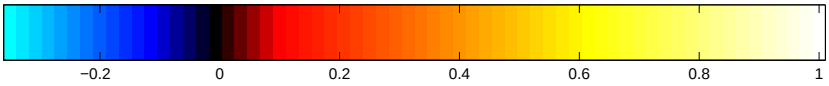

(d) Colorbar.

Figure 4.10: The Neo-Hookean, Mooney-Rivlin and Ogden density energies as a function of the principal stretches ε_1 and ε_2. The green line represents the no compression cases ($\det(\boldsymbol{F}) = \varepsilon_1\varepsilon_2 = 1$).

4.3.3.3 Examples of anisotropic elastic regularizers

Only limited research has been done on the use of anisotropic elastic regularizers for image registration. One advantage with the anisotropic elastic regularizers are that they can be used to incorporate statistical priors into the elastic regularization framework. Pennec et al. proposed the *statistical Riemannian elasticity energy*

$$r_{\text{srie}}(\boldsymbol{\phi}; \boldsymbol{x}) = \frac{1}{4} \int_{\Omega} \|\text{vect}((\boldsymbol{E}_0(\boldsymbol{x}) - \bar{\boldsymbol{E}}_0(\boldsymbol{x})))\|^2_{\boldsymbol{\Sigma}^{-1}(\boldsymbol{x})}, \tag{4.55}$$

where Σ is a covariance matrix and $\bar{\boldsymbol{E}}_0$ is a mean tensor calculated from a set of n previously observed deformations. Hence,

$$\bar{\boldsymbol{E}}_0(\boldsymbol{x}) = \frac{1}{n} \sum_{i=1}^{n} \boldsymbol{E}_{0,i}(\boldsymbol{x}) \tag{4.56}$$

and

$$\Sigma(\boldsymbol{x}) = \frac{1}{n} \sum_{i=1}^{N} \text{vect}(\boldsymbol{E}_{0,i}(\boldsymbol{x}))\text{vect}(\boldsymbol{E}_{0,i}(\boldsymbol{x}))^T. \tag{4.57}$$

Woods [177] proposed a similar statistical framework but he used the matrix $\log \boldsymbol{F}$ instead of the Hencky tensor. There are a number of theoretical problems

with using a non-symmetric tensor instead of a symmetric one. Primarily, $\log \boldsymbol{F}$ is not rotation invariant.

It is tempting to extend Eq. 4.55 by replacing the Hencky tensor with an arbitrary strain tensor. However, only a few strain tensor spaces lie on a linear manifold, and as such the usual matrix addition and substraction operations are not valid in general. That is, the matrix substraction of two strain tensors of the same type may not produce a strain tensor of that type.

4.4 Similarity measures

The similarity measure is the term in Eq. 4.1 which drives the registration. The derivatives of the similarity measure can be interpreted as a force field, which acts on the template image causing it to deform. In contradiction to the name most similarity measures do not measure the degree of similarity between images but rather the dissimilarity between them. Thus, most similarity measures quantify the degree of (dis)similarity by returning a non-negative real number – zero meaning that the images are *completely similar* or *identical*. This leads to the common misconception that a similarity measure is a distance function or metric. The truth is that many (dis)similarity measures fail to satisfy the *symmetry* and the *triangle inequality* conditions from the definition of a metric.

Under the assumption that two images are identical except for some spatial deformation the most instinctive approach for measuring the (dis)similarity between images is probably to compute the *squared difference*. The squared difference is in fact the optimal measure when the images are affected by independent additive Gaussian noise [170]. The applicability of the squared difference measure is unfortunately limited as the noise in medical images are often non-Gaussian. In addition to detector noise, medical images may also be corrupted with motion artifacts and reconstruction artifacts. In this section, it will be assumed that the images either contain an insignificant amount of noise, or that they have been noise corrected.

Another limitation of the squared difference measure is its incapability of measuring the similarity between multi-modality images, as they have different spectra. The most applied similarity measure for multi-modality registration is probably *normalized mutual information* [169, 174]. The choice of similarity should in general rely on the mapping type between the spectra of the two images. Table 4.1 lists, which mapping type, the included similarity measures are suitable for. The included similarity measures are *squared difference*, *correlation coefficient*, *correlation ratio*, *normalized mutual information* and *normalized gradient*

Mapping	Suitable measure(s)
Identity	Squared distance.
Linear	Correlation coefficient.
Monotone	Correlation ratio.
Otherwise	Mutual information and normalized gradient.

Table 4.1: The best choice of similarity measure depends on the mapping between the spectra of the two images to be registered.

fields. The registration framework implemented during the thesis work contains implementations of squared difference, correlation ratio and normalized gradient fields. The remaining measures have been included in the thesis for reasons of completeness.

4.4.1 Squared difference

The measure is given by

$$\mathcal{D}_{\text{sd}} = \frac{1}{2}\int_{\Omega}(R(\boldsymbol{x}) - T_{\phi}(\boldsymbol{x}))^2 d\boldsymbol{x}. \tag{4.58}$$

4.4.2 Correlation coefficient

The correlation coefficient is the optimal measure to use when there are a linear relationship between the intensities in the two images, e.g. registration of X-ray images. The measure is given by

$$\mathcal{D}_{\text{cc}} = \frac{\int_{\Omega}(R(\boldsymbol{x}) - \bar{R})(T_{\phi}(\boldsymbol{x}) - \bar{T}_{\phi})d\boldsymbol{x}}{\int_{\Omega}(R(\boldsymbol{x}) - \bar{R})^2 d\boldsymbol{x}\int_{\Omega}(T_{\phi}(\boldsymbol{x}) - \bar{T}_{\phi})^2 d\boldsymbol{x}}. \tag{4.59}$$

4.4.3 Correlation ratio

The correlation ratio was introduced as a similarity measure by Roche et al. [125], and it is given by

$$\mathcal{D}_{\text{cr}} = \frac{\int_{\Omega}(T_{\phi}(\boldsymbol{x}) - E[T_{\phi}(\boldsymbol{x})|R(\boldsymbol{x})])^2 d\boldsymbol{x}}{\int_{\Omega}(T_{\phi}(\boldsymbol{x}) - \bar{T}_{\phi})^2 d\boldsymbol{x}}, \tag{4.60}$$

where $E[T_{\phi}(\boldsymbol{x})|R(\boldsymbol{x})]$ is the expected value of $T_{\phi}(\boldsymbol{x})$ given $R(\boldsymbol{x})$. This measure can handle non-linear monotone mappings between spectra which makes it

suitable for intra-modal registration of MR images, where the mapping is not necessarily linear. The measure is not suitable for multi-modality image registration as it is unable to handle one-to-many mappings from the spectra of the reference image. This drawback is inherited from the use of $E[\cdot|\cdot]$. Note, this dissimilarity measure is comparable to the *partioned intensity uniformity* measure proposed by Woods et. al. [178].

4.4.4 Normalized mutual information

Normalized mutual information is the normalized version of the mutual information similarity measure which was introduced by Viola and Wells [169, 174]. Studholme et al. [154] showed that misregistration may cause an increase in mutual information and proposed the normalized mutual information as a better alternative. The normalized mutual information between two images is given by

$$\mathcal{D}_{\text{mi}} = \frac{H(R) + H(T_\phi)}{H(R, T_\phi)}, \tag{4.61}$$

where $H(I)$ is the entropy of the image I, and $H(R, T_\phi)$ is the joint entropy between the reference and deformed template image.

4.4.5 Normalized gradient fields

Haber et al. [73] introduced normalized gradient fields as an alternative to mutual information. They were motivated by the observation that mutual information is highly non-convex and has a tendency to fall into local minima during optimization. The basic idea behind the measure is that two images are similar, if the changes in intensities occur at the same locations. The normalized gradient field similarity measure is given by

$$\mathcal{D}_{\text{ng}} = -\frac{1}{2} \int_{\boldsymbol{x}\in\Omega} < \boldsymbol{n}_\epsilon(R, \boldsymbol{x}), \boldsymbol{n}_\epsilon(T_\phi, \boldsymbol{x}) >^2, \tag{4.62}$$

where

$$\boldsymbol{n}_\epsilon(I, \boldsymbol{x}) = \frac{\nabla I(\boldsymbol{x})}{\sqrt{\nabla I(\boldsymbol{x})^T \nabla I(\boldsymbol{x}) + \epsilon^2}}.$$

ϵ is the *jump*-parameter, which ensures that the measure is differentiable, even if one of the image gradients is zero, and it decreases the sensitivity to image noise.

Chapter 5

Discretization

While Chapter 4 dealt with the theoretical aspects of image registration this chapter deals with the image registration on a practical level. That is, to solve the definite IRP of Eq. 4.1 it has to be transformed into a finite problem which is solvable on a computer. The most common approach for discretization of the IRP with a regularization term formulated upon the transformation derivatives is to differentiate Eq. 4.1 to obtain the *Euler-Lagrange* equations. The equations are subsequently discretized and solved numerically [15, 21, 32]. In this thesis, the discretize-optimize approach [71–73] is pursued, which means that Eq. 4.1 is discretized and then differentiated. The advantages with the this approach is, that it can be efficiently optimized with a gradient based optimizer, and it has no problem with handling non-linearity in the derivatives of the regularization term.

5.1 Discretization of D

To compute the (dis)similarity between two images, we need to replace the integral of the (dis)similarity measure with a finite sum. Numerical integration is the approximate computation of the integral

$$\int_{\Omega} f(\boldsymbol{x}) d\boldsymbol{x}. \tag{5.1}$$

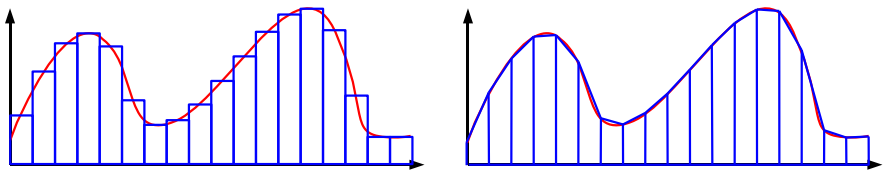

(a) Midpoint quadrature rule (b) Trapezoidal quadrature rule

Figure 5.1: Quadrature rules for numerical integration

The simplest and the most common approach for numerical integration is the *midpoint quadrature rule* (MQR), where the function f is locally approximated with a constant function (polynomial of zero order). The MQR is illustrated in Figure 5.1 (a). In order to apply the midpoint quadrature rule, the continuous image domain Ω needs to discretized into a finite set of discrete sub-domains. In practice, this means that the image domain is tesselated into a mesh representation consisting of convex polytopes. The MQR is

$$\int_{\Omega} f(\boldsymbol{x}) d\boldsymbol{x} \approx \sum_{i=1}^{n} V_i f\left(\frac{1}{L(\mathcal{T}_i)} \sum_{j \in \mathcal{T}_i} \boldsymbol{v}_j\right), \tag{5.2}$$

where V_i is the volume of the ith element, $\boldsymbol{v}_j$ is the jth vertex in the mesh, $\mathcal{T}_i$ is the set of vertex indices of the ith polytope, and $L(\mathcal{T}_i)$ is the length of $\mathcal{T}_i$.

As most discrete images are discretized on a regular grid $\mathcal{U}_n = (\boldsymbol{x}_0, \boldsymbol{\Delta}, \boldsymbol{s})$ it is customary to use this tessellation for the discretization of D. The MQR for a rectangular lattice $\mathcal{U}_n$ is

$$\int_{\Omega} f(\boldsymbol{x}) d\boldsymbol{x} \approx V \sum_{\boldsymbol{x}_i \in \mathcal{U}_c} f(\boldsymbol{x}_i), \tag{5.3}$$

where $\mathcal{U}_c = (\boldsymbol{x}_0 + \frac{1}{2}\boldsymbol{\Delta}, \boldsymbol{\Delta}, \boldsymbol{s} - 1)$ is the cell-centered lattice of $\mathcal{U}_n$ and $V = \prod_{i=1}^{N} \Delta_i$.

While it is not the standard in image registration one can alternatively approximate f locally with a higher order polynomial. Figure 5.1 (b) exemplifies the *Trapezoidal quadrature rule*(TQR), where f is locally approximated linearly (polynomial of first order).

5.2 Discretization of $\mathcal{S}$ and ϕ

Discretization of the regularization term $\mathcal{S}$ is straight forward when dealing with a parametric representation of the transformation. In these cases, it is possible to compute the spatial derivatives of the transformation directly, and $\mathcal{S}$ can be approximated with numerical integration techniques as above. In practice, this type of discretization becomes unstable when the number of transformation parameters approaches the number of discretization samples.

For a more stable discretization we turn our attention to *Finite Element Discretization* (FED). FED is the applied discretization in the *Finite Element Method* (FEM), which is a popular technique for solving partial differential equations and integral equations. The FEM has, since the pioneering work of Courant [38], been the topic of many engineering textbooks [55, 179] and applied in many image registration and virtual surgery applications [18, 21, 22, 54, 89, 139]. The basic idea behind FED is to discretize the domain into a *finite* number of discrete sub-domains (similar to numerical integration) where f can be approximated with a linear function. In the FEM terminology the discrete sub-domains are called *elements* which give reason to the name *Finite Element Method*. In some sense, the FED is related to the TQR of numerical integration, which is illustrated in Figure 5.1 (b). That is, the only difference between FED and TQR is that the FED approximates the function f itself, while TQR approximates the integral of f. In FED it is custom to discretize the domain using simplices (lines, triangles, tetrahedrons, etc.). A simplex of a ND space consists of exactly $N+1$ points/vertices, which is the minimum number of points required to model N linearly independent vectors. Thus, the name refers to the fact that it is the simplest polytope in any given space. The reason, that the simplex topology is the preferred mesh topology, is that the local linear approximation function of f can be represented by the linear interpolation of the function values of f in the vertices of the simplex. There exists a number of non-linear extensions to the standard FEM, e.g. hp-FEM [10, 70, 83] and the spectral-FEM[83, 121].

Let $\boldsymbol{x}$ be an arbitrary point and let the vertices $\{\boldsymbol{v}_1, \dots \boldsymbol{v}_{N+1}\}$ define a simplex in a ND space. Now, $\boldsymbol{x}$ can be written as a linear combination of the vertices

$$\boldsymbol{x} = \begin{bmatrix} \boldsymbol{v}_1 & \cdots & \boldsymbol{v}_{N+1} \end{bmatrix} \boldsymbol{\eta} = \boldsymbol{V}\boldsymbol{\eta}. \tag{5.4}$$

$\boldsymbol{\eta}$ is called the barycentric coordinates of $\boldsymbol{x}$ w.r.t. $\boldsymbol{v}_1, \cdots \boldsymbol{v}_{N+1}$. As $\boldsymbol{V}$ is $N \times (N+1)$ matrix $\boldsymbol{\eta}$ is not uniquely defined for a given $\boldsymbol{x}$. By adding the

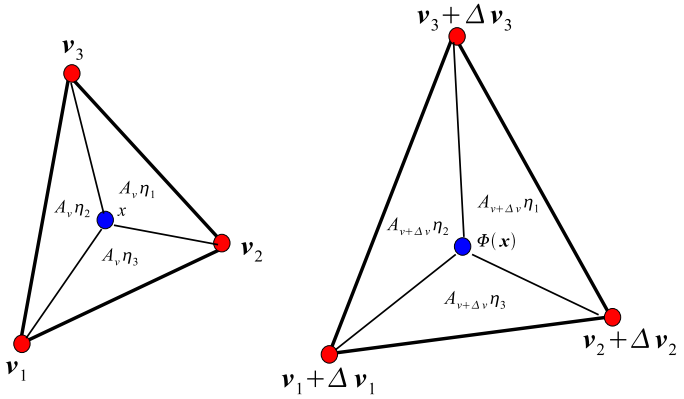

Figure 5.2: Illustration of the linear/affine transformation $\boldsymbol{\Phi}(\boldsymbol{x})$ from triangle $\{\boldsymbol{v}_1, \boldsymbol{v}_2, \boldsymbol{v}_3\}$ to triangle $\{\boldsymbol{v}_1 + \Delta\boldsymbol{v}_1, \ldots \boldsymbol{v}_{N+1} + \Delta\boldsymbol{v}_{N+1}\}$ with $x \in \{\boldsymbol{v}_1, \boldsymbol{v}_2, \boldsymbol{v}_3\}$ corresponds to the point $\boldsymbol{\phi}(\boldsymbol{x})$ in $\{\boldsymbol{v}_1 + \Delta\boldsymbol{v}_1, \boldsymbol{v}_2 + \Delta\boldsymbol{v}_2, \boldsymbol{v}_{N+1} + \Delta\boldsymbol{v}_{N+1}\}$.

homogenous constraint $\sum_{i=1}^{N+1} \eta_i = 1$, we get

$$\begin{bmatrix}\boldsymbol{x}\\1\end{bmatrix} = \begin{bmatrix}\boldsymbol{v}_1 & \cdots & \boldsymbol{v}_{N+1}\\1 & \cdots & 1\end{bmatrix}\begin{bmatrix}\eta_1\\\vdots\\\eta_{N+1}\end{bmatrix} = \begin{bmatrix}\boldsymbol{V}\\\boldsymbol{1}^T\end{bmatrix}\boldsymbol{\eta}, \tag{5.5}$$

$$\boldsymbol{\eta} = \begin{bmatrix}\boldsymbol{V}\\\boldsymbol{1}^T\end{bmatrix}^{-1}\begin{bmatrix}\boldsymbol{x}\\1\end{bmatrix} = \begin{bmatrix}\boldsymbol{D} & \boldsymbol{\eta}^0\end{bmatrix}\begin{bmatrix}\boldsymbol{x}\\1\end{bmatrix}. \tag{5.6}$$

A point $\boldsymbol{x}$ is inside or on the edge of the simplex $\{\boldsymbol{v}_1, \ldots \boldsymbol{v}_{N+1}\}$ if $0 \leq \eta_i \leq 1$ for all i. Geometrically speaking, the first barycentric coordinate of a point $\boldsymbol{x}$ inside a triangle $\{\boldsymbol{v}_1, \boldsymbol{v}_2, \boldsymbol{v}_3\}$ is the area of the triangle $\{\boldsymbol{x}, \boldsymbol{v}_2, \boldsymbol{v}_3\}$ normalized with the area of the triangle $\{\boldsymbol{v}_1, \boldsymbol{v}_2, \boldsymbol{v}_3\}$. This is illustrated in the left triangle of Figure 5.2.

The linear or affine transformation between a simplex $\{\boldsymbol{v}_1, \ldots \boldsymbol{v}_{N+1}\}$ and a simplex $\{\boldsymbol{v}_1 + \Delta\boldsymbol{v}_1, \ldots, \boldsymbol{v}_{N+1} + \Delta\boldsymbol{v}_{N+1}\}$ can be defined by assuming that the point $\boldsymbol{x}$ inside $\{\boldsymbol{v}_1, \ldots \boldsymbol{v}_{N+1}\}$ corresponds to the point $\boldsymbol{\phi}(\boldsymbol{x})$ in $\{\boldsymbol{v}_1 + \Delta\boldsymbol{v}_1, \ldots, \boldsymbol{v}_{N+1} + \Delta\boldsymbol{v}_{N+1}\}$ which has the same barycentric coordinates. Hence,

$$\boldsymbol{\phi}(\boldsymbol{x}) = \boldsymbol{x} + \Delta\boldsymbol{V}\boldsymbol{\eta} = \boldsymbol{x} + \Delta\boldsymbol{V}\begin{bmatrix}\boldsymbol{D} & \boldsymbol{\eta}^0\end{bmatrix}\begin{bmatrix}\boldsymbol{x}\\1\end{bmatrix}, \nabla\Phi(\boldsymbol{x}) = \boldsymbol{I} + \Delta\boldsymbol{V}\boldsymbol{D}. \tag{5.7}$$

During this thesis work, domain discretization has been limited to two types of mesh topologies. The regular grid topology was applied in the case of parametric transformations, and tetrahedral mesh topology was applied in the FED

case. The included paper *Generating Quality Tetrahedral Meshes From Binary Volumes* (Chapter 12) describes an approach for tessellating binary shapes using tetrahedral meshes.

5.3 Parametric vs non-parametric registration

In the image registration community there is a tendency to put emphasis on the difference between parametric and non-parametric image registration. To stress this point it took the author a couple of minutes to find six image registration papers [41, 86, 92, 113, 149, 165] with six different first authors, which all had *parametric* or *non-parametric* in the title. This section will try to demonstrate that the distinction between parametric and non-parametric registration is mostly a matter of interpretation.

Let $\boldsymbol{X}$ be a $N \times n$ matrix containing n discretization or sample points. Independent of the choice of discretization and type of transformation representation, the discrete transformation can be written in the form

$$\boldsymbol{X} + \boldsymbol{W}\boldsymbol{Q}, \tag{5.8}$$

where $\boldsymbol{W}$ is a $N \times m$ matrix with the transformation parameters and $\boldsymbol{Q}$ is a projection matrix. Likewise, the derivatives in the ith direction can be represented on the matrix form

$$\boldsymbol{I}_i \otimes \mathbf{1} + \boldsymbol{W}\boldsymbol{Q}_i, \tag{5.9}$$

where $\boldsymbol{I}_i$ is the $i$the column of the identity matrix, $\mathbf{1}$ is a row vector of ones with n elements, and $\boldsymbol{Q}_i$ is the projection matrix, which gives or approximates the spatial displacement derivatives in the ith direction. In a finite difference scheme $\boldsymbol{Q}$ is simply the identity matrix, and each column of $\boldsymbol{Q}_i$ will contain a finite difference operator. In a finite element scheme each column of $\boldsymbol{Q}$ will contain an average operator, and each column of $\boldsymbol{Q}_i$ will contain a vectorized version of $\boldsymbol{D}$ from Eq. 5.6. In a parametric scheme each column of $\boldsymbol{Q}$ will contain the basis functions of the parameterization, and each column of $\boldsymbol{Q}_i$ will contain the spatially differentiated basis functions.

The discretized version of Eq. 4.1 with a diffusive regularizer can be written on the form

$$\widehat{\mathcal{D}}[R(\boldsymbol{X}), T(\boldsymbol{X} + \boldsymbol{W}\boldsymbol{Q})] + \alpha \sum_{j=1}^{N} \boldsymbol{w}_j \left(\sum_{i=1}^{N} \boldsymbol{Q}_i \boldsymbol{Q}_i^T \right) \boldsymbol{w}_j^T \tag{5.10}$$

and the derivatives w.r.t. $\boldsymbol{W}$ are

$$\nabla_{\tilde{\boldsymbol{x}}} \widehat{\mathcal{D}}[R(\boldsymbol{X}), T(\boldsymbol{X} + \boldsymbol{W}\boldsymbol{Q})]\boldsymbol{Q}^T + \alpha \boldsymbol{W} \sum_{i=1}^{N} \boldsymbol{Q}_i \boldsymbol{Q}_i^T, \tag{5.11}$$

where $\widehat{\mathcal{D}}[R(\boldsymbol{X}), T(\boldsymbol{X} + \boldsymbol{W}\boldsymbol{Q})]$ is the discretized similarity measure, and $\boldsymbol{w}_j$ is the jth row of $\boldsymbol{W}$. The spatial derivatives of the similarity measure $\nabla_{\tilde{\boldsymbol{x}}}\widehat{\mathcal{D}}[R(\boldsymbol{X}), T(\boldsymbol{X} + \boldsymbol{W}\boldsymbol{Q})]$ are in most image registration literature (e.g. in [108]) called the forces or the force field. By multiplying the force field with $\boldsymbol{Q}^T$ ($n > m$) the force field is projected into a lower dimensional subspace. For most choices of $\boldsymbol{Q}$ this will have a smoothing effect on the force field. The Thirion's demons based image registration approach[163] and the viscous fluid model in [43] apply Gaussian convolution upon the force field to ensure a topology preserving deformation. The same smoothing effect could be achieved by parameterizing the displacement field with Gaussian radial basis functions (GRBFs) where the knots of the basis functions coincide with the sample points. The difference being that the weights of the GRBFs would be the actual displacements in [43, 163].

Here is an example where the distinction between parametric and non-parametric registration disappears. Consider modeling a displacement field with the cubic interpolation kernel (cf. Eq. 4.7) with $\alpha = -1$ on a rectangular lattice. With this model the transformation derivatives at the knot position are identical to the central difference approximation, and the displacement at a knot position corresponds to the weight of the kernel at the knot.

The FED can be interpreted as being a true parametric representation of the transformation, which has been discretized in the center of the simplices instead of being a finite element approximation to the transformation. There is one theoretical problem with this interpretation, which is that the transformation is non-differential along the borders of the simplices. The non-differentiability of the transformation makes Eq. 4.1 non-differentiable. However, this problem is circumvented by not sampling the transformation along the borders of the simplices.

The point to be made is that non-parametric image registration to a large extend is the gray zone of parametric registration, where the number of discretization samples is *close* to number of transformation parameters. The important elements for a stable discretization are $\boldsymbol{Q}$ and $\boldsymbol{Q}_i$. To support this statement we end the section with a small example.

Let us represent a 1D freeform deformation by storing the individual displacements of a set of n equivalently spaced points and approximate the derivatives using the first-order central difference operator. The derivatives of the first point and last point in the sequence are approximated with the first-order forward and backward finite difference operators, respectively. Now $\boldsymbol{Q_1}$ is a $n \times n$ matrix with rank $n-1$ which implies that $\boldsymbol{Q}_1^T\boldsymbol{Q}_1$ is an $n \times n$ semi-definite matrix with rank $n-1$. Figure 5.3(a) shows a plot of the normalized eigenvalues of $\boldsymbol{Q}_1^T\boldsymbol{Q}_1$ for $n = 40$. Figure 5.3(b) contains a plot of the elements in the eigenvector

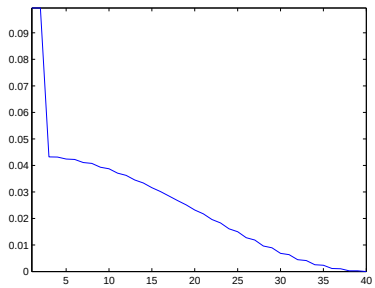

(a) Normalized eigenvalue plot.

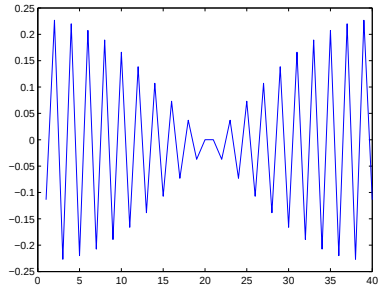

(b) Eigenvector with second smallest eigenvalue.

Figure 5.3: The eigenvalues and eigenvectors of $\boldsymbol{Q}_1^T \boldsymbol{Q}_1$ for $n = 40$.

with the second smallest non-zero eigenvalue. From the plots in Figure 5.3 we conclude that oscillating displacement patterns, as shown in Figure 5.3(b), will almost not get penalized by the regularizer as the second smallest eigenvalue is almost zero relatively speaking. Furthermore, as $\boldsymbol{Q}$ in this case is the identity matrix it has no smoothing effect on the force field. All-in-all this is not a stable discretization and therefore not suited for a discretize-optimize approach.

Part II

Contributions

Chapter 6

Summery of contribution

The six following chapters present the main contributions of the thesis. Each chapter contains a self-contained paper which can be read independently.

The central point of research in the papers is the study of morphology using image registration. The first two papers are application papers which use shape information to do virtual cutting. The included applications are build upon image registrations made by the RegLab image registration framework, which is the primary practical contribution of this thesis. A small description of the use and the functionality is given later in this chapter.

The following three chapters are image registration papers of a more theoretical nature. The first image registration paper presents a shape alignment algorithm, which aligns shapes by performing rigid image registration on the signed distance map representations of the shapes. The next image registration paper deals with the construction of diffeomorphic deformation models. The final image registration paper presents an approach to construct conditional statistical priors on compositional deformation models. The papers are included as submitted and may therefore apply a different notation than the rest of the thesis.

The final paper introduces a tessellation approach which generates quality tetrahedral meshes from binary volumes. This tessellation provides the basis for the

finite element discretization which is used by the RegLab image registration framework.

6.1 RegLab

RegLab is a collection Matlab classes which put together provide the necessary tools to do image registration. The easiest way to access the functionality of the framework is through the class `RegistrationController`. The matlab code snippet below rigidly registers the images `1.gipl.gz` through `n.gipl.gz` to the reference image `'atlas.gipl.gz'`.

```
1  initialize;
2  dataDir = ´/.../mydatadir/´;
3  outDir  = ´/.../myoutputdir/´;
4  referenceDir = ´/.../myreferencedir/´;
5
6  contr = RegistrationController(dataDir, outDir, referenceDir);
7  %TYPE = Linear, SUBTYPE = Rigid
8  opt = getDefaultSettings(contr, ´Linear´, ´Rigid´);
9
10 opt.masker = @standardMask;
11 opt.targets = {´1.gipl.gz´, ´2.gipl.gz´, .. , ´n.gipl.gz´}
12 opt.atlas   = ´atlas.gipl.gz´;
13 opt.mask    = ´mask.gipl.gz´;
14 register(contr, opt);
```

The member function `RegistrationController.getDefaultSettings` with arguments 'Linear' and 'Rigid' gets the default settings for doing rigid registration. If you want to do cubic B-spline registration instead you simply change the arguments of `getDefaultSettings` to 'NRP' and 'Cubic'. To do Riemannian elasticity registration with a tetrahedral mesh topology you change the arguments to 'NRNP' and 'Riemannian'. Line 10 specifies that you only want to register the part of the reference image which is specified by the mask image given by option `opt.mask`. As default no mask is applied, and the registration is done on the entire domain of the reference image. For all possible settings simply open the `getDefaultSettings.m` file with the Matlab editor.

6.1.1 Functionality

This section contains a brief description of the functionality of the RegLab.

6.1.1.1 Geometrical transformations

The Reglab framework offers a number of possible geometric transformations:

- Global linear.
  - Rigid.
  - Similarity.
  - Affine.
- Regular grid topology.
  - Linear interpolation.
  - Cosine interpolation.
  - Quadratic and cubic B-spline.
- Tetrahedral mesh topology.
  - Linear interpolation.

6.1.1.2 Similarity measures

The framework currently implements three different similarity measures, which are

- squared difference,
- correlation ratio,
- and normalized gradient.

6.1.1.3 Regularization

The framework currently contains implementations for six regularizers or soft contraints. The regularizers can be combined if necessary by the `CombinedRegularizer` class. The regularizers are

- general quadratic regularization (this regularizer can be used to model linear elasticity and diffusion),

- St. Vernant elasticity regularization,
- Riemannian elasticity regularization,
- Ogden material model (standard),
- volumetric regularization (cf. Eq. 4.53 and Eq. 4.52).
- and soft surface and point constraints.

The Ogden material model and the volumetric regularizers are implemented for the tetrahedral mesh topology only.

6.1.1.4 Interpolation

The framework currently contains implementations of four interpolators. All interpolators are wrapped in the Matlab class `ImageFunction` which also incorporates Gaussian scale-space. The types of interpolation are

- linear interpolation kernel,
- cosine interpolation kernel,
- cubic interpolation kernel,
- and cubic B-spline.

Chapter 7

Virtual cutting atlas

Mads Fogtmann Hansen, Lars Bager Christensen and Rasmus Larsen

Abstract

This paper presents the concept and the construction of a virtual cutting atlas. A virtual cutting atlas is a framework for performing virtual cutting on a database of images of pigs. Anatomical labeling from a reference image can be transferred to the images of the database by establishing correspondence between the images of the database and the reference image. The gained anatomical knowledge can subsequently be used to guide and secure a consisting virtual cutting of the images. From a database of 300 CT scans of the pork middle a single scan is selected to be the reference image, and a number of masks are traced on the reference. The remaining 299 scans are registered to the reference image with a finite element based image registration approach using the squared difference dissimilarity measure to drive the registration and the Riemannian elasticity energy to regularize the deformation. It is assumed that information needed to guide and define virtual cuts fall into three categories; anatomical, semi-anatomical and geometrical. The types of information are embedded in masks and combined with the usual set operations to define cuts and products. Two examples of virtual product ranges are presented in the paper.

7.1 Introduction

Since the first shipment of Danish bacon arrived in England in 1847 the Danish pig producing industry (DPPI) has grown to become one of the most important

industries in Denmark with an annual production of nearly 26 million pigs and an export totalling approximately 27 billion DDK in 2007[5]. Increased competition from countries such as the U.S. and Brazil, which have considerably lower wages and restrictions on food safety, threatens the continuing success of DPPI. To maintain a competitive edge DPPI continues to focus on the optimization of the pig production and slaughtering process.

Over the last decade DPPI has implemented a number of changes to increase the efficiency of the modern abattoirs. Especially, more and more slaughter and cutting robots are introduced to decrease the reliance on expensive manual labor. Because of the success of this automation, the largest potential increase in earnings lies in an optimized use of the raw materials. Pig carcasses are a natural material and thus exhibit a natural anatomical variation. The shape and the distribution of meat and fat in a given pig have a large impact on which product range is the optimal choice w.r.t. the yield of the individual pig. To get a deeper understanding of the optimal use it is important to link the anatomical variation of pigs to the vast combination of possible cuts and the potential yields of the combinations.

To gain this knowledge we build a *virtual cutting atlas* (VCA). A VCA is a framework which provides the ability to imitate the real cuts from the abattoirs automatically and consistently on a database of virtual representations (images) of pig carcasses. As the majority of cuts in an abattoir are based on the anatomy of the pig, the key to achieving consistent cutting in the virtual setting lies in the consistent identification of the anatomical structures in the images of pigs. In medical imaging and neuroscience, *deformable atlases* are often used for automated labeling and segmentation. The basic idea behind a deformable atlas is to propagate the manual labeling of a reference image to a set of target images by establishing correspondence between the reference and the targets using automated image registration.

We define a standard set of cutting tools upon the anatomical labeling, which allows us to combine different cuts and to propagate them to the database of pigs. The virtual cutting atlas presents the opportunity to test and experiment with the different product ranges upon a representative database of pigs.

7.1.1 Related work

Brain atlases have been used for decades in medical imaging to study and analyze the variation of structures across age, gender, diseases, etc [15, 19, 34, 44, 49, 82, 104, 127, 130, 164, 177]. An atlas is a map of some anatomy built from a set of annotations of a reference representation of the anatomy. Image

registration techniques can map new observations to the atlas by geometrically deforming the reference to match the new observations. Deformable atlases, which can adapt to the anatomy of a new subject, allow for an automatic labeling of incoming subjects and subsequent analysis of structural differences. In tensor based morphometry the relative displacement (often represented by the determinant of the Jacobian of the deformation tensor) is used to relate structural difference to clinical variables.

The idea of a cutting atlas was originally presented by Vester-Christensen [168]. Vester-Christensen constructed a cutting atlas from 57 CT scans of half pig carcasses. A single scan was selected to be the reference, and 50 3D landmarks were placed into the reference. The remaining 56 scans were subsequently spatially normalized using a tensor B-spline image registration technique. The atlas was used to perform a trisection on the half pig carcasses into the fore-end, pork middle and the ham part (see Figure 7.1), and to cut a single pork middle product combination. The cuts were modeled by planes which were defined upon the landmarks. The current work differentiates itself from the work of Vester-Christensen on a number of points:

- Our atlas only contains the pork middle. All pigs are trisected in the abattoirs, and thus there is no advantage in building an atlas on the entire half pig carcass. That is, it is better to build three individual atlases.
- We apply a rotation invariant elasticity energy to regularize the deformation field under the image registration process, while Vester-Christensen used a diffusion regularizer which is not rotation invariant. Hence, our image registration should be able to uncover much larger deformations.
- We define cuts with masks which are more flexible than planes.

7.1.2 Data

The used data set consists of 300 CT scans of the pork middle. Figure 7.1 shows the tomogram of a half pig carcass with vertical lines marking the beginning and the end of the pork middle. Voxel dimensions are $[0.87 \times 0.87 \times 10]\text{mm}^3$ with a 10mm spacing between consecutive slices. The pigs are of mixed breed and representative of the Danish pig population w.r.t. weight and fatness. The low out-plane resolution may cause topological difference problems between the atlas and some of the targets scans. That is, many of the structures are thin and run parallel with the slice planes which makes them vulnerable to the partial voluming caused by the low out-plane resolution. In practice, this means that the ribs are geometrically distorted (appear twice as thick as they really are),

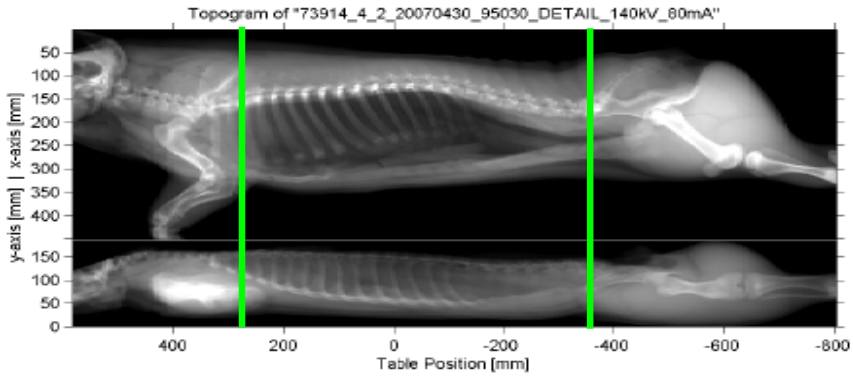

Figure 7.1: The topogram of a full body scan of a half pig carcass. The two green lines approximately mark the trisection of the pig carcass into the fore-end, pork middle and the ham part.

and some of the thin muscles vanish or fade out. This is naturally suboptimal for intensity based image registration.

7.2 Deformable atlas

For the construction of the atlas, a single scan was chosen to be the reference image of the atlas. In most situations it is an advantage to select a reference which resembles the *mean* of the population. Our selection was complicated by the existence of rapid surface oscillations on the skin side of the pork middles. The problem with skin folding and bending is illustrated in Figure 7.2. Non-anatomical skin folding and bending develop while the pig carcasses are hanging on cambrels in the cooling facility before cutting. The problem exists in all the scanned pigs but with different severity. It is likely to assume that the inter-subject registration of two individuals will fail to produce satisfactory correspondences, if both individuals contain many oscillations. The selected reference pig is only mildly affected by folding and bending but it is a little bit on the slim side and larger than average. The bias inherited from selection of the reference can be removed by updating the reference with the mean deformation between the reference pig and the remaining pigs of the database.

Anatomical knowledge has been added to the atlas by tracing a number of anatomical structures upon the reference image. The structures are visualized in Figure 7.3.

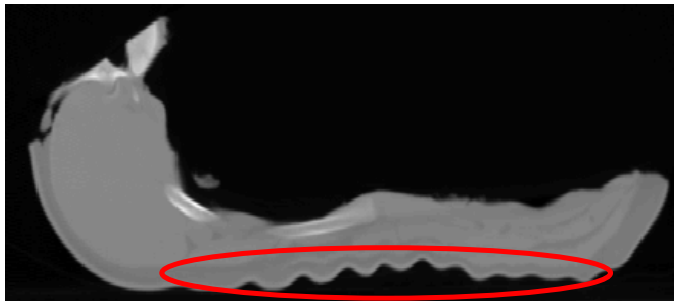

Figure 7.2: A slice of pig 290. The red ellipse marks a surface area with many folds and bends.

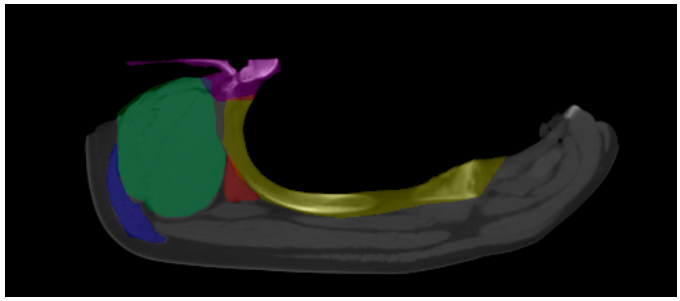

(a) Loin (green), ribs (yellow), dark muscle (red), spine (purple), false lean (blue).

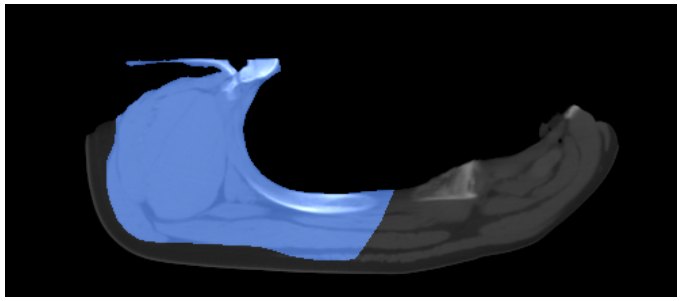

(b) Lower fat (cyan)

Figure 7.3: Anatomical masks superimposed on slice from reference image.

To transfer the anatomical labeling to the pigs of the database the pigs have to be spatially normalized against the reference pig. For this purpose we apply intensity based image registration.

7.2.1 Spatial normalization

Anatomical structures vary across the population in size and shape. The purpose of image registration is to establish correspondence between two images by spatially deforming one image such that the structures in two images match spatially. This is by done minimizing the dissimilarity between the images subject to a regularized deformation. In CT-to-CT registration it is custom to use the squared difference dissimilarity measure to quantify the degree of similarity between images

$$\mathcal{D}_{\mathrm{sd}}[R, T, \boldsymbol{\phi}] = \frac{1}{2} \int_{\Omega} (R(\boldsymbol{x}) - T_{\phi}(\boldsymbol{x}))^2 d\boldsymbol{x}, \tag{7.1}$$

where $T_{\phi} = T \circ \boldsymbol{\phi}$ is the deformed template image w.r.t. the transformation $\boldsymbol{\phi}$, R is the reference image and Ω is the domain of R.

There exists a range of spatial deformation models for modeling the mapping between biological structures of the same class. Many of these originate from the world of continuum mechanics, e.g. elasticity [24] and viscous elasticity [32]. That is, the transformation between a reference image and a template image is assumed to be equivalent to that of an elastic material or fluid undergoing deformation due to external forces. We apply the *Riemannian elasticity* [122] to regularize the deformation

$$\mathcal{S}[\boldsymbol{\phi}] = \int_{\Omega} \mu \mathrm{tr}(\boldsymbol{E}_0(\boldsymbol{x})^2) + \frac{\lambda}{2} \mathrm{tr}(\boldsymbol{E}_0(\boldsymbol{x}))^2 d\boldsymbol{x}, \tag{7.2}$$

where μ and λ are the Láme constants, and $\boldsymbol{E}_0$ is the *Hencky* strain tensor

$$\boldsymbol{E}_0(\boldsymbol{x}) = \frac{1}{2} \log(\nabla \boldsymbol{\phi}(\boldsymbol{x})^T \nabla \boldsymbol{\phi}(\boldsymbol{x})). \tag{7.3}$$

Riemannian elasticity has a number of nice properties compared to widely used *linear elasticity* [24]. Primarily, the Riemannian elastic energy is rotation-invariant which enables it to handle large deformations. The linear elastic energy is *not* rotation-invariant as it inherits a small deformation assumption from its use of the *Cauchy-Green* deformation tensor. Secondly, it takes an infinite amount of energy in Riemannian elasticity to do the black hole deformation (collapse) which protects the deformation against folding.

The template image T is registered to the reference image R by minimizing the cost function

$$\mathcal{D}_{\mathrm{sd}}[R, T, \boldsymbol{\phi}] + \alpha \mathcal{S}[\boldsymbol{\phi}], \tag{7.4}$$

where α is constant weighting the influence of the regularization.

To minimize Eq. 7.4 w.r.t. the transformation $\boldsymbol{\phi}(\boldsymbol{x})$, we discretize the transformation using finite elements, i.e. tessellating the non-background in the reference image with a tetrahedral mesh. Our tessellation method is described in details in [76]. An example of the tessellation of the reference pigs is shown in Figure 7.4. At each vertex of the mesh, we store a vector describing the spatial displacement of the vertex. The transformation $\boldsymbol{\phi}(\boldsymbol{x})$ of a point $\boldsymbol{x}$ inside the tetrahedron defined by the vertices $\boldsymbol{V}$ is approximated linearly, i.e.

$$\boldsymbol{\phi}(\boldsymbol{x}) \approx \hat{\boldsymbol{\phi}}_{\boldsymbol{V}}(\boldsymbol{x}; \Delta\boldsymbol{V}) = \boldsymbol{x} + \Delta\boldsymbol{V} \begin{bmatrix} \boldsymbol{V} \\ \mathbf{1} \end{bmatrix}^{-1} \boldsymbol{x} = \boldsymbol{x} + \Delta\boldsymbol{V}\boldsymbol{D}\boldsymbol{x}, \tag{7.5}$$

where $\Delta\boldsymbol{V}$ is the displacement of the vertices $\boldsymbol{V}$. Thus, the spatial gradient of discretized transformation is

$$\nabla\hat{\boldsymbol{\phi}}_{\boldsymbol{V}}(\boldsymbol{x}; \Delta\boldsymbol{V}) = \mathbf{I} + \Delta\boldsymbol{V}\boldsymbol{D}. \tag{7.6}$$

The similarity measure is discretized with the usual midpoint quadrature rule with the same tessellation as used to discretize the transformation. The discretized version of Eq. 7.4 is minimized using the conjugated gradient optimization method.

In theory, Riemannian elasticity should protect the deformation against folding but it does not in practice. The Riemannian elasticity energy from Eq. 7.2 will only evaluate to infinity in case of a collapse and not in the case of folding. A given optimization method may take a *long* step (over a peak of infinite energy), which makes the deformation fold, without successful intervention from the regularization. To protect the deformation against folding we modify the Riemannian elasticity energy to return infinity in the a case of a folding and implement a folding check. For all tetrahedra, we order the vertices $\{\boldsymbol{v}_1, \ldots, \boldsymbol{v}_4\}$ such that

$$\det\left(\begin{bmatrix} \boldsymbol{v}_1 & \boldsymbol{v}_2 & \boldsymbol{v}_3 & \boldsymbol{v}_4 \\ 1 & 1 & 1 & 1 \end{bmatrix}\right) \tag{7.7}$$

is positive. A deformation is non-folding as long as

$$\det\left(\begin{bmatrix} \boldsymbol{v}_1 + \Delta\boldsymbol{v}_1 & \boldsymbol{v}_2 + \Delta\boldsymbol{v}_2 & \boldsymbol{v}_3 + \Delta\boldsymbol{v}_3 & \boldsymbol{v}_4 + \Delta\boldsymbol{v}_4 \\ 1 & 1 & 1 & 1 \end{bmatrix}\right) \tag{7.8}$$

remains positive for all tetrahedra.

(a) Reference.

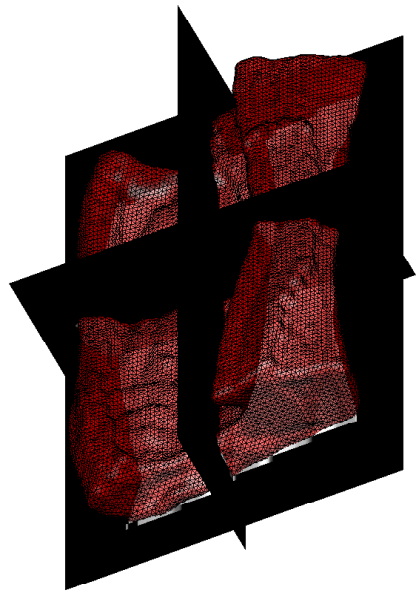

(b) Reference with surface mesh visualization of tessellation.

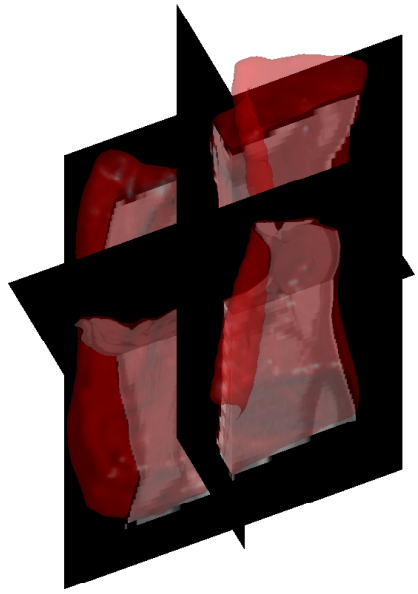

(c) Reference with surface visualization of tessellation.

Figure 7.4: Reference image with tessellation. The average volume of the tessellation elements is 27mm^3

7.3 Virtual cutting

The cutting in the abattoirs is based on a combination of anatomy and geometrical measuring. Figure 7.5 shows a few examples of the possible products which can be produced from the pork middle.

Figure 7.5(c) and Figure 7.5(d) contain a couple of typical loin products. Loin products are specified by the loin muscle, a trimmed fat layer on the outside of the loin with a thickness of x mm, and the inclusion or exclusion of the neighboring support muscles and ribs. Another typical product from the back area is *back bacon* (not shown in the figure) which consists of the back area without ribs and spine and with a width of 18 cm measured from the beginning of the skin closest to the spine along the surface of the skin.

From these examples we perceive that a cut may be guided by combination of:

Anatomical information The cut follows the boundary of some anatomical structure.

Semi-anatomical information The cut runs parallel with the boundary of some anatomical structure at an x mm distance.

Geometrical information The cut ensures that the product has some specific length or width.

Anatomical information can be embodied in an anatomical mask in the atlas and transferred to a target image by spatially normalizing the target against the reference of the atlas. As the transformation from the reference to the target is modeled with a piecewise affine transformation the inverse transformation is given explicitly, i.e

$$\hat{\boldsymbol{\phi}}_{\boldsymbol{V}}^{-1}(\boldsymbol{y}; \Delta \boldsymbol{V}) = \boldsymbol{\phi}_{\boldsymbol{V}+\Delta \boldsymbol{V}}(\boldsymbol{y}; -\Delta \boldsymbol{V}). \tag{7.9}$$

Thus, a voxel in the target image at the position $\boldsymbol{y}$ is inside some anatomical structure, if the mapped position $\hat{\boldsymbol{\phi}}_{\boldsymbol{V}}^{-1}$ is contained in the anatomical structure of the reference image.

Semi-anatomical information can be modeled similarly to purely anatomical information with the extension that the anatomical mask is dilated after being transferred to the target.

Cuts, which apply geometrical information for guidance, are the most difficult to handle as the deformable atlas provides limited geometrical information on

(a) 1648/1645

(b) 1838/1830/1836

(c) 1601

(d) 1660

(e) 1817

(f) 1826

Figure 7.5: Selected products from the Danish Crown product catalogue[39]. All products stem from the pork middle. The numbers written below the products are their product numbers.

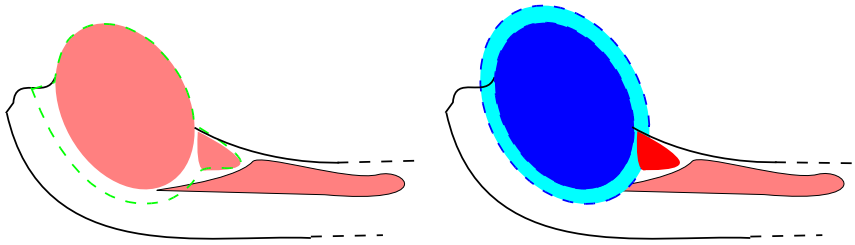

(a) Wanted cut. (b) Masked version of cut

Figure 7.6: Example of combinatorial masking.

the target. A tailored implementation for extracting a geometrical measure on a target image is in principal necessary for each cut employing geometrical information. In practice, most geometrical cuts can be modeled by measuring a distance of x mm from the left/right most point of the input product along the top/bottom surface of the product and then performing a vertical cut in the individual slices of the scan.

Most cuts will apply a combination of the different types of information. As anatomical and semi-anatomical information are represented by masks and geometrical information can be converted to mask representations, we combine the different types of information with the usual set operations such as *union* and *intersection*. Figure 7.6 displays a simple example of how to construct cuts by combining the different types of information. In Figure 7.6(a), we have a schematic drawing of a boneless pork middle with a broken green line representing the product, we want to cut. The product consists of the loin muscle with a trimmed fat layer and the dark muscle. The product can be modeled by dilating the transferred loin mask and uniting it with the transferred dark muscle mask. The masked modeled cutting is illustrated in Figure 7.6(b).

The cutting of a pig carcass can be viewed as a hierarchical tree, where the top node corresponds to the carcass, the internal nodes to the cuts, and the leaves to the end products. To maintain the simplest model possible we suggest to model the cutting of a carcass (or in this case the pork middle) with a binary tree. For each cut a mask embodies the main product, and the complement of the mask embodies the bi-product. The mask of an end product is extracted by traversing from the top node to the leaf of the end product. At each visited node, the mask of the parent is intersected with mask of the node or its complement depending on the path, and the resulting mask is forwarded on to the child in the path. The binary tree model from our cutting application is shown in Figure 7.7.

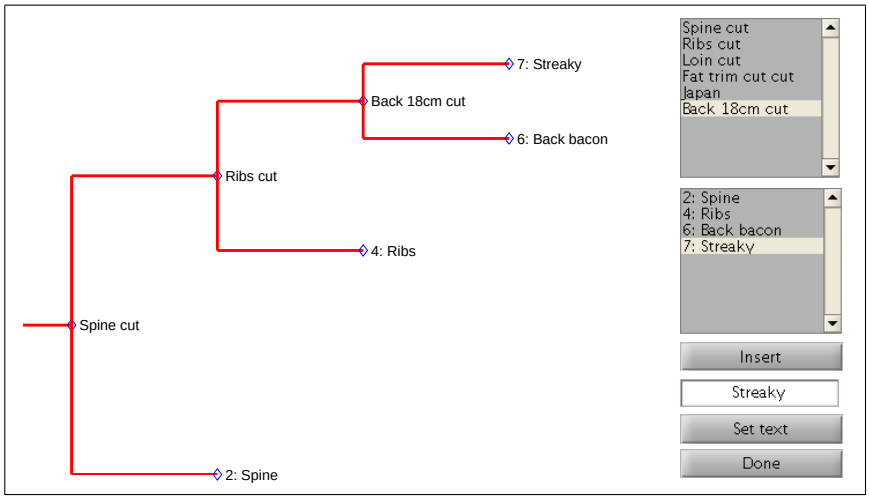

Figure 7.7: An example of cut hierarchy. Made from screen dump of cutting atlas application

Level	4	3	2	1	0
Avg. element vol. in mm^3	64	64	27	8	3.38
Gaus. scale space std. dev	4	3	2	1	0.5
α (E.q. 7.4)	5e-3	2.5e-3	1.2e-3	6e-4	3e-4

Table 7.1: Table of parameters used in multi-resolution image registration scheme.

7.4 Experiments

The Riemannian elasticity energy with $\mu = \lambda = 1$ was applied to normalize 299 CT scans against the reference scan. For a fast convergence a multi-resolution scheme was applied. Table 7.1 lists the parameters used for the different levels.

From the first experiments it was observed that existence of topological differences between reference image and target image led the registration to recover incorrect correspondences. The pork middle originates from the half pig carcasses which is made by splitting the carcass through the middle of the spine. The topological difference arises as the split is not perfectly symmetrical. It is estimated that 10-20% of the pigs in the data set have an unsymmetrical split which affects the registration. An example of the problem is displayed in Figure 7.8. To solve the problem the similarity measure is disabled in the tetrahedra situated in those areas. That is, only internal elastic forces drive the deformation of these tetrahedra. As a consequence the obtained correspondence

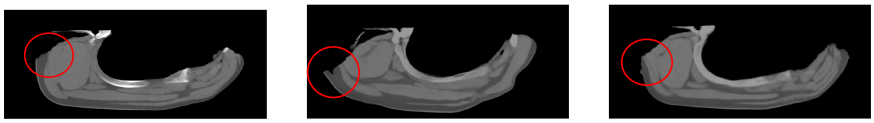

(a) Reference. (b) Target after rigid registration. (c) Target after non-rigid registration.

Figure 7.8: Example of misregistration due to topological difference.

may be suboptimal in the excluded areas.

Figure 7.9 (very skinny), Figure 7.10 (skinny), Figure 7.11 (normal), Figure 7.12 (fat with very unsymmetrical split) display the deformed images of the pig 214, pig 210, pig 270 and 100 after rigid, affine and non-rigid registration. The selected pigs represent the distribution w.r.t. fatness. In general, it seems that the registration is able to match the images and remove most of the skin folds and bends. From Figures 7.9(b,k) it is noticeable that the fat layer on the outside of the loin muscle is thinner in the non-rigidly registered image than in the reference image. This is a reappearing problem in many of the very skinny pigs.

As the anatomical masks shown in Figure 7.3(a) only have been traced in the reference and not in any of the remaining images in the database there are no ground truth data available for validating the registrations. To generate an artificial validation set the 299 resulting displacement fields of the registrations were fitted with a uniform tensor B-splines with a knot spacing of 15 mm. A compact deformation model was created by applying principal component analysis (PCA) on the fitted B-spline parameters. 11 modes of variation were selected explaining approximately 76% of the total variation. From the PCA model, 30 *virtual* pigs with anatomical masks were created by

- generating 30 virtual transformations by sampling the PCA model randomly,
- approximating the inverse transformations of the newly generated transformations by fitting uniform tensor B-splines,
- and finally interpolating the inverse transformations in the reference image and in the anatomical masks shown in Figure 7.3(a).

The virtual pigs were subsequently registered to the reference pig, and the dice scores between the anatomical masks of the reference and anatomical masks of the registered virtual pigs were computed. The mean dice scores for the

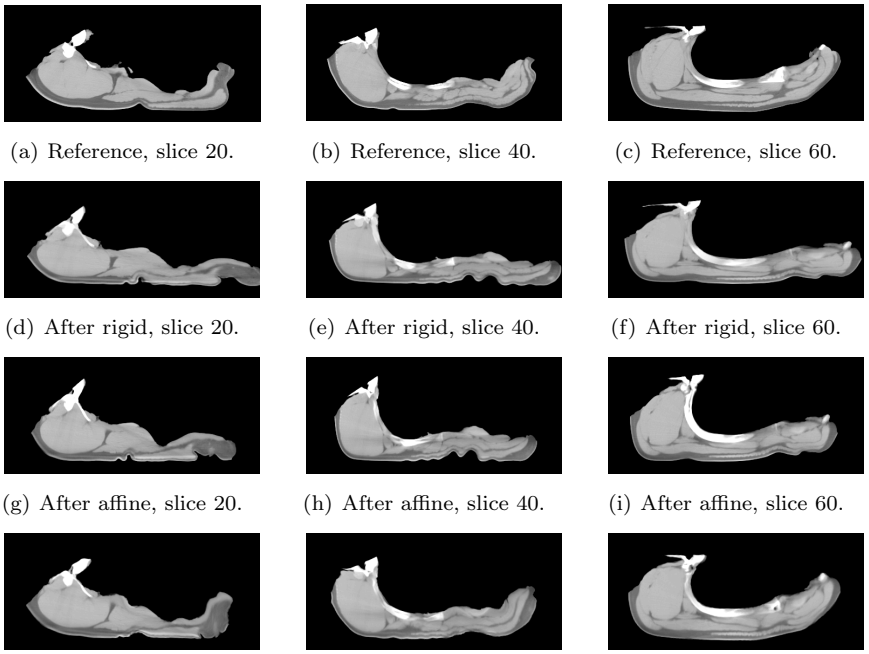

(a) Reference, slice 20. (b) Reference, slice 40. (c) Reference, slice 60.

(d) After rigid, slice 20. (e) After rigid, slice 40. (f) After rigid, slice 60.

(g) After affine, slice 20. (h) After affine, slice 40. (i) After affine, slice 60.

(j) After non-rigid, slice 20. (k) After non-rigid, slice 40. (l) After non-rigid, slice 60.

Figure 7.9: Registration result of pig 214. The figure displays slice, 20, 40 and 60 of the reference image and the template image after rigid registration, affine registration and non-rigid registration. The rows correspond to the images and the columns to the slices.

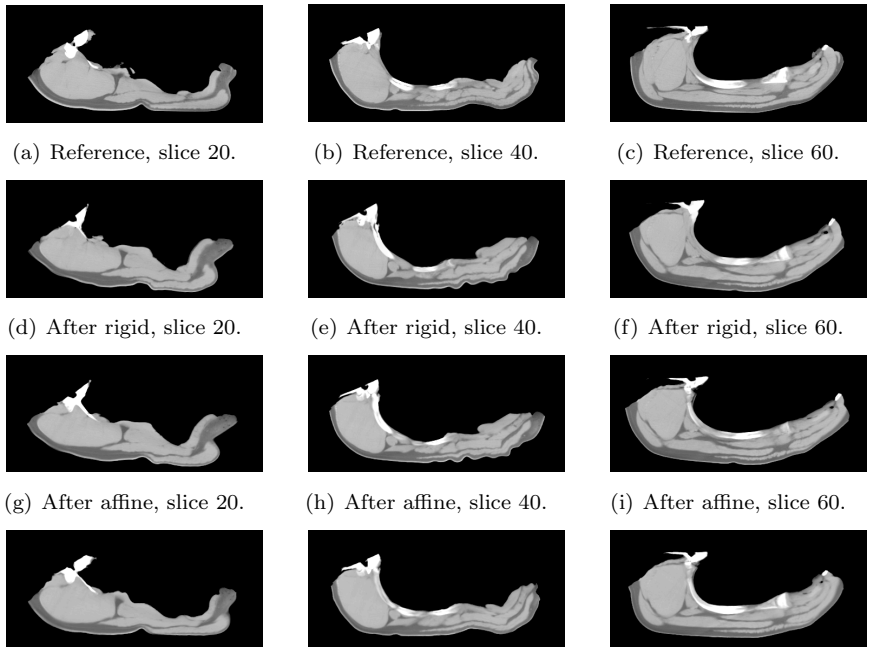

(a) Reference, slice 20. (b) Reference, slice 40. (c) Reference, slice 60.

(d) After rigid, slice 20. (e) After rigid, slice 40. (f) After rigid, slice 60.

(g) After affine, slice 20. (h) After affine, slice 40. (i) After affine, slice 60.

(j) After non-rigid, slice 20. (k) After non-rigid, slice 40. (l) After non-rigid, slice 60.

Figure 7.10: Registration result of pig 210. The figure displays slice, 20, 40 and 60 of the reference image and the template image after rigid registration, affine registration and non-rigid registration. The rows correspond to the images and the columns to the slices.

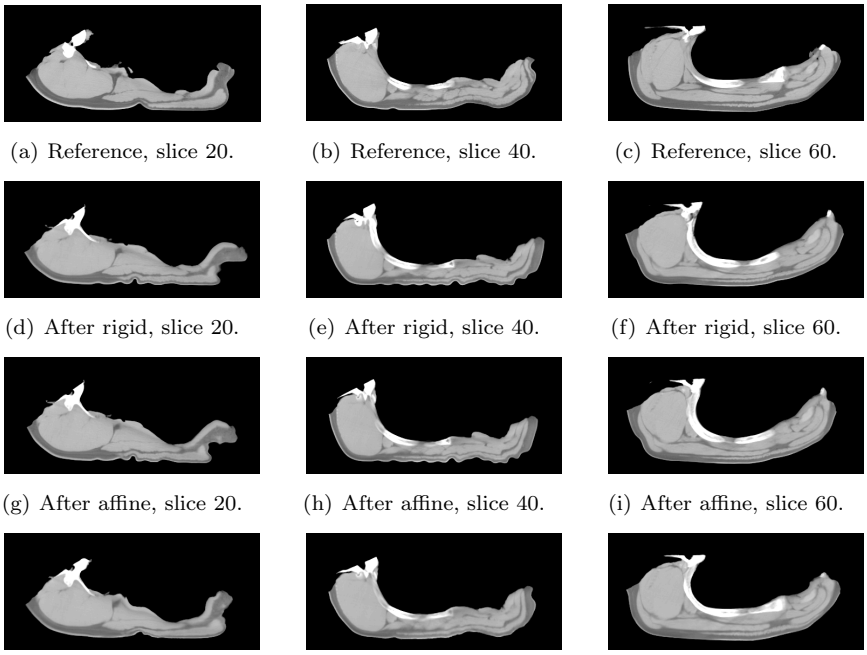

(a) Reference, slice 20. (b) Reference, slice 40. (c) Reference, slice 60.

(d) After rigid, slice 20. (e) After rigid, slice 40. (f) After rigid, slice 60.

(g) After affine, slice 20. (h) After affine, slice 40. (i) After affine, slice 60.

(j) After non-rigid, slice 20. (k) After non-rigid, slice 40. (l) After non-rigid, slice 60.

Figure 7.11: Registration result of pig 270. The figure displays slice, 20, 40 and 60 of the reference image and the template image after rigid registration, affine registration and non-rigid registration. The rows correspond to the images and the columns to the slices.

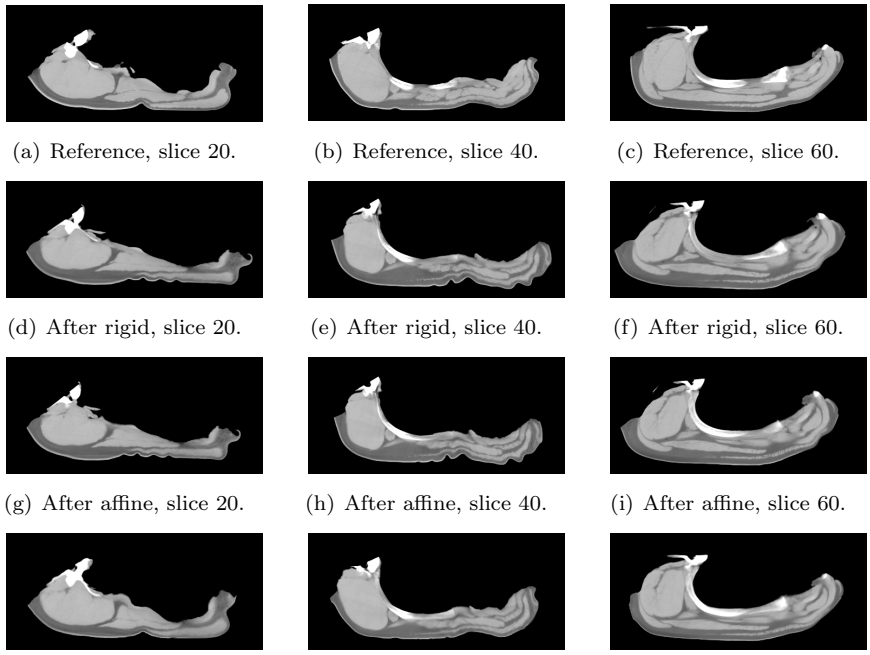

(a) Reference, slice 20. (b) Reference, slice 40. (c) Reference, slice 60.

(d) After rigid, slice 20. (e) After rigid, slice 40. (f) After rigid, slice 60.

(g) After affine, slice 20. (h) After affine, slice 40. (i) After affine, slice 60.

(j) After non-rigid, slice 20. (k) After non-rigid, slice 40. (l) After non-rigid, slice 60.

Figure 7.12: Registration result of pig 100. The figure displays slice, 20, 40 and 60 of the reference image and the template image after rigid registration, affine registration and non-rigid registration. The rows correspond to the images and the columns to the slices.

Loin	Ribs	Spine	Dark muscle	False lean
0.97	0.91	0.86	0.94	0.89

Table 7.2: Mean dice scores from registrations of the 30 virtually generated pigs.

anatomical masks are listed in Table 7.2. If the validation set was not statistically generated from a set of prior registrations the relative high dice score would have been impressive. It is however highly idealized that the differences between the reference image and the template image solely are due to a spatial deformation, and it is natural to expect that the applied deformation model can capture a deformation, which has been generated from a set of prior registrations with the same deformation model. We conservatively conclude that the pseudo validation did not uncover anything unexpected – and nothing else.

7.4.1 Examples of virtual cuts

This section presents two examples of virtual cuts on the pork middle. The first product range consists of (i) a spine (purple), (ii) a loin product with ribs and a width of 18 cm plus a 6 mm fat layer (red), (iii) spare ribs (blue), (iv) a layer of fat (green), and (v) a pork belly (yellow). The virtual products are shown in Figure 7.13 with the corresponding cutting tree.

The second product range consists of (i) a spine (purple), (ii) a loin product with the dark muscle and false lean plus a 4 mm fat layer (green), (iii) ribs (red), and (iv) a pork belly with some left-over skin and fat (blue). The virtual products are shown in Figure 7.14 with the corresponding cutting tree. The main product cut in Figure 7.14(a) is constructed by computing the intersection between the loin mask dilated 4 mm, the false lean mask dilated 4mm and the dark muscle mask.

The modeled product ranges demonstrate the versatility of our cutting tool. That is, they show that detailed and complex cutting can be achieved through a simple combination of masking, mathematical morphology (dilation) and set operations.

7.5 Discussion

This paper has presented a prototype for a virtual cutting framework based on a deformable atlas which applies elastic image registration to establish spatial

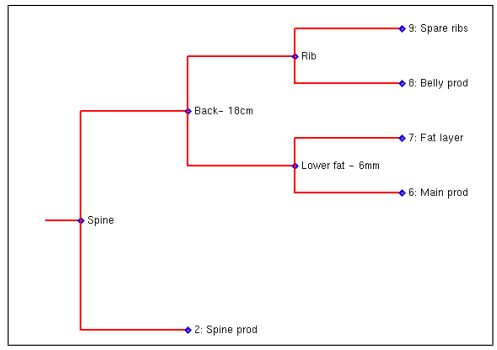

(a) Product tree.

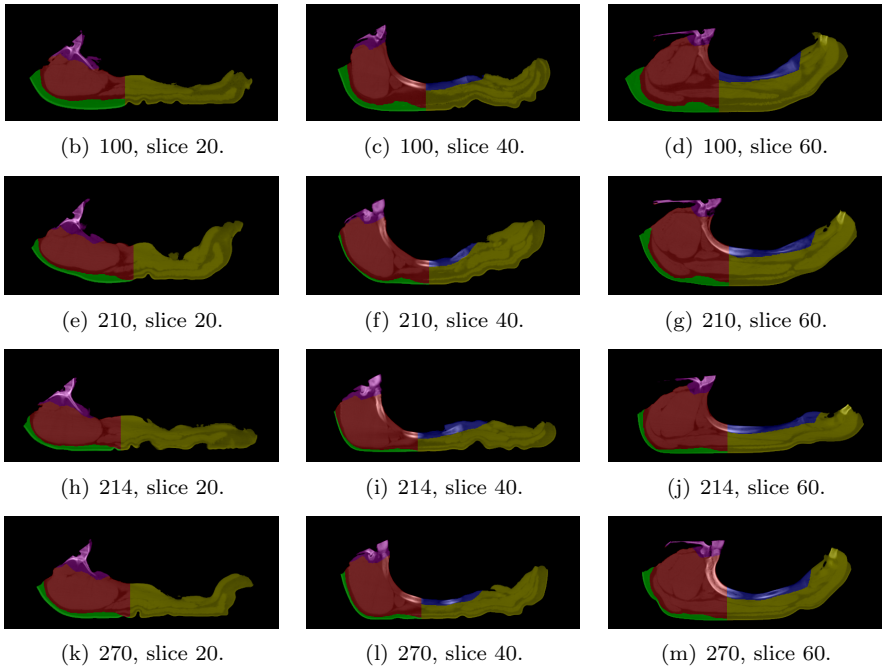

(b) 100, slice 20. (c) 100, slice 40. (d) 100, slice 60.

(e) 210, slice 20. (f) 210, slice 40. (g) 210, slice 60.

(h) 214, slice 20. (i) 214, slice 40. (j) 214, slice 60.

(k) 270, slice 20. (l) 270, slice 40. (m) 270, slice 60.

Figure 7.13: Superimpositions of first product range.

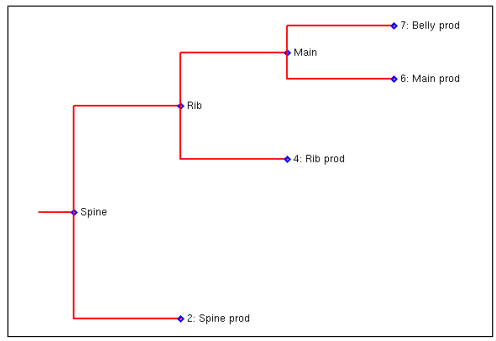

(a) Product tree.

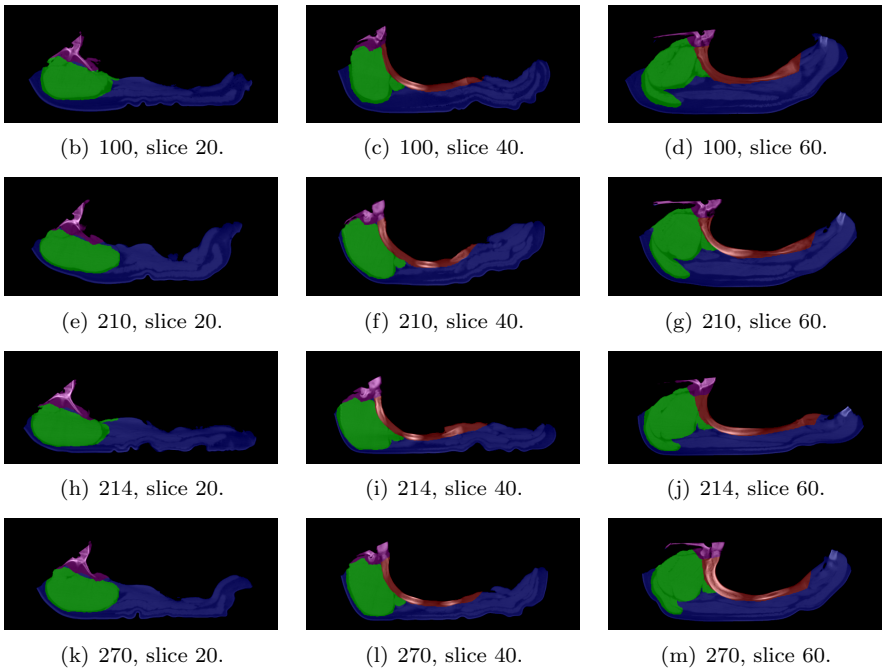

(b) 100, slice 20. (c) 100, slice 40. (d) 100, slice 60.

(e) 210, slice 20. (f) 210, slice 40. (g) 210, slice 60.

(h) 214, slice 20. (i) 214, slice 40. (j) 214, slice 60.

(k) 270, slice 20. (l) 270, slice 40. (m) 270, slice 60.

Figure 7.14: Superimpositions of second product range.

correspondence. The quality of the obtained registrations looks promising but awaits future validation. We propose to validate the registration in the future using 5 skinny, 10 normal and 5 fat pigs from the database. The same masks, as those traced upon the reference image, will be traced upon the validation pigs and subsequently compared to the transferred masks from the reference pig using the Dice score.

There is evidence indicating that the registration algorithm is having problems with capturing the deformations between the reference pig and skinny pigs. One way to solve this is to use multiple references in the atlas – one for skinny pigs, one for normal pigs and one for fat pigs. The fatness of an incoming pig would determine the reference of the registration.

The usage of masks for representing and constructing cuts makes the cutting framework flexible and adaptable to new cuts.

Chapter 8

Validation of virtual cuts

Mads Fogtmann Hansen and Rasmus Larsen

Abstract

This paper presents a methodology for comparing virtual cuts against real cuts from the abattoirs. The Danish meat research institute plans to use virtual cutting on a representative set of Computed Tomography (CT) scans of pig to simulate different cut scenarios with goal of ensuring that every pig passing through the abattoirs is cut into the optimal selection of products. For such an application to be a success, it is a necessity that the virtual products resemble the real products sufficiently well. In this pilot study, we compare so-called virtual *back 2* products extracted from CT scans of pork middles with CT scans of the real *back 2* products. As products non-rigidly deform subsequent to the cutting, virtual and real products cannot be compared until this deformation have been estimated. We apply a nearly incompressible elastic image matching technique to recover the deformation and use the Euclidean surface-to-surface distance to evaluate the resemblance of the virtual products. The study revealed an overall satisfactory resemblance between virtual and real back 2 products but with the existence of unwanted inconsistencies.

8.1 Introduction

The Danish Meat Research Institute (DMRI) and DTU Informatics are currently constructing a virtual cutting atlas which can be used to simulate different cut scenarios on a database of Computed Tomography (CT) scans of pig carcasses [168]. This atlas will enable DMRI to experiment with new cuts and to relate

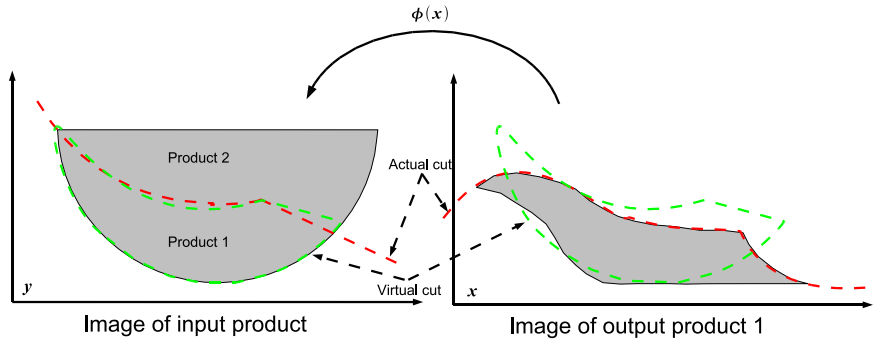

Figure 8.1: Illustration of deformation problem.

the biological variation of pigs against a set of possible products to determine the optimal selection of products for the specific type of pig.

For a cutting atlas to be of value the virtual cuts have to resemble the real cuts from the abattoirs, and vice versa. To ensure a good consistency between the virtual cuts and the real cuts, we propose to CT scan the input product and the output products of a cut, and subsequently to compare the output products with the similar virtual output products extracted from scan of the input product.

As soft tissue behaves similarly to rubber materials the output products of a cut will often undergo large non-rigid deformations after the execution of the cut. This makes a direct geometrical comparison between the virtual products and the real products meaningless. The problem is illustrated in Figure 8.1. In Figure 8.1 an input product (left coordinate system) is cut into two products along the broken red line. After the cut product 1 is deformed producing the deformed product shown in the right coordinate system. Before the virtual product 1 (represented by the broken green line) can be compared to the real product 1, the real product 1 has to be spatially normalized against the input product. That is, the geometrical transformation $\boldsymbol{\phi}(\boldsymbol{x})$ between the right and the left coordinate has to be estimated to recover the undeformed version of the real cut in the left coordinate system.

We apply an elastic image registration approach to recover the transformation between the deformed output product and the input product, and measure the surface-to-surface distance between the virtual output product and the spatially normalized output product to quantify and visualize the difference.

8.1.1 Data

The data used in this study consist of 37 CT scans of the pork middle of pigs (cf. Figure 8.2 (a)) and 37 CT scan of the resulting output products of the pork middle cutting robot (cf. Figure 8.2 (b)). The output products from the the top-left to the bottom-right are *pork belly*, *back 2*, *ribs*, *spine*. Voxel dimensions are $[0.87 \times 0.87 \times 10]\text{mm}^3$ with a 10mm spacing between consecutive slices. The scans were constructed with a reconstruction algorithm which emphasizes bone. As a consequence of this choice the meat and fat tissue areas are noisy and affected by shade artifacts from the bones.

As the back 2 product is the main product of the cut, this paper will focus on the comparison between the real and the virtual back 2 products. From the remainder of this paper we will refer to the back 2 product as the output product and the pork middle as the input product.

The BackBatch program developed from the master thesis work of Hansen [74] produces virtual back 2 products from CT scans of the pork middle of pigs. 37 virtual back 2 products were extracted from the 37 CT scans of the pork middle with the BackBatch program. An example of a virtual back 2 product is shown in Figure 8.2 (c). For simplicity all virtual products have a length of 41cm measured perpendicular to the slice planes which is realized by including 20 slices on either side of the middle slice of the CT scan of the pork middle.

To aid the registration corresponding landmarks have been placed in the pork middle and in the back 2 product. The landmarks were placed by identifying approximately corresponding slices in the input product scan and the output product scan, and then placing a number of in-slice correspondence points (1-4 landmarks per slice). Note, the landmarks are of a questionable quality due to the low out-plane resolution and to small changes in the orientation between the scans. As such the landmarks can only be used as initial guidance marks for the registration and not as ground truth.

Figure 8.3 shows the histogram of the voxel intensities in the back 2 product of pig 1. The first and second peak correspond to fat and muscle, respectively. It is observed that both the muscle intensities and fat intensities look nearly normally distributed.

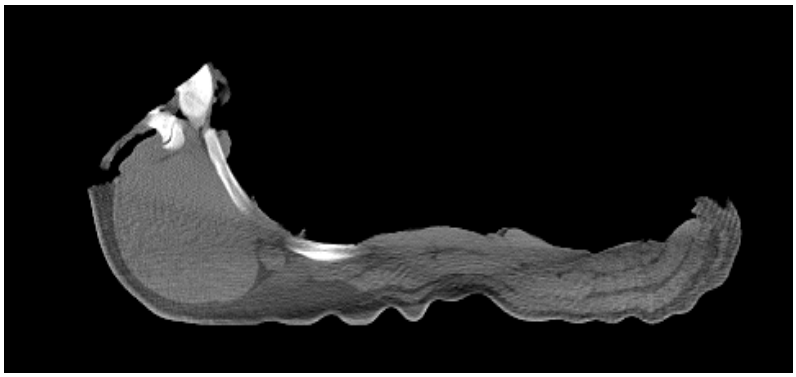

(a) Pork middle.

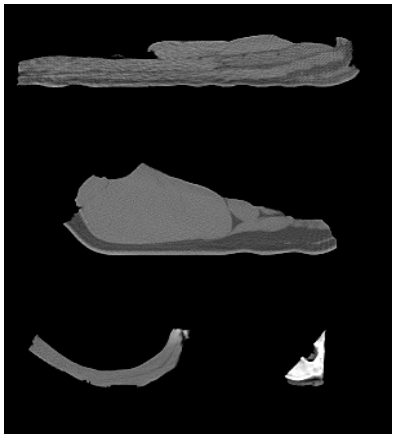

(b) Products.

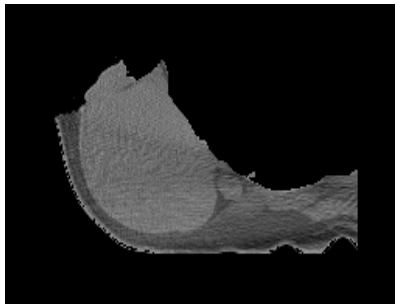

(c) Virtual back 2 product.

Figure 8.2: Selected slices from pig 1.

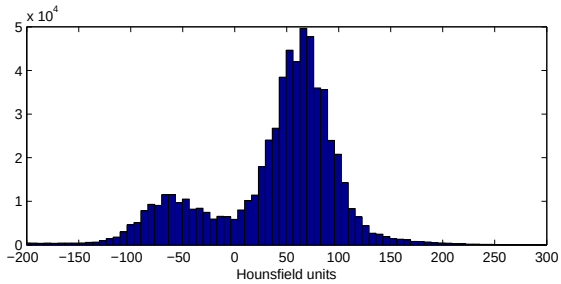

Figure 8.3: Histogram of the voxel intensities in back 2 product of pig 1. The first peak is fat, and the second peak is meat.

8.2 Related work

Elastic image matching was originally proposed by Broit [24] and completed by Bajcsy et. al. [14, 15]. Broit and Bajcsy et. al. applied linear elasticity to regularize the deformation, which was a synonym for elasticity in general until Pennec et. al. [122] introduced the use of Riemannian elasticity. Riemannian elasticity is in contrast to linear elasticity rotation invariant and can therefore model much larger and more complex deformations. The viscous elastic or fluid registration approach by Christensen [31] is closely related to linear elastic image registration but differentiates itself by regularizing the flow of the deformation rather than the spatial displacements.

This study separates itself from most non-linear intra-subject registration studies and applications such as early diagnosis and monitoring of the progression of dementia [25, 62, 63] as our deformation is nearly incompressible. Volume-preserving or nearly volume preserving image registration has been applied for the registration pre- and post-contrast MRIs of female breasts [71, 128, 159]. Haber et. al. [71] combine a volume-preserving hard constraint with ordinary linear elasticity, and Tanner et. al. [159] and Rohlfing et. al. [128] combine a tensor B-spline representation of the geometrical transformation with a volume penalty term. We believe that the use of linear elasticity in [71] and the B-spline representation in [128, 159] render both approaches incapable of modeling the relatively large non-rigid deformation between input and output products.

Inspired by virtual surgical application [93, 173], we apply a nearly incompressible Ogden material model to regularize the deformation. The primary reason for using the Ogden model is that it is considered to be the reference model for rubber materials. Soft tissues fall into this category of materials. DMRI and DTU Informatics are currently working on the development of models for soft tissue deformation in pig carcasses by scanning products with inserted steel markers prior to and after a deformation. Mosbech et. al. [111] present a preliminary study.

8.3 Spatial normalization

For the image registration process, we select the output product scan to be the reference image, the input product scan to be the deformable template image, and restrict the domain Ω of the reference image to the spatial positions in the output product scan which lay within the output product. The choice is an implication of the fact that there only exists a partial mapping from the input

product scan to the output product scan – an input product is cut into multiple output products.

8.3.1 Image and landmark matching

To drive the registration between reference and the template image we apply a mixture of image matching and landmarks matching. The inclusion of landmarks is necessary as the deformation between input and output product is too large for an initial rigid or affine registration to provide a sufficiently good starting estimate for the non-rigid registration.

We apply the mean squared difference dissimilarity measure as the image matching criterion as the only difference between the images in principal should be some spatial deformation, and as the Gaussian sensor model is appropriate for these CT scans (cf. section 8.1.1). Thus, the dissimilarity is given by

$$\mathcal{D}[R, T, \boldsymbol{\phi}] = \frac{1}{2V_\Omega} \int_\Omega (R(\boldsymbol{x}) - T_\phi(\boldsymbol{x}))^2 d\boldsymbol{x}, \tag{8.1}$$

where $T\phi = T \circ \boldsymbol{\phi}$ is the deformed template image, R is the reference image and V_Ω is the volume of the domain.

To match a set of landmarks $\{\boldsymbol{x}_i\}$ with a set of a corresponding set of landmarks $\{\boldsymbol{y}_i\}$ we use the mean squared Euclidian distance, i.e.

$$\mathcal{L}[\{\boldsymbol{x}_i\}, \{\boldsymbol{y}_i\}, \boldsymbol{\phi}] = \frac{1}{2M} \sum_i^M \langle \boldsymbol{\phi}(\boldsymbol{x}_i) - \boldsymbol{y}_i, \boldsymbol{\phi}(\boldsymbol{x}_i) - \boldsymbol{y}_i \rangle, \tag{8.2}$$

where M is the number of landmarks.

8.3.2 Spatial deformation modeling

Biological studies [42, 81, 95, 117, 118, 137, 156, 158, 161] show that biological tissues are nearly incompressible and compliant to shear, which makes biological tissue similar to rubber. The reference model for modeling the elastic potential energy in rubber-like materials subject to a deformation $\boldsymbol{\phi}$ is the Ogden material model [115]

$$\mathcal{S}[\boldsymbol{\phi}] = \frac{1}{V_\Omega} \int_\Omega \sum_{p=1}^{Q} \frac{\mu_p}{\alpha_p} \left(-3 + \operatorname{tr} \left(\boldsymbol{C}(\boldsymbol{x})^{\frac{\alpha_p}{2}} \right) \right) = \frac{1}{V_\Omega} \int_\Omega \sum_{p=1}^{Q} \frac{\mu_p}{\alpha_p} \left(-3 + \sum_{i=1}^{3} \lambda_i^{\alpha_p} \right) d\boldsymbol{x}, \tag{8.3}$$

where Q, α_p and μ_i are material constants, $\boldsymbol{C}(\boldsymbol{x}) = \nabla\boldsymbol{\phi}(\boldsymbol{x})^T\nabla\boldsymbol{\phi}(\boldsymbol{x})$ and λ_i is the ith principal stretch. The Ogden model is only valid for compressible materials and as such assumes that the constraint $\det(\nabla\boldsymbol{\phi}(\boldsymbol{x})) = 1$ is fulfilled. For nearly incompressible materials the principal stretches are normalized, and a volume penalty term is introduced, i.e.

$$\begin{aligned}\mathcal{S}_2[\boldsymbol{\phi}] &= \frac{1}{V_\Omega}\int_\Omega \sum_{p=1}^{Q}\frac{\mu_p}{\alpha_p}\left(-3+\det(\boldsymbol{C}(\boldsymbol{x}))^{-\frac{\alpha_p}{6}}\operatorname{tr}\left(\boldsymbol{C}(\boldsymbol{x})^{\frac{\alpha_p}{2}}\right)\right)+\beta\log(\det(\boldsymbol{C}(\boldsymbol{x})))^2 d\boldsymbol{x}\\ &= \frac{1}{V_\Omega}\int_\Omega \sum_{p=1}^{Q}\frac{\mu_p}{\alpha_p}\left(-3+\sum_{i=1}^{3}\tilde{\lambda_i}^{\alpha_p}\right)+\beta\left(\sum_{i=1}^{3}\log\lambda_i\right)^2 d\boldsymbol{x} \qquad (8.4)\end{aligned}$$

where $\tilde{\lambda}_i = \lambda_i(\prod_{i=1}^{3}\lambda_i)^{-\frac{1}{3}}$ and β is a constant controlling the volume penalty.

8.3.3 Discretization and optimization

The template image T is registered to the reference image R by minimizing the cost function

$$\mathcal{D}[R,T,\boldsymbol{\phi}]+\gamma\mathcal{L}[\{\boldsymbol{x}_i\},\{\boldsymbol{y}_i\},\boldsymbol{\phi}]+\mathcal{S}_2[\boldsymbol{\phi}] \qquad (8.5)$$

w.r.t. $\boldsymbol{\phi}(\boldsymbol{x})$, where γ controls the influence of the landmarks.

To minimize Eq. 8.5 w.r.t. transformation $\boldsymbol{\phi}(\boldsymbol{x})$, the transformation is discretized using finite elements by tessellating the mask of the output product in the reference image with a tetrahedral mesh. Our tessellation method is described in details in [76]. At each vertex of the mesh a vector describes the spatial displacement of the vertex. The transformation $\boldsymbol{\phi}(\boldsymbol{x})$ of a point $\boldsymbol{x}$ inside the tetrahedron defined by the vertices $\boldsymbol{V}$ is approximated linearly, i.e.

$$\boldsymbol{\phi}(\boldsymbol{x}) \approx \hat{\boldsymbol{\phi}}_{\boldsymbol{V}}(\boldsymbol{x};\Delta\boldsymbol{V}) = \boldsymbol{x}+\Delta\boldsymbol{V}\begin{bmatrix}\boldsymbol{V}\\ \mathbf{1}\end{bmatrix}^{-1}\boldsymbol{x} = \boldsymbol{x}+\Delta\boldsymbol{V}\boldsymbol{D}\boldsymbol{x}, \qquad (8.6)$$

where $\Delta\boldsymbol{V}$ is the displacement of the vertices $\boldsymbol{V}$. Thus, the spatial gradient of discretized transformation is

$$\nabla\hat{\boldsymbol{\phi}}_{\boldsymbol{V}}(\boldsymbol{x};\Delta\boldsymbol{V}) = \mathbf{I}+\Delta\boldsymbol{V}\boldsymbol{D}. \qquad (8.7)$$

The dissimilarity measure is discretized with the usual midpoint quadrature with the same tessellation as used to discretize the transformation. The discretized version of Eq. 8.5 is minimized using the conjugated gradient optimization method.

8.4 Evaluating the distance between cuts

We evaluate the distance between real and corresponding virtual products by computing the Euclidean surface-to-surface distance between the products. The surface-to-surface distance is computed by

(i) transferring the mask of deformed product using the inverse transformation of $\boldsymbol{\phi}(\boldsymbol{y})$ to the coordinate system of the input product,

(ii) converting the mask of the virtual product and the transferred mask to signed distance maps,

(iii) extracting the iso-surfaces of the signed distance maps,

(iiii) and finally interpolating the iso-surface of the virtual product in the distance map of the transferred mask and the iso-surface of the non-deformed real product in the distance map of the mask of the virtual product.

As the transformation from the reference image to the template image is modeled with a piecewise affine transformation the inverse transformation is given explicitly by

$$\hat{\boldsymbol{\phi}}_{\boldsymbol{V}}^{-1}(\boldsymbol{y}; \Delta \boldsymbol{V}) = \boldsymbol{\phi}_{\boldsymbol{V}+\Delta \boldsymbol{V}}(\boldsymbol{y}; -\Delta \boldsymbol{V}). \tag{8.8}$$

8.5 Validation of virtual cuts

For the image registration a simple Ogden model was used with $Q = 1$ and $\alpha_1 = 12$ for both muscle and fat tissue. Oomens et. al. [117] reported empirical derived values $\alpha_1 = 30$ and $\alpha_1 = 5$ for muscle and fat tissue respectively in living humans. We have experimented with a common α_1 between 5 and 30, and it is our experience that any $10 \leq \alpha_1 \leq 20$ yield almost identical registration results. Moreover, we applied a multi-level registration scheme for a faster convergence. The parameters for the different levels are listed in Table 8.1.

Figure 8.4 displays the surface of the tetrahedral mesh representation of the output product in the output product scan and the surface of the deformed tetrahedral mesh in the input product scan at the end of the level 2 registration of pig 1[1]. From Figure 8.4(d), we observe that the deformed mesh closely borders the ribs which is expected for a quality registration.

[1]Level 2 was chosen for the visualization as lower level meshes become to dense for visualization.

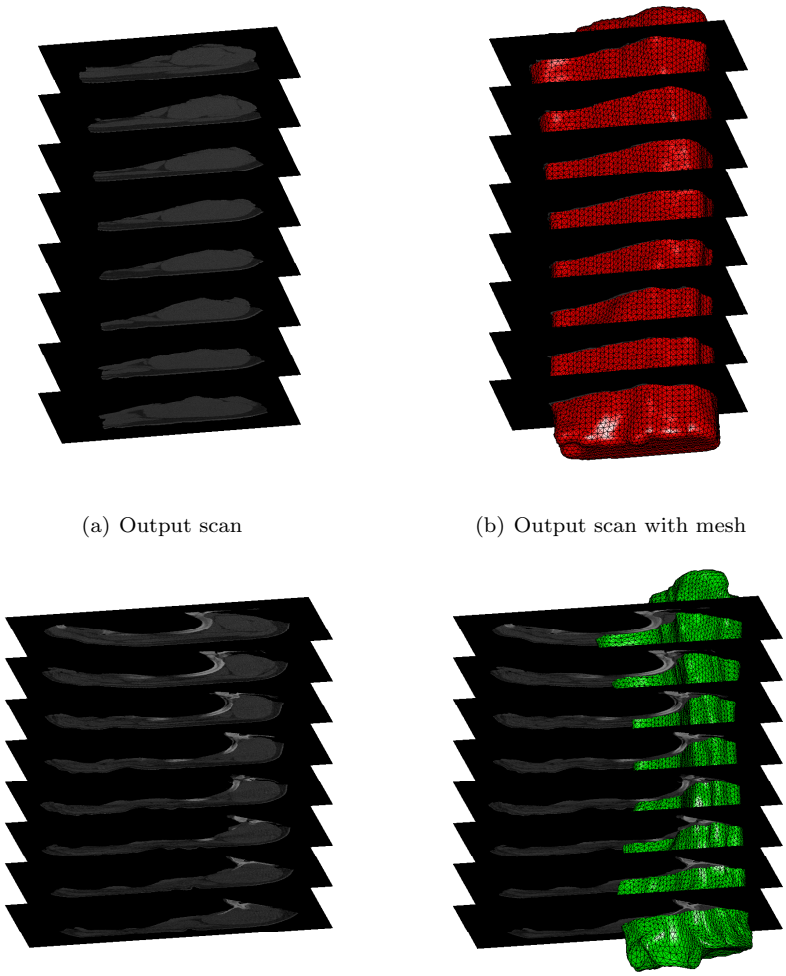

(a) Output scan

(b) Output scan with mesh

(c) Input scan

(d) Input scan with deformed mesh

Figure 8.4: Tetrahedral mesh on slice visualization of CT scans.

Level	3	2	1	0
Avg. element vol. in mm^3	64	27	8	3.38
Gaus. scale space std. dev (mm)	2	1.5	1	0.5
α_1	12	12	12	12
β	0.05	0.1	0.2	0.4
μ_1	1e-5	0.5e-6	0.25e-6	0.1e-6
γ	10	5	2.5	0

Table 8.1: The used registration parameters for each level.

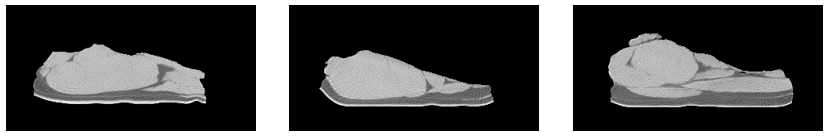

(a) $R(\boldsymbol{x})$ slice 10 (b) $R(\boldsymbol{x})$ slice 30 (c) $R(\boldsymbol{x})$ slice 50

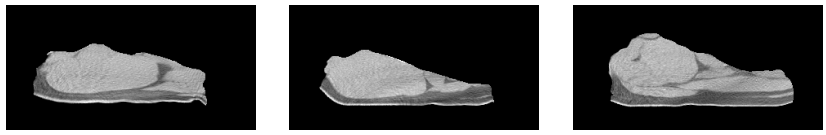

(d) $T(\boldsymbol{\phi}(\boldsymbol{x}))$ slice 10 (e) $T(\boldsymbol{\phi}(\boldsymbol{x}))$ slice 30 (f) $T(\boldsymbol{\phi}(\boldsymbol{x}))$ slice 50

Figure 8.5: Slice comparison of back 2 scan and registered back 2 of pig 1.

Figures 8.5-8.7 show slice-by-slice illustrations of the reference image and the deformed template image for pig 1, 2 and 3. The reference and the deformed template images are in general very similar but there is a noticeable difference in the top of slice 50 for pig 1.

Columns 2-5 in Table 8.2 list the minimum, maximum, mean and the standard deviation of the determinant of the Jacobian of the transformation. The determinant of the Jacobian quantifies the amount of local compression or expansion. A determinant of the Jacobian larger than 1 indicates a local expansion, a determinant of the Jacobian smaller than 1 indicates a local compression, and finally a determinant of the Jacobian smaller than 0 indicates a local folding. As the deformation is nearly incompressible it is expected that the determinant of the Jacobian in every spatial location is close to 1. From the fourth and fifth column in Table 8.2 we observe that the mean determinant of the Jacobian is very close to 1 for all registrations, and that the standard deviation for all but one of the registrations ranges between 0.010 and 0.020. Thus, we conclude that the estimated deformations are nearly volume preserving. The combination of a good visual resemblance between the reference images and the deformed template images and the nearly volume preserving deformation adds evidence to

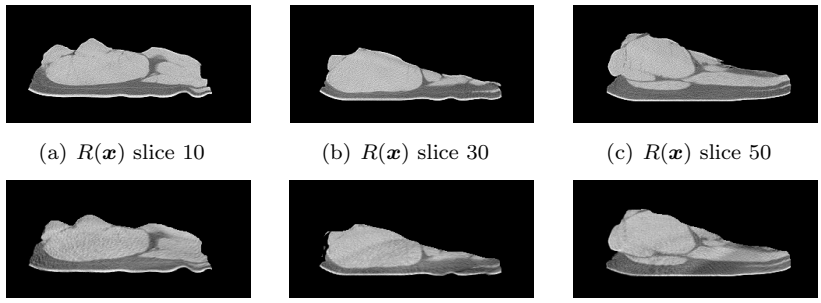

(a) $R(\boldsymbol{x})$ slice 10 (b) $R(\boldsymbol{x})$ slice 30 (c) $R(\boldsymbol{x})$ slice 50

(d) $T(\boldsymbol{\phi}(\boldsymbol{x}))$ slice 10 (e) $T(\boldsymbol{\phi}(\boldsymbol{x}))$ slice 30 (f) $T(\boldsymbol{\phi}(\boldsymbol{x}))$ slice 50

Figure 8.6: Slice comparison of back 2 scan and registered back 2 of pig 2.

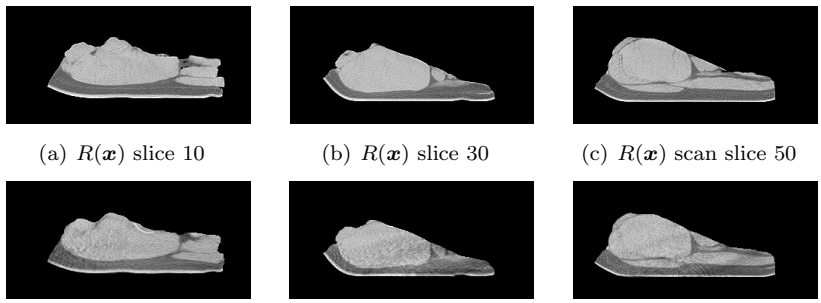

(a) $R(\boldsymbol{x})$ slice 10 (b) $R(\boldsymbol{x})$ slice 30 (c) $R(\boldsymbol{x})$ scan slice 50

(d) $T(\boldsymbol{\phi}(\boldsymbol{x}))$ slice 10 (e) $T(\boldsymbol{\phi}(\boldsymbol{x}))$ slice 30 (f) $T(\boldsymbol{\phi}(\boldsymbol{x}))$ slice 50

Figure 8.7: Slice comparison of back 2 scan and registered back 2 of pig 3.

the validity of the registration.

Figures 8.8-8.10 contain the surfaces of the virtual products for the first 18 pigs color-coded with the minimum distance to the surface of the spatially normalized output products, and vice versa. A couple of general trends can be observed in the figures:

- Indentations from the ribs and spine are clearly visual on virtual products but not on the real products, which suggest that the virtual cuts follows the surfaces of the ribs and spine to closely.
- The virtual products seem to be wider in the middle and more narrow in the ends.

The quartiles of the absolute surface-to-surface distances are listed in the last two columns of Table Figure 8.2. Whether, this is acceptable or not, is a question for the expert butcher.

8.6 Discussion

This paper presented a methodology for the comparison of the virtual and real cuts. The comparison method was demonstrated on a set of virtual and real back 2 products. In general, there was a good consistency between the virtual and the real products but a couple of tendencies or biases were discovered. Thus, we conclude that the resemblance of virtual back 2 product and against the real back 2 product can be improved.

The quality of the geometrical comparison is dependent on the estimate of the deformation between the real output product and the input product. Unfortunately, there are a number of weaknesses in the obtained registration:

- The reliance on landmarks for initial guidance of the registration threatens the applicability of the method. The need for landmarks can probably be eliminated by placing the products in a half pipe while scanned in order to preserve the the natural curve of the product and to decrease the size of the deformation between input and output products. As an alternative approach it may be possible simulate the deformation of the output product prior to the registration. In this example, one could try to simulate how gravity deforms the pork middle without ribs and then register the back 2 product to the deformed pork middle.

	$\det(\nabla\phi)$				Quartiles	
ID	Min	Max	Mean	Std.	R→V	V→R
1	0.858	1.169	1.000	0.014	0.67 /1.20 /3.06	0.74 /1.50 /4.39
2	0.811	1.162	1.000	0.020	0.58 /1.13 /2.51	0.67 /1.42 /3.94
3	0.902	1.099	1.000	0.010	0.66 /1.18 /2.21	0.72 /1.34 /2.93
4	0.881	1.150	1.000	0.032	0.74 /1.32 /3.34	0.76 /1.52 /4.21
5	0.848	1.170	1.000	0.012	0.77 /1.53 /4.76	0.83 /1.64 /5.24
6	0.890	1.099	1.000	0.015	0.64 /1.15 /2.13	0.70 /1.33 /2.98
7	0.846	1.178	1.000	0.012	0.76 /1.47 /3.33	0.77 /1.53 /4.49
8	0.856	1.173	1.000	0.010	0.75 /1.39 /2.93	0.77 /1.51 /3.87
9	0.855	1.126	1.000	0.010	0.80 /1.47 /3.15	0.87 /1.56 /4.37
10	0.810	1.163	1.000	0.014	0.83 /1.53 /3.39	0.93 /1.66 /4.33
11	0.861	1.147	1.000	0.011	0.73 /1.31 /2.76	0.76 /1.49 /3.86
12	0.881	1.147	1.000	0.012	0.74 /1.32 /2.39	0.76 /1.53 /3.85
13	0.871	1.120	1.000	0.011	0.76 /1.38 /2.53	0.77 /1.53 /3.82
14	0.841	1.176	1.000	0.015	0.76 /1.49 /3.13	0.82 /1.59 /4.53
15	0.849	1.174	1.000	0.011	0.74 /1.36 /2.93	0.76 /1.50 /3.57
16	0.891	1.105	1.000	0.010	0.76 /1.53 /3.36	0.77 /1.58 /3.66
17	0.871	1.133	1.000	0.012	0.72 /1.37 /2.70	0.76 /1.56 /3.86
18	0.867	1.126	1.000	0.011	0.62 /1.16 /2.53	0.71 /1.42 /3.84
19	0.845	1.153	1.000	0.012	0.76 /1.35 /3.36	0.77 /1.51 /4.26
20	0.870	1.129	1.000	0.013	0.72 /1.30 /2.26	0.75 /1.42 /2.76
21	0.875	1.156	1.000	0.012	0.73 /1.39 /3.15	0.76 /1.59 /4.72
22	0.880	1.114	1.000	0.011	0.76 /1.47 /2.94	0.81 /1.55 /4.51
23	0.861	1.158	1.000	0.012	0.72 /1.40 /3.89	0.75 /1.50 /4.48
24	0.829	1.169	1.000	0.012	0.81 /1.54 /3.65	0.90 /1.70 /4.64
25	0.853	1.168	1.000	0.011	0.75 /1.40 /3.75	0.76 /1.53 /4.80
26	0.863	1.157	1.000	0.012	0.76 /1.33 /2.29	0.76 /1.45 /2.89
27	0.903	1.091	1.000	0.011	0.76 /1.44 /2.90	0.78 /1.53 /3.67
28	0.892	1.122	1.000	0.010	0.75 /1.41 /3.06	0.75 /1.41 /2.99
29	0.890	1.111	1.000	0.011	0.74 /1.39 /2.99	0.76 /1.51 /3.91
30	0.854	1.129	1.000	0.010	0.76 /1.51 /3.06	0.77 /1.53 /4.08
31	0.864	1.127	1.000	0.012	0.71 /1.39 /3.22	0.76 /1.53 /4.44
32	0.868	1.117	1.000	0.011	0.70 /1.29 /3.49	0.73 /1.41 /4.04
33	0.864	1.100	1.000	0.011	0.71 /1.43 /3.82	0.76 /1.58 /5.16
34	0.885	1.109	1.000	0.012	0.65 /1.31 /3.22	0.69 /1.44 /3.87
35	0.855	1.143	1.000	0.012	0.77 /1.51 /3.82	0.86 /1.77 /5.39
36	0.841	1.207	1.000	0.015	0.78 /1.53 /3.91	0.81 /1.53 /4.38
37	0.876	1.120	1.000	0.011	0.76 /1.44 /3.03	0.80 /1.53 /3.98

Table 8.2: The table lists the minimum, maximum, mean and the standard deviation of determinant of the Jacobian of the recovered transformations as well the mean absolute surface-to-surface distance between the virtual and real output product. Distances are in mm, and $V \rightarrow R$ is an abbreviation for the distance from the surface of the virtual product to the surface of the real spatial normalized product.

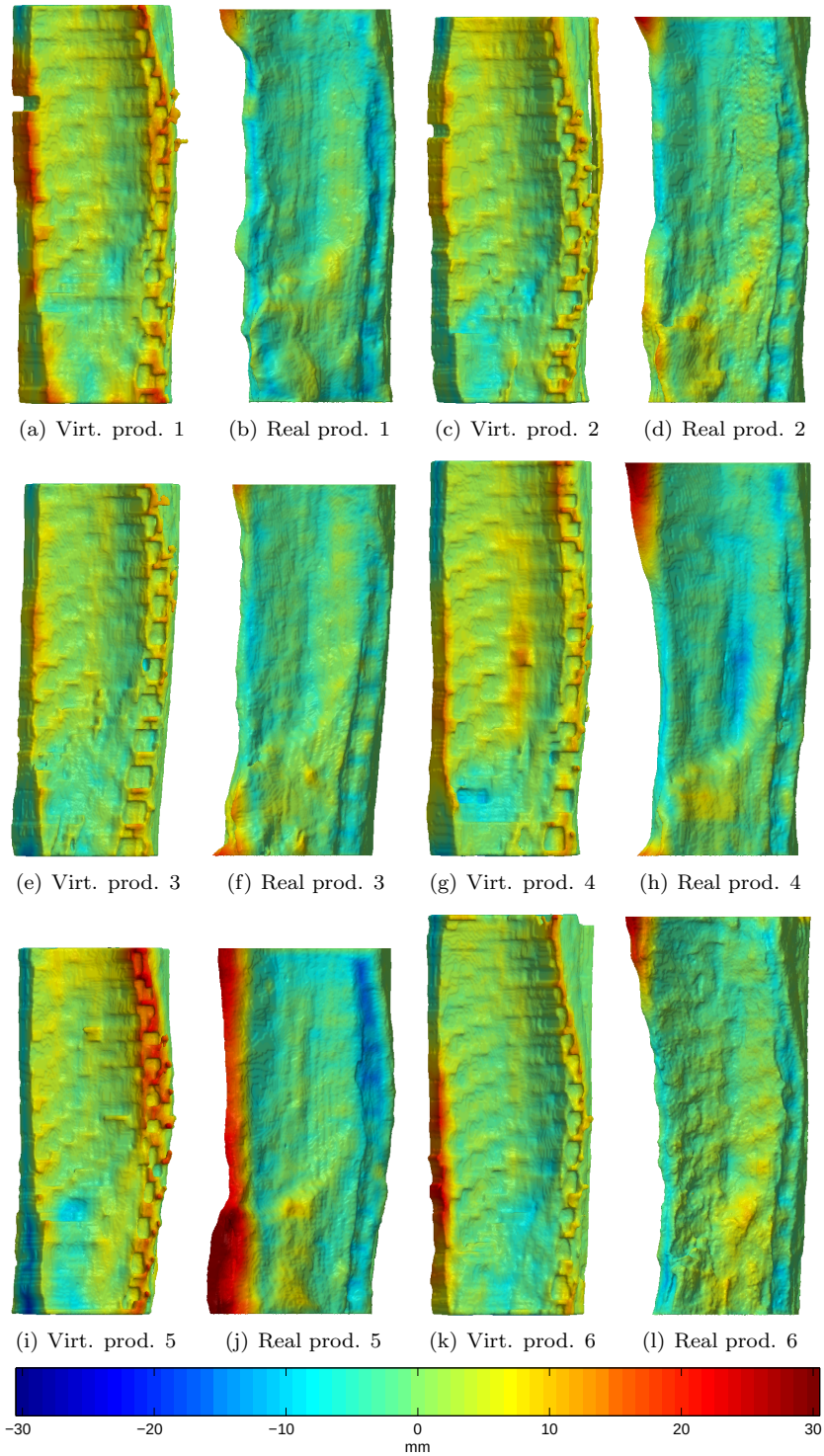

(a) Virt. prod. 1 (b) Real prod. 1 (c) Virt. prod. 2 (d) Real prod. 2

(e) Virt. prod. 3 (f) Real prod. 3 (g) Virt. prod. 4 (h) Real prod. 4

(i) Virt. prod. 5 (j) Real prod. 5 (k) Virt. prod. 6 (l) Real prod. 6

Figure 8.8: 3D Surface distance plots. Pigs 1-6

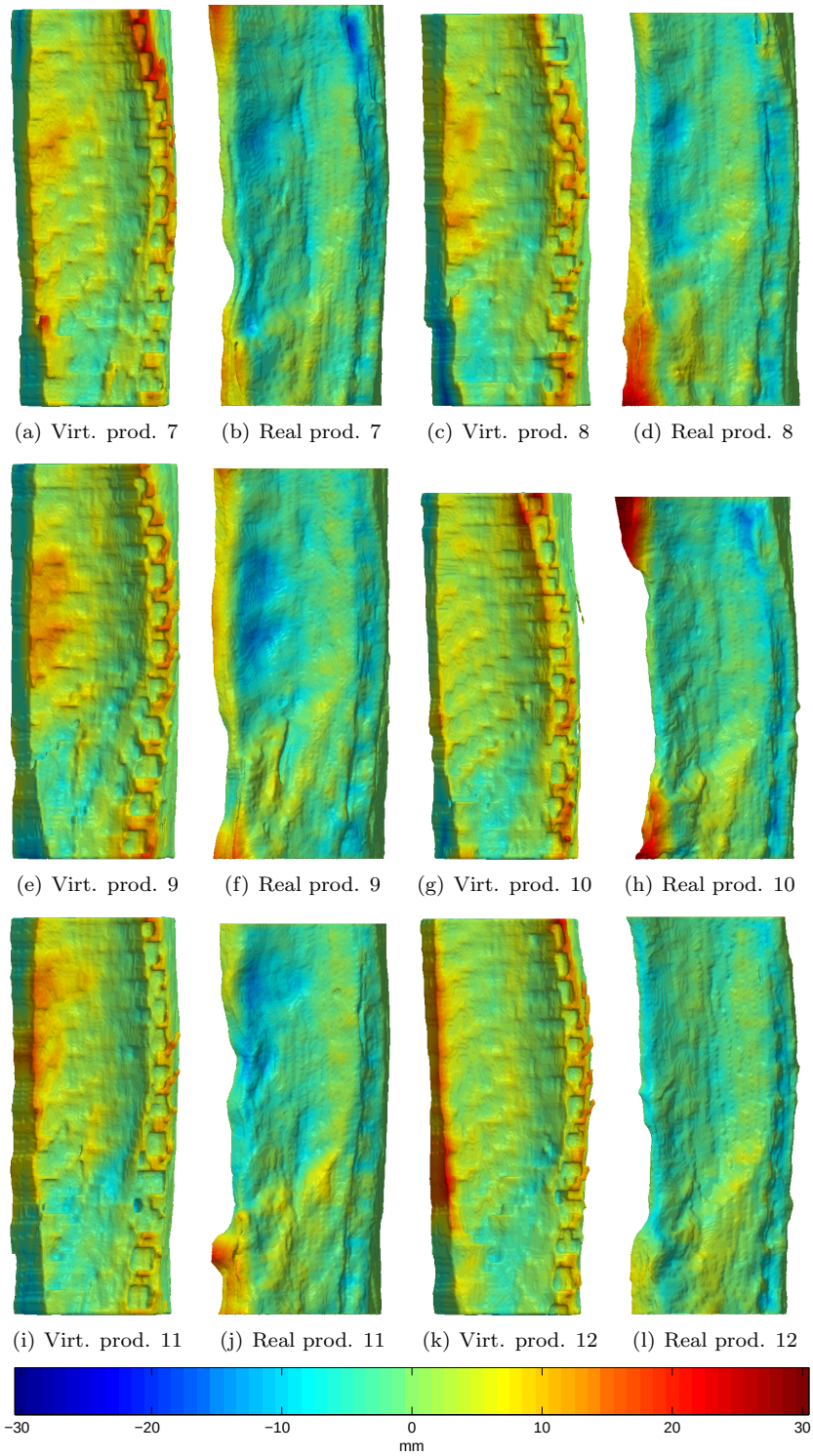

(a) Virt. prod. 7 (b) Real prod. 7 (c) Virt. prod. 8 (d) Real prod. 8

(e) Virt. prod. 9 (f) Real prod. 9 (g) Virt. prod. 10 (h) Real prod. 10

(i) Virt. prod. 11 (j) Real prod. 11 (k) Virt. prod. 12 (l) Real prod. 12

Figure 8.9: 3D Surface distance plots. Pigs 7-12

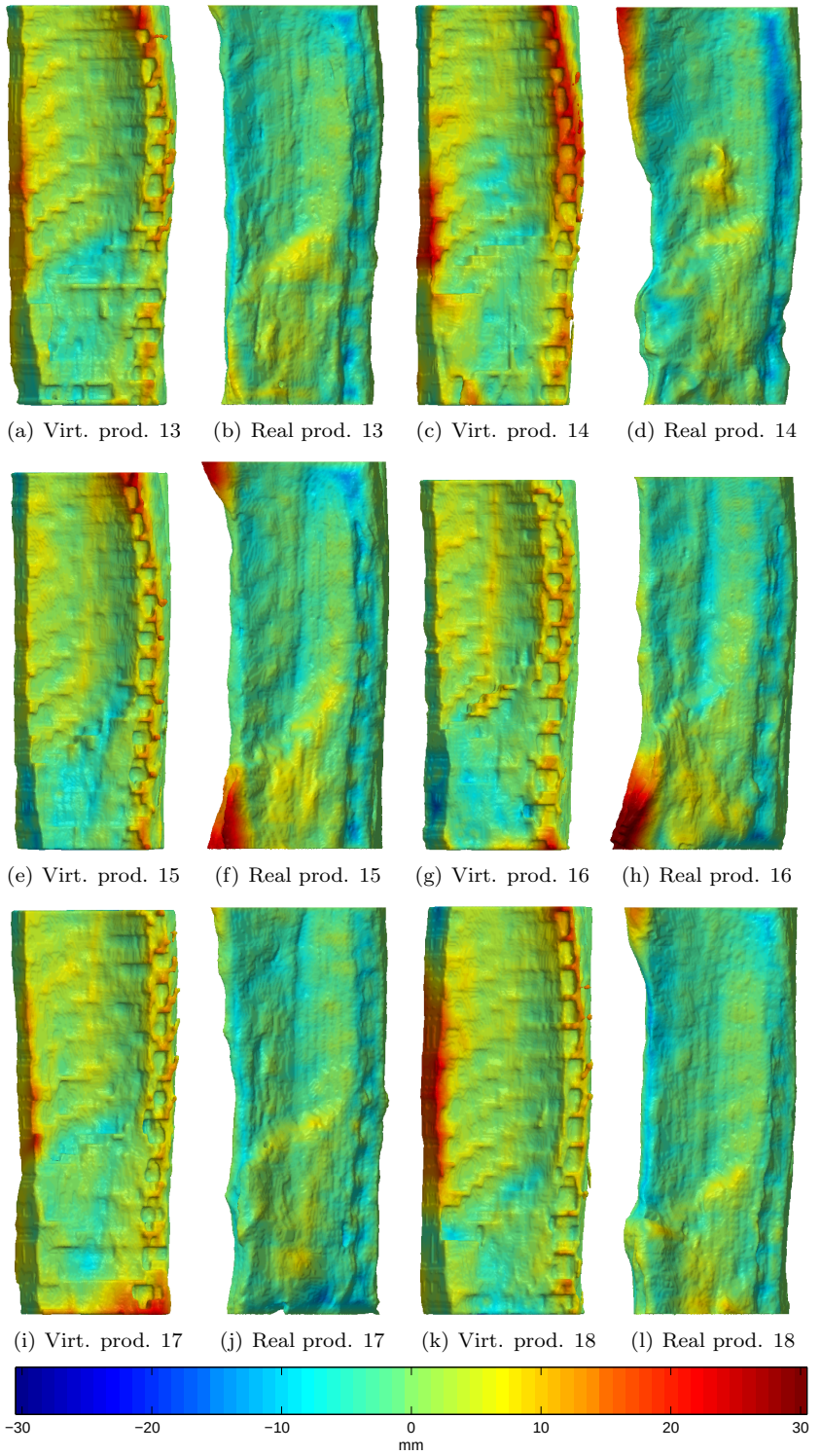

(a) Virt. prod. 13 (b) Real prod. 13 (c) Virt. prod. 14 (d) Real prod. 14

(e) Virt. prod. 15 (f) Real prod. 15 (g) Virt. prod. 16 (h) Real prod. 16

(i) Virt. prod. 17 (j) Real prod. 17 (k) Virt. prod. 18 (l) Real prod. 18

Figure 8.10: 3D Surface distance plots. Pigs 13-18.

- The low quality of the data questions the accuracy of the registration. Especially, the low out-plane resolution is a problem for intensity based image registration as the spatial image derivatives in the out-plane direction become significantly smaller than the in-plane derivatives. In addition, thin structures running parallel with the slice planes may fade out and almost disappear.

If these issues are addressed in the future, we believe that the presented methodology is appropriate for inspecting the consistency between virtual and real cuts.

Chapter 9

Surface-to-surface registration using level sets

Mads Fogtmann Hansen, Søren Erbou, Martin Vester-Christensen, Rasmus Larsen, Bjarne Ersbøll and Lars Bager Christensen

Abstract

This paper presents a general approach for surface-to-surface registration (S2SR) with the Euclidean metric using signed distance maps. In addition, the method is symmetric such that the registration of a shape A to a shape B is identical to the registration of the shape B to the shape A.
The S2SR problem can be approximated by the image registration (IR) problem of the signed distance maps (SDMs) of the surfaces confined to some narrow band. By shrinking the narrow bands around the zero level sets the solution to the IR problem converges towards the S2SR problem. It is our hypothesis that this approach is more robust and less prone to fall into local minima than ordinary surface-to-surface registration. The IR problem is solved using the inverse compositional algorithm.
In this paper, a set of 40 pelvic bones of Duroc pigs are registered to each other w.r.t. the Euclidean transformation with both the S2SR approach and iterative closest point approach, and the results are compared.

9.1 Introduction

This paper addresses the problem of shape registration or alignment which plays an essential role in shape analysis. Many registration procedures such as generalized Procrustes analysis [51, 67] rely on a prior manual annotation of landmarks.

The main drawback with these approaches is the reliance on manual annotation which becomes cumbersome and infeasible for larger 2Ddatasets and for 3D data.
Methods for explicitly deriving landmarks form training curves/surfaces based on information theoretic theory has been published [46]. Unfortunately these often suffer form exceeding use of computation time.
The iterative closest point (ICP) algorithm by Besl et al. [17] solves the problem of landmark dependence by iteratively updating the point correspondence after the closest point criterium. Since the introduction in 1992 many extensions and improvements of original ICP have been proposed in literature [57, 68, 136]. Most of these methods still require a good initial estimate in order not to converge to a local minimum. Furthermore, common for these methods are that they do not utilize the knowledge of the connectedness of the point cloud, which is available in many cases.
The approach described in this paper is in many ways related to the approach presented by Darkner et al. [45], which aligns two point clouds by minimizing the sum of squared difference between the distance functions of the point clouds in some rectangular box domain. The problem with the scheme by Darkner et al. is that it is likely produce a suboptimal result when applied to concave shapes. That is, the concave parts of a shape will not propagate as far out in a distance map as the convex parts. As a consequence points placed on the convex parts of a shape are given more weight than points on concave parts. Our approach differs from the approach presented in [45], as it uses *signed* distance maps and minimizes the squared difference between the signed distance maps restricted to a shrinking narrow band. Thus, it does not suffer from the same defect as [45].

9.2 Theory

The registration of a surface S_x to a surface S_y w.r.t the Euclidean metric can be expressed as the minimization of the functional

$$F_1(\boldsymbol{p}) = \oint_{\mathcal{S}_x} d(W(\boldsymbol{x};\boldsymbol{p}), \mathcal{S}_y)^2 d\boldsymbol{x}, \tag{9.1}$$

where $W(\_;\boldsymbol{p})$ is the warp function.
A minor flaw with this approach is that the registration of S_x to S_y is not necessarily equivalent to the registration S_y to S_x. If $W(\_;\boldsymbol{p})$ is invertible (9.1)

can be extended to

$$\begin{aligned} F_2(\boldsymbol{p}) &= \oint_{\mathcal{S}_x} d(W(\boldsymbol{x};\boldsymbol{p}),\mathcal{S}_y)^2 d\boldsymbol{x} + \oint_{\mathcal{S}_y} d(W(\boldsymbol{y};\boldsymbol{p})^{-1},\mathcal{S}_x)^2 d\boldsymbol{y} \\ &= \oint_{\mathcal{S}_x} d_{,\mathcal{S}_y}(W(\boldsymbol{x};\boldsymbol{p}))^2 d\boldsymbol{x} + \oint_{\mathcal{S}_y} d_{\mathcal{S}_x}(W(\boldsymbol{y};\boldsymbol{p})^{-1})^2 d\boldsymbol{y}, \end{aligned} \tag{9.2}$$

where $d_{\mathcal{S}_x}$ and $d_{\mathcal{S}_y}$ are the distance maps of the surfaces $\mathcal{S}_x$ and $\mathcal{S}_y$, respectively. This energy functional ensures a symmetric registration.
A minimum of F_2 can be obtained by any gradient or Newton based optimization scheme. However, such schemes may very well get stuck in a local minimum instead of the global minimum. To overcome this problem we introduce a slightly different energy functional

$$F_3(\boldsymbol{p}) = \int_{U_x^r} (\Phi_y(W(\boldsymbol{x};\boldsymbol{p})) - \Phi_x(x))^2 d\boldsymbol{x} + \int_{U_y^r} (\Phi_x(W(\boldsymbol{y};\boldsymbol{p})^{-1}) - \Phi_y(y))^2 d\boldsymbol{y}, \tag{9.3}$$

where $\Phi_x(\boldsymbol{x})$ and $\Phi_y(\boldsymbol{y})$ are the signed distance maps (SDMs) of the surfaces $\mathcal{S}_x$ and $\mathcal{S}_y$, and $U^r = \{\boldsymbol{x} \mid \boldsymbol{x} \in \mathbb{R}^d, |\Phi(x)| < r\}$. And we note that

$$F_3 \to F_2 \text{ for } r \to 0. \tag{9.4}$$

Now, consider the shape in Figure 9.1(a) consisting of two identical rectangles. If we translate the shape in both the x and the y direction between -25 and 25 pixels and calculate the energy in each position using F_2 and F_3 with $r = 25$ pixels, we get energy landscapes shown in Figure 9.1(b,c). In this case, the F_2 cost function produces three minima while the F_3 cost function produces only the global minimum.

9.3 Method

The energy functional defined in F_3 can be viewed as an image registration problem between two SDMs Φ_x and Φ_y, where the points to be warped are those inside the narrow bands U_x^r and U_y^r. The problem is solved using an extended version of the inverse compositional algorithm presented by Baker et al [16]. To preserve the same notation as in [16], we assume that Φ_x and Φ_y are discretized SDMs. Thus, F_3 becomes

$$F_4(\boldsymbol{p}) = \sum_{\boldsymbol{x} \in U_x^r} (\Phi_y(W(\boldsymbol{x};\boldsymbol{p})) - \Phi_x(\boldsymbol{x}))^2 + \sum_{\boldsymbol{y} \in U_y^r} (\Phi_x(W(\boldsymbol{y};\boldsymbol{p})^{-1}) - \Phi_y(\boldsymbol{y}))^2. \tag{9.5}$$

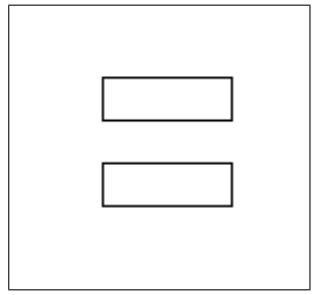

(a) A simple shape.

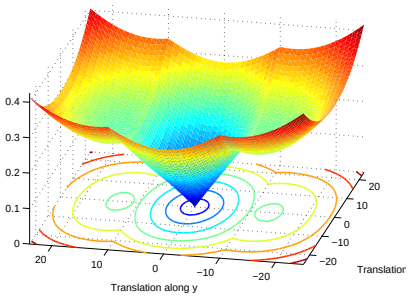

(b) F_2 cost functional.

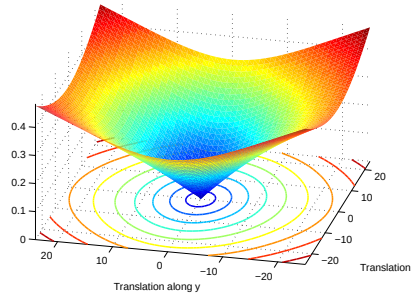

(c) F_3 cost functional.

Figure 9.1: Cost as a function of translation in x and y direction.

If the set of warps forms a *group* the minimization of F_4 is equivalent to the minimization of

$$\begin{aligned} F_5(\boldsymbol{p}) &= \sum_{\boldsymbol{x}\in U_x^r} (\Phi_y(W(\boldsymbol{x};\boldsymbol{p})) - \Phi_x(W(\boldsymbol{x};\Delta\boldsymbol{p})))^2 \\ &+ \sum_{\boldsymbol{y}\in U_y^r} (\Phi_x(W(\boldsymbol{y};\boldsymbol{p})^{-1}) - \Phi_y(W(\boldsymbol{y};\Delta\boldsymbol{p})^{-1}))^2. \end{aligned} \tag{9.6}$$

with the update rule $W(\boldsymbol{x};\boldsymbol{p}) \leftarrow W(\boldsymbol{x};\boldsymbol{p}) \circ W(\boldsymbol{x};\Delta\boldsymbol{p})^{-1}$. By applying the first order Taylor expansion to (9.6) we get

$$\begin{aligned} F_5(\boldsymbol{p}) &\approx \sum_{\boldsymbol{x}\in U_x^r} \left(\Phi_y(W(\boldsymbol{x};\boldsymbol{p})) - \Phi_x(W(\boldsymbol{x};\boldsymbol{0})) - \nabla\Phi_x \frac{\partial W(\boldsymbol{x};\boldsymbol{0})}{\partial \boldsymbol{p}} \Delta\boldsymbol{p}\right)^2 \\ &+ \sum_{\boldsymbol{y}\in U_y^r} \left(\Phi_x(W(\boldsymbol{y};\boldsymbol{p})^{-1}) - \Phi_y(W(\boldsymbol{y};\boldsymbol{0})^{-1}) - \nabla\Phi_y \frac{\partial W(\boldsymbol{y};\boldsymbol{0})^{-1}}{\partial \boldsymbol{p}} \Delta\boldsymbol{p}\right)^2 \end{aligned} \tag{9.7}$$

By taking the derivatives of F_5 w.r.t. $\Delta\boldsymbol{p}$ and setting them equal to zero we get the update equation

$$\Delta\boldsymbol{p} = -\boldsymbol{H}^{-1} \left(\sum_{\boldsymbol{x}\in U_x^r} \boldsymbol{S}_x^\top \boldsymbol{E}_{\boldsymbol{x}} + \sum_{\boldsymbol{y}\in U_y^r} \boldsymbol{S}_y^\top E_y \right), \tag{9.8}$$

where $\boldsymbol{S}_x = \nabla\Phi_x \frac{\partial W(\boldsymbol{x};\boldsymbol{0})}{\partial \boldsymbol{p}}$, $\boldsymbol{S}_y = \nabla\Phi_y \frac{\partial W(\boldsymbol{y};\boldsymbol{0})^{-1}}{\partial \boldsymbol{p}}$, $E_x = \Phi_y(W(\boldsymbol{x};\boldsymbol{p})) - \Phi_x(\boldsymbol{x})$, $E_y = \Phi_x(W(\boldsymbol{y};\boldsymbol{p})^{-1}) - \Phi_y(\boldsymbol{y})$ and $\boldsymbol{H} = \sum_{\boldsymbol{x}\in U_x^r} \boldsymbol{S}_x^\top \boldsymbol{S}_x + \sum_{\boldsymbol{y}\in U_y^r} \boldsymbol{S}_y^\top \boldsymbol{S}_y$. Note that $\boldsymbol{H}^{-1}$, $\boldsymbol{S}_x$ and $\boldsymbol{S}_y$ only have to be computed once. A S2SR can be obtained with Algorithm 1.

Algorithm 9.1 S2SR

```
r = [r_1 ... r_n]; { r_i > r_{i+1} }
for each r_i ∈ r do
    k = 0;
    repeat
        update p using (9.8) with U_x^{r_i} and U_y^{r_i};
        k = k + 1;
    until convergence or k > k_max
end for
```

The best sequence of r_i's is properly highly depended on the problem. We have applied the following scheme with success:

$$r_{i+1} \approx \frac{r_i}{2}. \tag{9.9}$$

Selecting a suitable initial narrow band r_0 is however not entirely straight forward. If the choice of r_0 is too small the algorithm may get stuck in a local minima, and if it is too large the algorithm will use an unnecessary amount of computational power. Note, that the computation time is much more depended on the radius of the initial narrow band than the number of narrow bands as the global minimum of F_3 for the narrow band r_i properly is relatively close to the global minimum of F_3 for r_{i+1}. In general, r_0 should be larger than the width of largest structure or feature in the image which might introduce a local minimum in F_3.

9.3.1 Extending approach to open surfaces

SDMs are in principal only defined for closed surfaces as it is impossible to label the inside and outside of an open surface. Thus, our approach can only be applied to closed surfaces. To overcome this problem we introduce the notion of a pseudo SDM.
The pseudo SDM of triangle mesh of an open surface is computed using the following recipe:

1. Close the surface by triangulating all the holes in the triangle mesh.
2. Compute the SDM of the closed tiangle mesh. Bærentzen et al. [11, 12] describe how to compute the SDM of a closed triangle mesh.
3. Set all voxels in the discretized SDMs with distances to the added faces to an undefined value.

Under the registration, voxels from one SDM may be warped to an undefined volume of the other SDM. In such cases, it is reasonable to assume that the distance in the undefined volume is 0, as we have no way of knowing whether the point is on the outside or inside of the shape. This hack allows for a bit of slack around the open areas of a surface. In many cases a surface is only open as it has been chosen to disregard a part of the shape - cutting away part of a shape in the exact *same place* is impossible. Furthermore, the gradient of a SDM at the borders between the defined and undefined volumes is likewise assumed to be equal to 0.

Sometimes, it is impossible to close an open surface with triangulation without introducing intersections between the new faces and the existing faces. Also, it might not be reasonable to close a surface if the hole is very large. In such

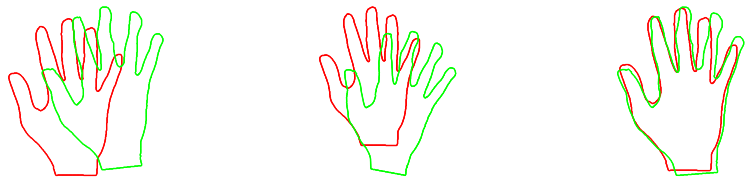

(a) Initial position. (b) Final position for S2SR with narrow band r=1. (c) Final position for S2SR with narrow bands 30, 15, 7.5, 1.

Figure 9.2: Rigid registration of left (green) and right hand (red).

cases, it might be more advisable simply to use unsigned distance maps instead of SDMs. The question of how large a hole in a surface can be, before the registration algorithm fails or produces suboptimal result with pseudo SDMs, needs to be investigated in the future.

9.4 Experiments

Two experiments were conducted to test the surface registration approach; (i) a toy example where the outline of the right and left hand of one of the authors were registered to each other, and (ii) a real example where 40 pelvic bones of Duroc pigs were registered with the ICP algorithm by Fitzgibbon [57] and with our S2SR algorithm.

9.4.1 Hand example

To test the robustness of the S2SR algorithm a left and a right hand were traced on a piece of paper and scanned into a computer. The left hand was flipped horizontally, displaced 100 pixels in the x-direction and -25 pixels in the y-direction, and rotated 5 degrees counter clockwise. Figure 9.2 shows the initial position of the hands, the final position with regular S2SR[1] and the final position with our S2SR algorithm with the narrow bands $r = 30, 15, 7, 3, 1$. Evidently, the regular S2SR approach gets stuck in a local minimum or saddle point, while the shrinking narrow band S2SR approach registers the left and right hand perfectly.

[1]Simulated with the small narrow band r=1.

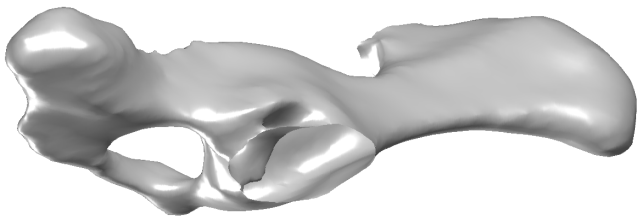

Figure 9.3: Example of a pelvic bone from a Duroc pig.

9.4.2 Pelvic bones

Half pig skeletons were automatic extracted from CT scans of half pig carcasses and fitted with implicit surfaces. From the implicit surfaces triangle meshes were created, and the pelvic bones were manually removed from the triangulated skeletons. An example of a pelvic bone can be found in Figure 9.3.

From the set of pelvic bone shapes a shape was selected to be the reference, and the remaining shapes were registered to the reference shape with ICP and our level set based S2SR algorithm with $r = 20,\ 10,\ 5,\ 2.5,\ 1\ mm$. To compare the two registration approaches we use the mean squared error (MSE) and the maximum error (ME). As ICP minimizes the point-to-closest-point (CP) distance and our algorithm minimizes the surface-to-surface distance[2], we evaluate the performance of the registration algorithms using both distance concepts. Furthermore, as our registration algorithm does symmetric minimization of the squared distances and ICP does not, the MSE and the ME are calculated in the same direction as the ICP registration, in the other direction and in both directions combined. The registration results for ICP and S2SR can be found in Table 9.1 and 9.2, respectively. As no surprise, the ICP registration has a lower MSE and ME in the same direction as the registration, when we are using the CP distance. It is neither a surprise that our S2SR algorithm has lower MSEs and MEs in the opposite direction of the ICP registration and in both directions. It is however a bit of a surprise, that our S2SR algorithm has a smaller MSE than ICP when using the SDMs to extract distances. A possible explanation for this result is that our algorithm allows for a bit of slack around the open regions of the surface and is therefore better at fitting the remaining

[2]The distances are found by interpolating the SDMs. To ensure fairness, when evaluating the MSE and ME, points, which are warped to an undefined area of a SDM, are ignored instead of receiving the distance 0.

Method	ICP ($A \rightarrow B$)					
Direction	$A \rightarrow B$		$A \leftarrow B$		$A \leftrightarrow B$	
Measure	$\sqrt{MSE}$	ME	$\sqrt{MSE}$	ME	$\sqrt{MSE}$	ME
SDM	11.92	20.13	12.70	27.04	12.34	27.24
CP	12.32	20.85	14.40	29.41	13.44	29.48

Table 9.1: The MSE and ME averaged over the 39 registrations after ICP registration.

Method	S2SR ($A \leftrightarrow B$)					
Direction	$A \rightarrow B$		$A \leftarrow B$		$A \leftrightarrow B$	
Measure	$\sqrt{MSE}$	ME	$\sqrt{MSE}$	ME	$\sqrt{MSE}$	ME
SDM	11.69	24.11	12.18	24.03	11.90	26.28
CP	12.77	25.70	13.11	26.34	12.95	28.30

Table 9.2: The MSE and ME averaged over the 39 registrations after S2S registration.

regions of the surface. Figure 9.4 illustrates this by color-coding the surfaces of two registered pelvic bones with the shortest distance.

W.r.t. computation time, it can be mentioned that it took approximately 20 minutes to run the 39 registrations with ICP and approximately 50 minutes to run 39 registrations with S2SR on a standard Dell laptop with a 1.6Ghz Centrino CPU and 2Gb ram. It is difficult to compare the computation time of the two algorithm as the computation time for the S2SR algorithm is vastly depended on the chosen parameters, e.g. the chosen narrow bands and the resolution of the discretized SDMs.

9.5 Conclusion

This paper has presented a method for S2SR. The registration algorithm was tested on two examples, where its properties were highlighted; (i) it is less prone to fall into local minima than ordinary S2SR, (ii) and it does symmetric registration. As the method relies on SDMs it only works in theory on closed surfaces. Nevertheless, this paper has demonstrated that it can work on open surfaces by introducing a pseudo SDM, where distances are not defined in volumes *close* to the open regions of the surface.
In the future, we will use non-rigid transformations with the registration approach.

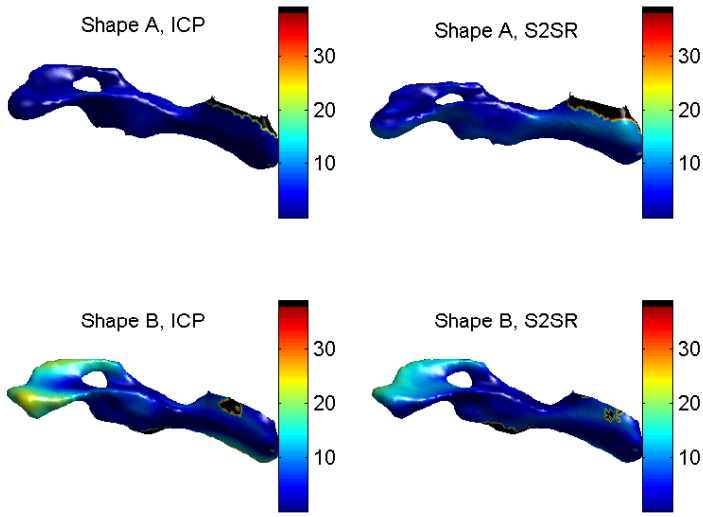

Figure 9.4: Distance color-coded surfaces after registration. Black areas are areas where the distance could not be interpolated in the SDM because the point is situated in a undefined area.

Chapter 10

Diffeomorphic Statistical Deformation Models

Michael S. Hansen, Mads F. Hansen and Rasmus Larsen

Abstract

In this paper we present a new method for constructing diffeomorphic statistical deformation models in arbitrary dimensional images with a nonlinear generative model and a linear parameter space.

Our deformation model is a modified version of the diffeomorphic model by Cootes et al. The modifications ensure that no boundary restriction has to be enforced on the parameter space to prevent folds or tears in the deformation field.

For straightforward statistical analysis, principal component analysis and sparse methods, we assume that the parameters for a class of deformations lie on a linear manifold and that the distance between two deformations is given by the metric introduced by the L_2-norm in the parameter space. The chosen L_2-norm is shown to have a clear and intuitive interpretation on the usual nonlinear manifold.

Our model is validated on a set of MR images of corpus callosum with ground truth in form of manual expert annotations.

We anticipate applications in unconstrained diffeomorphic synthesis of images, e.g. for tracking, segmentation, registration or classification purposes.

10.1 Introduction

Registration is the problem of establishing correspondence between points in different images. It has been used for building models of variation in groups of

images for several years. Cootes et al. proposed the very successful active appearance models in 1998 [35], which, once trained, can establish correspondence between points in the model and the images using a piecewise affine mapping. Rueckert et al. presented a statistical deformation model based on registrations of an atlas to the images of the group [133]. Joshi et al. demonstrate how to construct an unbiased atlas from a population [82], and Cootes et al. presented a guaranteed diffeomorphic shape model [37] by using smooth kernels for interpolating a warp field and putting restrictions on the variation of the parameters. Vester-Christensen et al. have presented an accelerated version of this algorithm [166], which is based on the inverse compositional method by Baker et al., which we have also made extensive use of in the presented work [16].

10.2 Methods

We define image registration as the identification of correspondence between positions in images. In the current work we address problems where the correspondences can be represented by a diffeomorphic function $f \in \mathcal{H}$, where $\mathcal{H}$ denotes the infinite dimensional group of diffeomorphisms on $\mathbb{R}^N$. The mapping from one image to the other is differentiable and the inverse exists and is also differentiable. Popularly speaking this limits the problem of registration to the problem of finding smooth warps without folds or tears. More precisely this is fulfilled, when the Jacobian of the warp field is positive and well defined.

In the statistical analysis of the warp functions we are interested in estimating an unbiased atlas of the structures we are registering. We identify such an atlas as the groupwise maximizer of similarity between the atlas R and the deformed images I_i, while minimizing the deformation fields ϕ_i.

$$[\phi_i,\ \hat{R}] = \min_{\phi_i, \hat{R}} \sum_i \mathcal{S}[\hat{R}, I_i \circ \phi_i] + \alpha \mathcal{D}(\phi_i)^2 \ . \tag{10.1}$$

where $\mathcal{S}$ denotes the similarity measure and $\mathcal{D}(\phi)$ denotes the regularization term, introduced to regularize the warp ϕ further than just restricting it to the space of the parameters, and α is the regularization parameter.

10.2.1 Parameterized diffeomorphisms

Fletcher et al. have investigated geodetic curves on the nonlinear manifolds of the parameters of the M-reps parameterization [58]. Most of the current statistical analysis, however, is based on the assumption that the data are located on

a linear manifold with the Euclidean metric, e.g. principal component analysis (PCA) and independent component analysis (ICA), which have nice properties as analytical tools. This is our motivation for introducing a function $\mathcal{G}$ which identifies $\mathbb{R}^M$ with a (hopefully interesting) subset of diffeomorphisms.

Let $\mathcal{H}(\mathbb{R}^N)$ denote the set of diffeomorphisms ($f : \mathbb{R}^N \to \mathbb{R}^N$). Now let $\mathcal{G}$ be a bijective mapping:

$$\mathcal{G} : \mathbb{R}^M \to \mathcal{H}_t \ . \tag{10.2}$$

where $\mathcal{H}_t = \mathcal{G}(\mathbb{R}^M) \subset \mathcal{H}$. We let $\mathcal{H}_t$ inherit the Euclidean metric from the parameter space $\mathbb{R}^M$

$$\begin{aligned} d(\mathcal{G}(t_1), \mathcal{G}(t_2)) \equiv d(t_1, t_2) = \|t_1 - t_2\|_2 \ \ , \\ t_1, t_2 \in \mathbb{R}^M \text{ and } \mathcal{G}(t_1), \mathcal{G}(t_2) \in \mathcal{H}_t \ , \end{aligned} \tag{10.3}$$

from which we conclude that $\mathcal{G}$ is a homeomorphism, and that the spaces $\mathcal{H}_t = \mathcal{G}(\mathbb{R}^M)$ and $\mathbb{R}^M$ are topologically equivalent. To conclude it can be observed that the defined metric on the space of parameterized warps is the L_2 norm on $\mathbb{R}^M$ as intended.

10.2.1.1 Composition of warps

The composition of more diffeomorphisms is diffeomorphic, which is a very important property of diffeomorphisms in the present context.

$$\begin{aligned} f_i \in \mathcal{H} \ , \ i \in \{1, 2, \ldots, n\} \\ \phi = f_n \circ f_{n-1} \circ \ldots \circ f_1 \ \Rightarrow \ \phi \in \mathcal{H} \end{aligned} \tag{10.4}$$

This allows for the construction of diffeomorphisms of higher complexity by the composition of several simpler warps. We shall assume we are dealing with parameterized warp functions, and our statistical analysis of warps can be reduced to the analysis of the warp parameters, in line with (10.3). For all images in our set the warp parameters shall warp from our *reference*, R, into the current *target*, I. In order to be able to compare parameters from different warp compositions it is evident that all our parameters exist in the same space. This is achieved by ensuring that all warps f_i in a composition warp from the reference coordinate system[37].

10.2.1.2 Grid based diffeomorphisms

Several grid based representations of diffeomorphisms have been presented and they are commonly used at different levels of detail and composed succeedingly

[37, 108, 133]. A general trait of the grid methods is that they manipulate the parameters of the functions describing the diffeomorphism, and that the functions have a local support in the image, either as points defined in the image or as basis functions with support around a control point. Often this parameterization of the grid is linear in the parameters and this obviously imposes some restrictions on the parameters to produce diffeomorphic warps. Cootes et al. specify a cut-off at displacements larger than $\frac{1}{\pi}$ of the cosine based kernel [37] and Lee et al. find a threshold bound on the B-spline parameters to secure that the B-spline based warp function is diffeomorphic [94].

10.2.1.3 A proposed $\mathcal{G}$

Let $\mathcal{F}$ be the function mapping from a real parameter space $\mathbb{R}^M$ into the space of functions from $\mathbb{R}^N$ to $\mathbb{R}^N$, e.g. in case of the B-spline warps, $\mathcal{F}$ maps from the parameter space into the space of N-dimensional B-spline functions $f : \mathbb{R}^N$ to $\mathbb{R}^N$, the image of $\mathcal{F}$, $\mathcal{K}$ can be shown to contain functions that are not diffeomorphic.

As discussed in the previous section there can for some parameterized warps be specified a threshold such that $\mathcal{P} =]-\tau_1, \tau_1[\times \cdots \times]-\tau_M, \tau_M[$ and $\mathcal{F} : \mathcal{P} \to \mathcal{H}_t$, where $\mathcal{H}_t \equiv \mathcal{F}(\mathcal{P}) \subset \mathcal{H}$. In the current study we have investigated the use of a function $g : \mathbb{R}^M \to \mathcal{P}$, that is, a bounded monotonic injective function into the space of thresholded displacement parameters. Constructing $\mathcal{G} = \mathcal{F} \circ g$, where $\mathcal{G} : \mathbb{R}^M \to \mathcal{H}_t$ gives us the desired function $\mathcal{G}$, namely a homeomorphic mapping from the parameter space $\mathbb{R}^M$ into the space of diffeomorphisms. As an example of the function g we have chosen a set of hyperbolic tangent function, because the range where it is close to linear is large. In this the composed mapping $\mathcal{G}$ and the different ranges are illustrated in Figure 10.1.

We define g coordinate-wise by

$$\boldsymbol{g} = \{g_1, ..., g_M\} \text{ where } g_i : R \to]-\tau_i, \tau_i[$$

$$s_i = g_i(t_i) = \tau_i \tanh a_i t_i \text{ , for } \quad i \in \{1, ..., M\} \tag{10.5}$$

where τ_i are the threshold parameters reducing the displacement parameter space of the warp to $\mathcal{P} \subset \mathbb{R}^M$, $\boldsymbol{s} = \{s_1, ..., s_M\} \in \mathcal{P}$ are the displacement parameters and a_i are constants ensuring that the impact of each t_i is of the same order of magnitude.

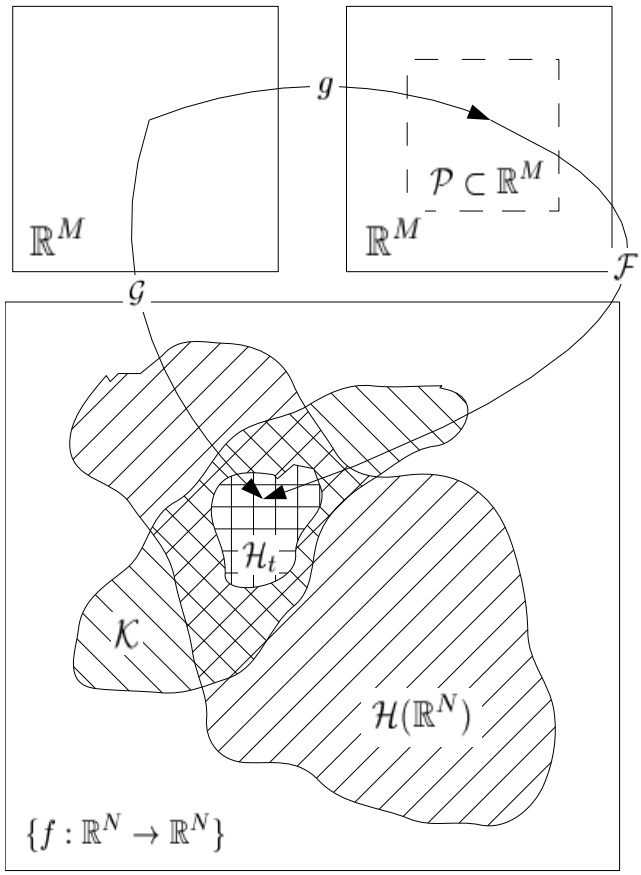

Figure 10.1: Illustration of the mapping $\mathcal{G}$ from $\mathbb{R}^N$ to $\mathcal{G}$, along with our proposed composed mapping $\mathcal{G} = \mathcal{F} \circ g$

.

10.2.1.4 Properties of the g mapping

Before we continue with an empirical validation of our proposed mapping we will make some theoretical considerations over the choice of homeomorphic mapping g. For small values $t \in \mathbb{R}^M$ the L_2 norm in $\mathbb{R}^M$ is equivalent to a scaled L_2 norm in $g(\mathbb{R}^M)$ to a first order. In other words, relating this to diffeomorphic warps, for small deformations the defined norm is equivalent to the usual metric applied in analysis of the warp fields [37, 133].

10.2.1.5 The parameter distribution

We believe that the distribution of the parameters is well described by the normal distribution and we will show what distribution this describes in the displacement parameter space of the warp function. Let f_{t_i} be the marginal distribution of the parameter t_i and f_{g_i} be the marginal distribution of the warp parameter $s_i = g_i(t_i)$, then

$$f_i(t_i) = \frac{1}{\sqrt{2\pi\sigma_i^2}} e^{-\frac{t_i^2}{2\sigma_i^2}} \tag{10.6}$$

$$f_{g_i}(s_i) = \frac{1}{2a_i \cdot \tau_i \sqrt{2\pi\sigma_i^2}} \left(e^{-\frac{g^{-1}(s_i)^2}{2\sigma_i^2}} + \frac{e^{\frac{\mu_i^2}{2\sigma_i^2}}}{2} e^{-\frac{(g^{-1}(s_i)-\mu_i)^2}{2\sigma_i^2}} + \frac{e^{\frac{\mu_i^2}{2\sigma_i^2}}}{2} e^{-\frac{(g^{-1}(s_i)+\mu_i)^2}{2\sigma_i^2}} \right) \tag{10.7}$$

where $\mu_i = \frac{\sigma_i^2 a_i}{2}$ and this distribution is seen to be the composition of three Gaussian distributions scaled by g^{-1}. For small μ_i this is approaching the Gaussian distribution which is often the distribution for the warp parameters in the small deformation domain and for μ_i big the two μ_i displaced distributions dominate, and we observe a high concentration of parameters around the threshold τ_i. In the presence of strong deformations this also what we expect when imposing a threshold on the warp deformation parameters. Based on these considerations we expect an M-dimensional normal distribution of our parameters to be well suited for modelling the distributions of the observed deformations.

10.2.1.6 Statistical deformation model

In the previous section we argued that the expected distribution of warps could be modelled as an M-dimensional normal distribution. If this is the case PCA

is known to be the optimal choice of analysis tool for creating a compact model of the observations, and is therefore the method of choice in the current implementation.

10.3 Implementation

To validate our approach for construction of diffeomorphic deformation model we have adapted the grid based diffeomorphisms by Cootes [37] with our g mapping. These diffeomorphisms can be viewed as an extension to standard linear interpolation, where the interpolation coefficients are transformed by a suitable kernel $k(r)$ which ensures smoothness across the grid boundaries. The displacement of a 2D point $\boldsymbol{x} \in \mathbb{R}^2$ is given by

$$\begin{aligned} \boldsymbol{u}(\boldsymbol{x}, \boldsymbol{d}) &= \sum_{m=0}^{1} \sum_{n=0}^{1} k_n(v) k_m(w) \boldsymbol{d}_{i+n,j+m} \\ &= \sum_{m=0}^{1} \sum_{n=0}^{1} a_{i+m,j+n}(\boldsymbol{x}) \boldsymbol{d}_{i+n,j+m} \qquad (10.8) \\ &= \begin{bmatrix} \boldsymbol{a}(\boldsymbol{x})^\top & \mathbf{0} \\ \mathbf{0} & \boldsymbol{a}(\boldsymbol{x})^\top \end{bmatrix} \boldsymbol{d} \qquad (10.9) \end{aligned}$$

where $k_0(r) = k(r)$, $k_1(r) = 1 - k(r)$, i and j are the local indices of the neighboring grid points, v and w are relative positions of $\boldsymbol{x}$ in the neighborhood and $\boldsymbol{d}$ and $\boldsymbol{d}_{i,j}$ are all the displacements and the displacement of the (i, j)-node, respectively. By substituting the displacements $\boldsymbol{d}$ with the g mapping with a suitable threshold τ, this deformation model will no longer be able to generate non-diffeomorphisms. In the present example we are using the Cootes kernel, $\tau = 1/\pi$.

For notational simplicity the displacement in the ith direction will represented by

$$u_i(\boldsymbol{x}, \boldsymbol{t}_i) = \boldsymbol{a}(\boldsymbol{x})^\top \boldsymbol{g}_\tau(\boldsymbol{t}_i), \qquad (10.10)$$

and the warp function is written in the form

$$\boldsymbol{\varphi}(\boldsymbol{x}, \boldsymbol{t}) = \boldsymbol{x} + \boldsymbol{u}(\boldsymbol{x}, \boldsymbol{t}). \qquad (10.11)$$

10.3.1 Image registration

To drive the registration between a reference image R and a target image I we apply the sum-of-squared-differences (SSD) as our similarity measure and the

regularization term is given by $\mathcal{D}(\phi) = d(e, \phi) = \|t\|_2$, where e is the identity map corresponding to $\boldsymbol{t} = 0$. The SSD comparison leads us to calculate the reference image as the arithmetic mean of the warped target images, as this is the optimum SSD solution to (10.1) [82].

$$F(\boldsymbol{t}) = \frac{1}{2}\sum_{\boldsymbol{x}}(R(\boldsymbol{x}) - I(\boldsymbol{\varphi}(\boldsymbol{x}, \boldsymbol{t}))^2 + \alpha\|\boldsymbol{t}\|_2^2 \tag{10.12}$$

$$= \frac{1}{2}\sum_{\boldsymbol{x}} E^2(\boldsymbol{x}, \boldsymbol{t}) + \alpha\|\boldsymbol{t}\|_2^2. \tag{10.13}$$

To achieve a fast optimization we apply the inverse compositional optimization approach by Baker et al. [16] to the cost function. Thus, we obtain a minimum by iteratively minimizing

$$F_{ic}(\boldsymbol{t}) = \frac{1}{2}\sum_{\boldsymbol{x}}(R(\boldsymbol{\varphi}(\boldsymbol{x}, \Delta\boldsymbol{t})) - I(\boldsymbol{\varphi}(\boldsymbol{x}, \boldsymbol{t}))^2 + \alpha\|\boldsymbol{t} - \frac{\partial \boldsymbol{t}'}{\partial \Delta \boldsymbol{t}}\Delta\boldsymbol{t}\|^2 \tag{10.14}$$

with respect to $\Delta\boldsymbol{t}$ and updating $\boldsymbol{t}$ according to

$$\boldsymbol{\varphi}(\boldsymbol{x}, \boldsymbol{t}') \leftarrow \boldsymbol{\varphi}(\boldsymbol{x}, \boldsymbol{t}) \circ \boldsymbol{\varphi}^{-1}(\boldsymbol{x}, \Delta\boldsymbol{t}). \tag{10.15}$$

In Appendix 10.b it is shown how $\boldsymbol{t}'$ is derived from (10.15).

By performing a first-order Taylor-expansion on $R(\boldsymbol{\varphi}(\boldsymbol{x}, \Delta\boldsymbol{t})$ around $\boldsymbol{x}$ in (10.14), taking the derivatives wrt. $\Delta\boldsymbol{t}$ and setting them equal to zero we get

$$\Delta\boldsymbol{t} = \boldsymbol{H}^-1\left[\sum_{\boldsymbol{x}} \boldsymbol{SD}(\boldsymbol{x})^\top E(\boldsymbol{x}, \boldsymbol{t}) + \alpha\frac{\partial \boldsymbol{t}'}{\partial \Delta \boldsymbol{t}}^\top \boldsymbol{t}\right] \tag{10.16}$$

where

$$\boldsymbol{SD}(\boldsymbol{x}) = \nabla R(\boldsymbol{x})\frac{\partial \boldsymbol{\varphi}(\boldsymbol{x}, \boldsymbol{0})}{\partial \boldsymbol{t}} \tag{10.17}$$

and

$$\boldsymbol{H} = \sum_{\boldsymbol{x}} \boldsymbol{SD}(\boldsymbol{x})^\top \boldsymbol{SD}(\boldsymbol{x}) + \alpha\left[\frac{\partial \boldsymbol{t}'}{\partial \Delta \boldsymbol{t}}\right]^\top \left[\frac{\partial \boldsymbol{t}'}{\partial \Delta \boldsymbol{t}}\right]. \tag{10.18}$$

The advantage with this inverse compositional approach is that $\boldsymbol{SD}(\boldsymbol{x})$ can be pre-computed as it is not dependent on $\boldsymbol{t}$.

10.4 Validation: corpus callosum model

To demonstrate our approach we have created a deformation model of the Corpus Callosum from 62 two dimensional MR images of the mid-sagittal cross-section of the corpus callosum brain structure. This data set is part of the LADIS (Leukoaraiosis and DISability) study [119], a pan-European study involving 12 hospitals and more than 700 patients. Furthermore, each corpus callosum has manually been annotated with 72 landmarks by a clinician, which we will later use for validation.

Prior to the non-rigid registration a rigid registration was performed to filter out non-anatomical variation. This was achieved by performing Procrustes analysis on the sets of annotations. After the rigid registration an initial reference was created by computing a mean image of the rigidly registered images. All corpus callosum images were then non-rigidly registered to the reference, and a new reference was computed by averaging. This was done multiple times until the reference stabilized. For the non-rigid registration the cosine kernel $k(r) = 0.5(1 + cos(\pi r))$ was applied [37]. The non-rigid warps were modelled by composing three grid based diffeomorphisms in a fine-to-coarse manner. The dimensions of the applied grids were 5×4, 10×8 and 20×16. The non-rigid registrations were carried out in coarse to fine order. After each level φ_i of the warp was estimated the target image was updated by warping the target image back into the reference coordinate frame by $T_{n+1}(x) = T_n(\varphi(x))$. This was done to ensure that different parameters from different warps could be compared [37]. a_i of the g mapping was set proportional to the inverse of the squared grid node distance because the grid was 2 dimensional. The image registration was validated using the Dice measure, which is twice the intersecting area between the ground truth shape outline of the warped image and the outline of the reference shape divided by the total area inside the two outlines. The ground truth was obtained from the expert annotations. The Dice measure was 0.884 ± 0.048. In Fig. 10.2 we show an example of a typical registration of an image. In Fig. 10.3 the cumulative overlap of the aligned corpus callosum shapes before and after a rigid registration is illustrated, showing a clear improvement in correspondences between the shapes.

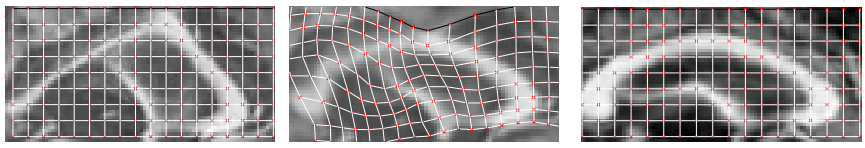

(a) Template image (b) Warped template (c) Reference image

Figure 10.2: Registration of an image to the reference.

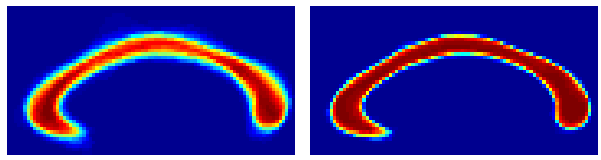

(a) Before nonrigid registration (b) After nonrigid registration

Figure 10.3: Cumulative overlap of the aligned corpus callosum shapes before and after a rigid registration

To create a compact deformation model, PCA was applied to the parameters after the groupwise registration of the images. 13 modes of variation could describe 95 % of the observed variation in the population as observed in Figure 10.4, and the first three modes are illustrated in Fig. 10.5. The first mode of variation is seen to be related to a vertical stretch and in particular to the size of the septum pellucidum (the dark area between the bright corpus callosum and the bright Fornix), the second mode is related to the kink of the corpus callosum and the thickness of the structure and the same goes for the third mode but with a different bending of the Fornix. Rueckert et al. have also analyzed the corpus callosum and they found modes quite similar to the ones found in the current study [133]. For comparison we applied a regularized version of Cootes' algorithm to the same problem, and constructed a similar PCA model of the variation. The variance of the modes is nearly identical, as shown in Figure 10.4 and the obtained Dice scores were also the same. However the described modes are not completely identical, and to point out the major difference, we note that the most extreme sites in the Cootes warp (in terms of curvature) are more expressed than the same sites in the model based on the current method.

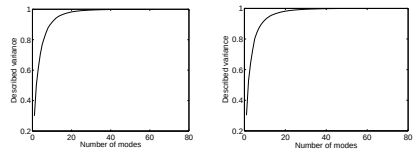

(a) (b)

Figure 10.4: Plot relating described variance with number of modes included in the model. a: the presented method. b: method introduced by Cootes et al. [37].

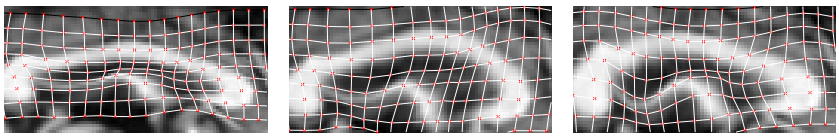

(a) 1st mode, −3 std. dev. (b) 2nd mode, −3 std. dev. (c) 3rd mode, −3 std. dev.

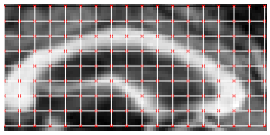

(d) Reference

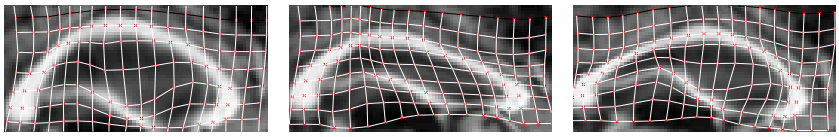

(e) 1 st mode, +3 std. dev. (f) 2nd mode, +3 std. dev. (g) 3rd mode, +3 std. dev.

Figure 10.5: First three modes of the corpus callosum deformation model estimated with the current method, shown as the reference warped ± 3 std. deviations.

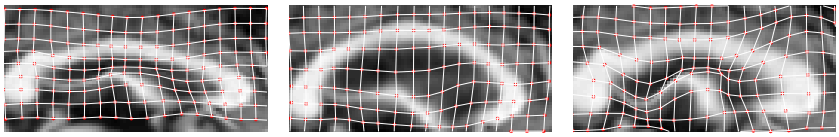

(a) 1st mode, −3 std. dev. (b) 2nd mode, −3 std. dev. (c) 3rd mode, −3 std. dev.

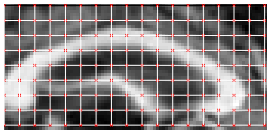

(d) Reference

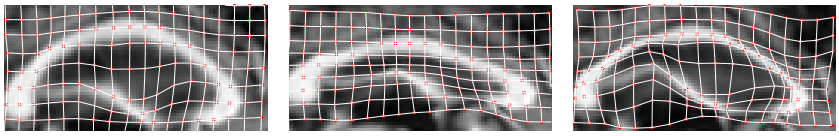

(e) 1 st mode, +3 std. dev. (f) 2nd mode, +3 std. dev. (g) 3rd mode, +3 std. dev.

Figure 10.6: First three modes of the corpus callosum deformation model estimated with a constrained version of Cootes' method, shown as the reference warped ± 3 std. deviations

10.5 Discussion

We have shown how a parametric function can be defined on the unbounded linear space $\mathbb{R}^M$ and still produce diffeomorphic warps. When this is accomplished by first mapping $\mathbb{R}^M$ into an open bounded subset of $\mathbb{R}^M$, which inevitably leads to an asymptotic behavior at the closure of the bounded set. In our implemented example the parameters of the model by Cootes et al. asymptotically approach $\frac{1}{\pi}$ where singularities in the warp *may* occur. We believe that our distance measure is very reasonable when we are indeed approaching a singularity, as a small change in the displacement parameters of the warp will cause a huge impact on curvature of the warp function. In Fig. 10.7 we show the Corpus Callosum which results from -6 std. deviations of the first mode. We see that a singularity starts to form in the contracting area but this is highly unlikely as predicted by our model and metric.

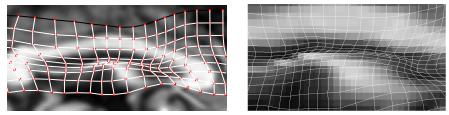

Figure 10.7: -6 Std. deviations of the first mode, normal view and a zoomed view on the beginning singularity.

With the choice of the tanh function, the asymptotic behavior is assumed to be exponential, which may not always be the case. There are obviously an infinite variety of monotonically bounded functions, e.g. the arcus tangent, and we will be investigating the choice of function in more detail.

A problem, we believe, that may occur with the proposed method is that we cannot be sure that the threshold does actually mark a singularity. A simple translation would for instance be asymptotic as well, which is why initial rigid alignment is very important indeed. Currently we investigate more involved parameter restrictions than the simple threshold to circumvent this possible problem.

Our validation on corpus callosum data showed that we were able to learn the important modes of variation, similar to previous obtained results, while the relatively high Dice coefficient illustrated that our warp representation was able to capture the large variations in the data set. We believe it is an advantage that all configurations in our parameter space are valid diffeomorphism, such that all gradients and derivatives during the optimization are well defined. Also we find it an advantage for tracking etc. that the the deformation as a function of the deformation model parameters is smooth, when using the presented method.

10.6 Conclusions

This paper proposed a new warp representation which allows statistical analysis on an unrestricted linear parameter space, where all derivatives are defined. Furthermore, we have shown that the L_2-norm in the parameter space introduces a reasonable metric in the actual space of modelled diffeomorphisms, and that our results compare well with those obtained using Cootes' deformation model.

Acknowledgements

The authors extend their gratitude to the LADIS work group for supplying the corpus callosum data. In particular we acknowledge the annotation effort of Charlotte Ryberg and Egill Rostrup from the Danish Research Center for Magnetic Resonance, Copenhagen University Hospital, Hvidovre, Denmark. We also wish to thank Vagn L. Hansen and Niels V. Christensen for fruitful discussion during this work.

10.a Warp inversion

Theorm 10.1 *Consider the function* $\boldsymbol{\varphi} : \mathbb{R}^N \times \mathbb{R}^M \mapsto \mathbb{R}^N$ *of type* $\boldsymbol{\varphi}(\boldsymbol{x}, \boldsymbol{t}) = \boldsymbol{x} + \boldsymbol{u}(\boldsymbol{x}, \boldsymbol{t})$ *and let* $\boldsymbol{\varphi_t}(\boldsymbol{x}) = \boldsymbol{\varphi}(\boldsymbol{x}, \boldsymbol{t})$ *be a* $\mathcal{C}^1$*-diffeomorphism. If* $\boldsymbol{u}(\boldsymbol{x}, \boldsymbol{0}) = \boldsymbol{0}$ *and* $\boldsymbol{u}(\boldsymbol{x}, \boldsymbol{t}) = -\boldsymbol{u}(\boldsymbol{x}, \boldsymbol{t})$*,* $\boldsymbol{\varphi}(\boldsymbol{x}, -\boldsymbol{t})$ *converges with second-order to* $\boldsymbol{\varphi}^{-1}(\boldsymbol{x}, \boldsymbol{t})$*.*

Proof.

$$
\begin{aligned}
& |\xi_i(h\boldsymbol{t})| = |\varphi_i(\boldsymbol{\varphi}(\boldsymbol{x}, h\boldsymbol{t}), -h\boldsymbol{t}) - x_i| \\
= \;& |x_i + u_i(\boldsymbol{x}, h\boldsymbol{t}) - u_i(\boldsymbol{x} + \boldsymbol{u}(\boldsymbol{x}, h\boldsymbol{t}), h\boldsymbol{t}) - x_i| \\
< \;& |u_i(\boldsymbol{x}, h\boldsymbol{t}) - u_i(\boldsymbol{x}, h\boldsymbol{t}) + \frac{\partial u_i}{\partial \boldsymbol{x}}(\boldsymbol{x}, h\boldsymbol{t})\boldsymbol{u}(\boldsymbol{x}, h\boldsymbol{t})| \\
< \;& |h\boldsymbol{t}^\top \frac{\partial^2 u_i}{\partial \boldsymbol{x} \partial h\boldsymbol{t}}(\boldsymbol{x}, \boldsymbol{0}) \frac{\partial \boldsymbol{u}}{\partial h\boldsymbol{t}}(\boldsymbol{x}, \boldsymbol{0}) h\boldsymbol{t}| \\
< \;& |c| \cdot |h^2| \qquad (10.19)
\end{aligned}
$$

10.b Derivation of update function

In general, it is unlikely that $\boldsymbol{\varphi}(\boldsymbol{x},\boldsymbol{t}) \circ \boldsymbol{\varphi}^{-1}(\boldsymbol{x},\Delta\boldsymbol{t})$ can be parameterized with $\boldsymbol{\varphi}(\boldsymbol{x},\boldsymbol{t}')$, and thus it has to be approximated.
In Appendix 10.a, it was shown that $\boldsymbol{\varphi}(\boldsymbol{x},-\boldsymbol{t})$ is a first-order approximation to $\boldsymbol{\varphi}^{-1}(\boldsymbol{x},\boldsymbol{t})$ as the error converges with second-order to zero. The composition in Eq. 10.15 is approximated with the parameters $\boldsymbol{t}'$ which minimizes the SSD between the true compositional warp and the warp $\boldsymbol{\varphi}(\boldsymbol{x},\boldsymbol{t}')$

$$\sum_x \Delta\boldsymbol{\varphi}(\boldsymbol{x})^\top \Delta\boldsymbol{\varphi}(\boldsymbol{x}) \tag{10.20}$$

where

$$\begin{aligned}\Delta\boldsymbol{\varphi}(\boldsymbol{x}) &= \boldsymbol{\varphi}(\boldsymbol{\varphi}(\boldsymbol{x},\Delta\boldsymbol{t}),\boldsymbol{t}) - \boldsymbol{\varphi}(\boldsymbol{x},\boldsymbol{t}') \\ &= \boldsymbol{a}(\boldsymbol{x})^\top(\boldsymbol{g}_\tau(\Delta\boldsymbol{t}) - \boldsymbol{g}_\tau(\boldsymbol{t}')) \\ &\quad + \boldsymbol{a}(\boldsymbol{\varphi}(\boldsymbol{x},\Delta\boldsymbol{t}))\boldsymbol{g}_\tau(\boldsymbol{t}).\end{aligned} \tag{10.21}$$

If

$$\boldsymbol{A} = \begin{bmatrix}\boldsymbol{a}(\boldsymbol{x_1})^\top \\ \vdots \\ \boldsymbol{a}(\boldsymbol{x_n})^\top\end{bmatrix}, \text{and } \boldsymbol{A}_\varphi = \begin{bmatrix}\boldsymbol{a}(\boldsymbol{\varphi}(\boldsymbol{x}_1,\Delta\boldsymbol{t})^\top \\ \vdots \\ \boldsymbol{a}(\boldsymbol{\varphi}(\boldsymbol{x}_n,\Delta\boldsymbol{t})^\top\end{bmatrix}$$

the updated warp parameters $\boldsymbol{t}'$ can be found by solving the system

$$\boldsymbol{0} = \boldsymbol{A}(\boldsymbol{g}_\tau(\Delta\boldsymbol{t}_i) - \boldsymbol{g}_\tau(\boldsymbol{t}_i')) + \boldsymbol{A}_\varphi\boldsymbol{g}_\tau(\boldsymbol{t}_i). \tag{10.22}$$

The least square solution to the system is

$$\boldsymbol{t}_i' = \boldsymbol{g}_\tau^{-1}\left(\boldsymbol{A}^\dagger\boldsymbol{A}_\varphi\boldsymbol{g}_\tau(\boldsymbol{t}_i) + \boldsymbol{g}_\tau(\Delta\boldsymbol{t}_i)\right) \tag{10.23}$$

where $\boldsymbol{A}^\dagger = \left[\boldsymbol{A}^\top\boldsymbol{A}\right]^{-1}\boldsymbol{A}^\top$.

As A_φ has to be evaluated on warped points it is relatively computational expensive to evaluate. Thus, we perform a first-order Taylor expansion on A_φ and arrive at

$$\boldsymbol{t}_i' = \boldsymbol{k}^{-1}\left(\boldsymbol{A}^\dagger\boldsymbol{A}_{J_i}\boldsymbol{A}\boldsymbol{g}_\tau(\Delta\boldsymbol{t}_i) + \boldsymbol{g}_\tau(\Delta\boldsymbol{t}_i) + \boldsymbol{g}_\tau(\boldsymbol{t}_i)\right), \tag{10.24}$$

where

$$A_{J_i} = \boldsymbol{I} + \operatorname{diag}\frac{\partial\boldsymbol{a}(\boldsymbol{x}_j)}{\partial x_i}^\top \boldsymbol{g}_\tau(\boldsymbol{t}_i)_{j=1\ldots n} \tag{10.25}$$

Chapter 11

Conditional Statistical Model Building

Mads Fogtmann Hansen, Michael Sass Hansen and Rasmus Larsen

Abstract

We present a new statistical deformation model suited for parameterized grids with different resolutions. Our method models the covariances between multiple grid levels explicitly, and allows for very efficient fitting of the model to data on multiple scales.

The model is validated on a data set consisting of 62 annotated MR images of Corpus Callosum. Five sixth of the data set was used as a training set. The images of the training set were non-rigidly registered to each other without a shape prior. From the non-rigidly registered training set a shape prior was constructed by performing principal component analysis on each grid level and using the results to construct a conditional shape model, conditioning the finer parameters with the parameters from the coarser grid levels. The remaining shapes were registered with the constructed shape prior. The dice measures for the registration without prior and the registration with a prior were 0.875 ± 0.042 and 0.8615 ± 0.051, respectively.

11.1 Introduction

Image registration has for many years been vastly explored by the imaging processing community. Especially in medical imaging, registration has proven a fundamental part of many medical application and studies; Cardenas et al. [26] and Rohlfing et al. [130] have studied the effect of alcohol consumption on

the human brain, Wierzbicki et al. [175] and Meinzer et al. [106] used image registration for surgery planning and Rousseau et al. [131] create high-resolution MR images of human fetal brains by registration of multiple sets of orthogonal fast two-dimensional MRI slices. Image registration seeks to find a *reasonable* geometrical deformation such that the dissimilarity between to images vanishes or becomes small. What is meant by *reasonable* is naturally dependent on the application. However, in medical applications the common consensus is that these deformations at least are diffeomorphic - smooth and invertible.

It is often favorable to parameterize the deformations as this allows the appliance of gradient based optimization approaches. Rueckert et al. [135] proposed the use of cubic B-splines basis functions on a regular lattice. In general these parameterizations ensure smoothness but not invertibility unless constraints are applied to parameters. Consequently, simple parametric representations such as the cubic B-splines by Rueckert [135] are not well suited for handling large deformations. Christensen et al. [32] introduced fluid registration which in contrast is capable of handling arbitrarily large deformations but sensitive to the initialization. Another approach is to compose several parametric warps together to construct a warp model capable of handling large and complex deformations. In this paper, we will model deformations by composing a sequence of grid based diffeomorphisms in a fine-to-coarse manor as described by Cootes et al. [37].

Furthermore, Cootes et al. [37] constructed a diffeomorphic statistical shape model by learning a linear model of the variation of the warp parameters from a set of non-rigidly registered images. Such models are however not well suited for searching images as the warps are compositions of several grid based diffeomorphism, and thus have complex derivatives. Instead, we propose a conditional deformation model that conditions the warp parameters of a level on the warp parameters of the coarser levels. This allows us to optimize the levels sequentially in a coarse-to-fine manner and provides a natural regularization. This approach is in many ways similar to the conditional shape model by Bruijne et al. [48] who condition the shape of a vertebra on the shapes of the neighboring vertebrae.

11.2 Methods

11.2.1 Bayesian formulation of the compositional image registration problem

We will pose the registration problem in a Bayesian setting, which in turn will allow for a more straightforward interpretation of the presented method. We identify an atlas by the reference, R, and the deformation fields $\boldsymbol{\phi}_i$ that maximize the posterior probability given a set of images I_i. The deformation field will be parameterized on different grid levels by $\boldsymbol{t} = \{\boldsymbol{t}^1, \boldsymbol{t}^2, ..., \boldsymbol{t}^m\}$. It is common to maximize the posterior probability $P(\boldsymbol{t}, R|I)$ by sequentially maximizing $P(\boldsymbol{t}^i, R|I, \{\boldsymbol{t}^1, ..., \boldsymbol{t}^{i-1}\})$, [37].

$$P(\boldsymbol{t}^i, R|I, \{\boldsymbol{t}^1, ..., \boldsymbol{t}^{i-1}\}) = \frac{P(I|\{\boldsymbol{t}^1, ..., \boldsymbol{t}^i\}, R)P(\boldsymbol{t}^i, R|\{\boldsymbol{t}^1, ..., \boldsymbol{t}^{i-1}\})}{P(I|\{\boldsymbol{t}^1, ..., \boldsymbol{t}^{i-1}\})} \tag{11.1}$$

It is reasonable to assume that the warp parameters and the reference are independent. We shall assume a Gaussian distribution of the parameters t^i, conditional on the previous parameters

$$P(\boldsymbol{t}^i|\{\boldsymbol{t}^1, ..., \boldsymbol{t}^{i-1}\}) = e^{-\gamma\|\boldsymbol{t}^i - \mu^i\|_{\Sigma_{i|\boldsymbol{t}^1,...,\boldsymbol{t}^{i-1}}}} \tag{11.2}$$

where the conditional mean μ^i and and covariance matrix $\Sigma_{i|\boldsymbol{t}^1,...,\boldsymbol{t}^{i-1}}$ are given in [1]

$$\Sigma = \begin{bmatrix} \Sigma_1 & \Sigma_{1,2} & \dots & \Sigma_{1,i} \\ \Sigma_{1,2}^T & \Sigma_2 & \dots & \Sigma_{2,i} \\ \vdots & \vdots & \ddots & \vdots \\ \Sigma_{1,i}^T & \Sigma_{2,i}^T & \dots & \Sigma_i \end{bmatrix} = \begin{bmatrix} \Sigma_{1:i-1} & \Sigma_{1:i-1,i} \\ \Sigma_{1:i-1,i}^T & \Sigma_i \end{bmatrix} \tag{11.3}$$

$$\Sigma_{i|\boldsymbol{t}^1,...\boldsymbol{t}^{i-1}} = \Sigma_i - \Sigma_{1:i-1,i}^T \Sigma_{1:i-1}^{-1} \Sigma_{1:i-1,i} \tag{11.4}$$

$$\mu_{i|\boldsymbol{t}^1,...\boldsymbol{t}^{i-1}} = \mu_i + \Sigma_{1:i-1,i}^T \Sigma_{1:i-1}^{-1} (\boldsymbol{t}^{1:i-1} - \mu_{1:i-1}) \tag{11.5}$$

The likelihood of the images is taken to be the usual Laplacian of the integral over the difference between the template and the warped image.

$$P(I|\{\boldsymbol{t}^1, ..., \boldsymbol{t}^i\}, R) = e^{-\beta \int_\Omega \{R - I(\varphi^1(...(\varphi^i(\boldsymbol{x}, t^i), ...))t^1)\}^2 \delta\boldsymbol{x}} \tag{11.6}$$

where Ω denotes the support of the reference. We maximize the posterior probability by minimizing minus the logarithm of the measure. Assuming a uniform

distribution of R and ignoring the scaling factor $P(I)$ we seek to maximize the following measure on each scale

$$\int_{\Omega} \{R - I(\varphi^1(...(\varphi^i(\boldsymbol{x}, t^i), ...)t^1))\}^2 \delta\boldsymbol{x} + \alpha \|t^i - \mu^i\|^2_{\Sigma_{i|\boldsymbol{t}^1,...,\boldsymbol{t}^{i-1}}} \tag{11.7}$$

where $\alpha = \gamma/\beta$ is assumed to be known. The important contribution in the presented work, is the changes in the regularization term, which is usually based on a simple regularization on the current level alone. In (11.7) this is changed to regularization according to what our previous knowledge levels tells us. Sections 11.2.2 and 11.2.3 describe how statistical models are build, and especially how a conditional statistical model is build taking advantage of this result, in creating a sparse parameterization of the composed image registration problem.

11.2.2 Statistical deformation models

In statistical deformation models principal component analysis (PCA) is the preferred method [133]. The attractive properties of the PCA for shape modeling include optimal linear reconstruction of the data set variance, the estimated modes of variation are orthogonal and uncorrelated, and a closed form solution exists for calculating the principal components at a relatively low computational cost. For Gaussian distributed random variables, PCA yields the most compact representation of the model.

The deformation model is built from n displacement fields $U = \{U_i\}$ representing the deformations. In the present work these displacement fields are parameterized by the set of parameters $\boldsymbol{t} = \{\boldsymbol{t}^1, \boldsymbol{t}^2, ..., \boldsymbol{t}^m\}$. The d-dimensional deformation fields parameterized by a total of k parameters on the m different levels are collected in random vectors $\boldsymbol{t}_i \in \mathcal{R}^{dk}$.

From $\boldsymbol{t}_i$, a linear shape model, which approximates the parameterization of a given field $\boldsymbol{t}$ is given by $\bar{t}$ and $\boldsymbol{\Phi}$ as

$$\boldsymbol{t} = \bar{\boldsymbol{t}} + \boldsymbol{\Phi}\boldsymbol{b} \ . \tag{11.8}$$

Here $\bar{\boldsymbol{t}}$ is the mean of all n parameter sets. That is

$$\bar{\boldsymbol{t}} = \frac{1}{n} \sum_{i=1}^{n} \boldsymbol{t}_i \ . \tag{11.9}$$

The matrix $\boldsymbol{\Phi}$ is constructed from the l first eigenvectors $\boldsymbol{\Phi}_i$ of the covariance matrix $\boldsymbol{\Sigma}$, given by

$$\boldsymbol{\Sigma} = \frac{1}{n-1} \sum_{i=1}^{n} (\boldsymbol{t}_i - \bar{\boldsymbol{t}})(\boldsymbol{t}_i - \bar{\boldsymbol{t}})^\top \ . \tag{11.10}$$

As usual the eigenvalues corresponding to $\mathbf{\Phi}_i$ are denoted by λ_i. The vectors $\mathbf{\Phi}_i$ are also referred to as the *principal modes*. Finally, $\boldsymbol{b} \in \mathcal{R}^l$ is the parameter vector, describing the contribution of the principal modes contained in $\mathbf{\Phi}$ in order to approximate $\boldsymbol{t}$ by the estimated linear model. By assuming a Gaussian distribution on the single displacement entries, the variance of the elements of $\boldsymbol{b}$, the parameters b_i, are best approximated by λ_i [133].

11.2.3 Conditional Statistical Model Building

Returning to (11.7), and optimizing on level i, the conditional variance of the parameters is in effect determining the regularization. Consequently some combinations of parameters are deemed very unlikely, given the correctness of the model, which encourages us to choosing a more dense representation, which explicitly rules out the unlikely configurations. This is the motivation for changing the parameterization from $\boldsymbol{t}^i$ to the model described in the current section.

Given the conditional covariance matrix $\Sigma_{i|\boldsymbol{t}^1,\ldots,\boldsymbol{t}^{i-1}}$, define

$$\boldsymbol{V}^T_{i|\boldsymbol{t}^1,\ldots,\boldsymbol{t}^{i-1}} \boldsymbol{L}_{i|\boldsymbol{t}^1,\ldots,\boldsymbol{t}^{i-1}} \boldsymbol{V}_{i|\boldsymbol{t}^1,\ldots,\boldsymbol{t}^{i-1}} = \Sigma_{i|\boldsymbol{t}^1,\ldots,\boldsymbol{t}^{i-1}} \ , \tag{11.11}$$

where $\mathbf{\Phi}_{i|\boldsymbol{t}^1,\ldots,\boldsymbol{t}^{i-1}}$ are the orthonormal eigenvectors of $\Sigma_{i|\boldsymbol{t}^1,\ldots,\boldsymbol{t}^{i-1}}$ and $\mathbf{\Lambda}_{i|\boldsymbol{t}^1,\ldots,\boldsymbol{t}^{i-1}}$ contains the corresponding eigenvalues. We will denote a submatrix with the l biggest eigenvalues and the matrix with the corresponding eigenvectors by $\mathbf{\Lambda}'$ and $\mathbf{\Phi}'$ respectively. Then the following will be approximating $\boldsymbol{t}^i$

$$\boldsymbol{t}^i \approx \mu_{i|\boldsymbol{t}^1,\ldots\boldsymbol{t}^{i-1}} + \mathbf{\Phi}'\mathbf{\Lambda}'\boldsymbol{b}' \ , \tag{11.12}$$

where $\boldsymbol{b}'$ is a random vector with uncorrelated univariate elements, according to the general assumption of Gaussian distributed deformation parameters. With this representation we are ready to state the major result of the presented work, which relates to conditional regularization described in (11.7).

$$\alpha\|t^i - \mu^i\|^2_{\Sigma_{i|\boldsymbol{t}^1,\ldots,\boldsymbol{t}^{i-1}}} \approx \alpha\|\mathbf{\Phi}'\mathbf{\Lambda}'\boldsymbol{b}'\|^2_{\Sigma_{i|\boldsymbol{t}^1,\ldots,\boldsymbol{t}^{i-1}}} = \alpha\|\boldsymbol{b}'\|^2_{L_2} \ . \tag{11.13}$$

This means that the regularization reduces to simple sum of squared distances on the introduced parameters. Using this representation we have gained a sparse parameterization with l parameters instead of all the parameters on level i.

11.3 Validation

The LADIS (Leukoaraiosis and DISability) study [119], is a pan-European study involving 12 hospitals and more than 700 patients. The purpose of the current

work is to analyze the Corpus Callosum based on mid-sagittal cross-sections of the brain. A subset consisting of 62 annotated two dimensional MR images of the Danish patients were selected for the current work. In this study it is of great interest to infer the possible variations in shape that we can expect to observe. To analyze these variations we need a pixelwise correspondence, which, we believe, is best achieved using image registration. Each corpus callosum has been manually annotated by a clinician with 72 landmarks, which we use for validating our method.

Our approach for building statistical deformation models was tested on a set of 62 2D MR images of the Corpus Callosum. Due to the limited number of images 6-fold cross validation was used to obtain the results presented in this section. Prior to the model building the 62 images were rigidly aligned to each other by performing Procrustes analysis on the ground truth outline. Initially, the images in the training set were non-rigidly registered to the mean image, as an estimator of the reference image, a registration result is illustrated in Figure 11.2. A new reference was then constructed by averaging the non-rigidly aligned images, and a new non-rigid alignment was subsequently performed. This process was repeated multiple times until the reference stabilized. Four grid levels were used to model the deformation with node spacings equal to 60, 30, 15 and 8 pixels, respectively.

To validate our registration we computed the Dice measures between the ground truth outline and the outline of the warped reference. The dice measure was 0.875 ± 0.042, which is very satisfactory, and much better than the on obtained from just the alignment. Figure 11.3 displays the cumulative overlap before and after non-rigid registration.

From the final deformation fields a statistical deformation model was created by performing PCA separately on each grid level. At each level the number of modes was chosen such that at least 95% of the total variation was explained, and the modes were scaled with the std. dev. to ensure that all parameters had unit variance. Figure 11.1 plots the total explained variance in the coarsest level model as a function of the number of modes. When the entire dataset was used for the model construction this resulted in 50 modes distributed among the grid levels (6, 8, 14 and 22 components). Each deformation field was parameterized with the model and the covariance between parameters across the grid levels were computed. Figure 11.4 displays the first mode of the first level displaced ± 3 std. dev. and illustrates how the covariance creates a conditional prior on the following modes. Afterwards, the remaining Corpus Callosum were registered to the reference using the deformation model. First, the coarsest level was fitted. At each level the parameters of the prior levels were then used to create a conditional prior on the current level. The dice measure for the registrations with the deformation model was 0.8615 ± 0.051

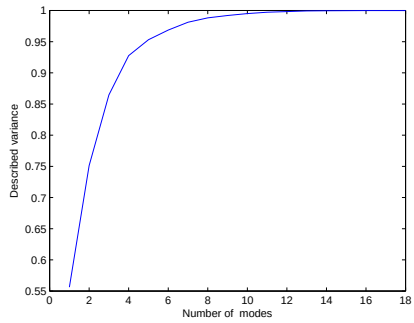

Figure 11.1: Plot relating explained variance of the coarsest level with number of modes included in the coarsest level model.

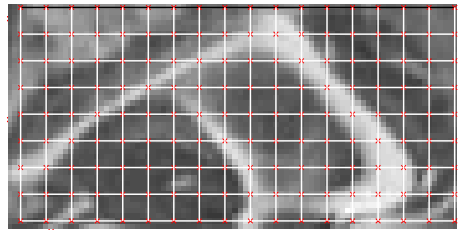

(a) Template image

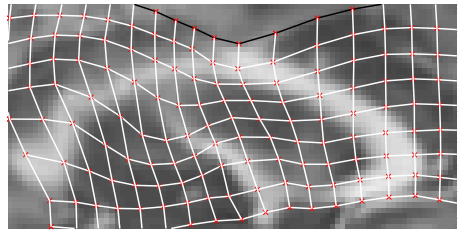

(b) Warped template

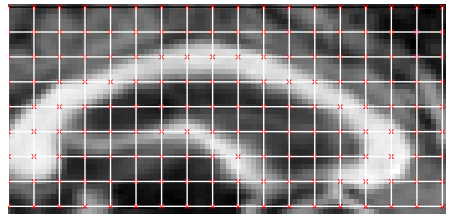

(c) Reference image

Figure 11.2: Registration of an image to the reference.

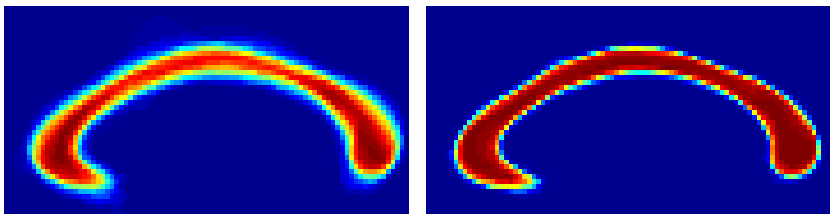

(a) Before nonrigid registration (b) After nonrigid registration

Figure 11.3: Cumulative overlap of the aligned corpus callosum shapes before and after our non-rigid registration

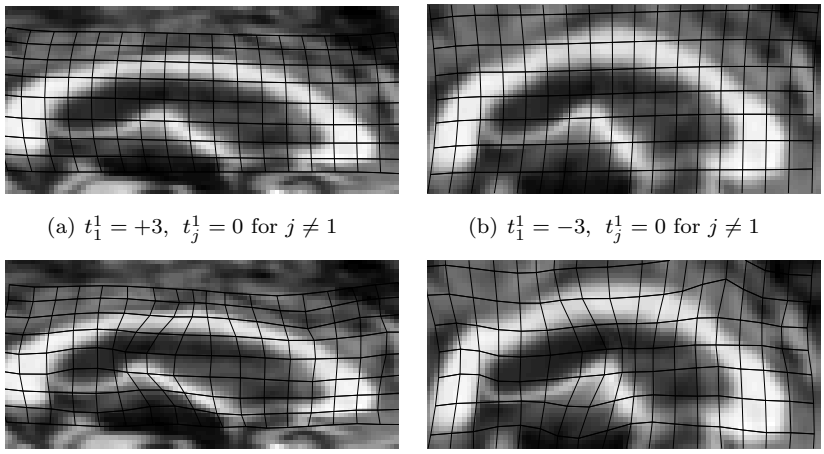

(a) $t_1^1 = +3,\ t_j^1 = 0$ for $j \neq 1$ (b) $t_1^1 = -3,\ t_j^1 = 0$ for $j \neq 1$

(c) $E(\boldsymbol{t}^4, \boldsymbol{t}^3, \boldsymbol{t}^2 | t_1^1 = +3)$ (d) $E(\boldsymbol{t}^4, \boldsymbol{t}^3, \boldsymbol{t}^2 | t_1^1 = -3)$

Figure 11.4: (a) and (b) illustrate the first mode of the PCA model for the coarsest grid level. (c) and (d) show the deformation resulting from the conditional means of $\boldsymbol{t}^4, \boldsymbol{t}^3, \boldsymbol{t}^2$ for $t_1^1 = \pm 3$.

11.4 Discussion

We present a novel deformation model especially designed for optimization in grid based models, while retaining most of the covariance between grid resolutions. The method is validated on a data set of MR images of the brain of 62 patients. We presented a new statistical deformation model suited for parameterized grids with different resolutions. Our method models the covariances between multiple grid levels explicitly, and allows for very efficient fitting of the model to data on multiple scales. We obtained a dice measure of 0.875 ± 0.042 when we registered the training set without a shape prior, and a dice measure of 0.8615 ± 0.051 when we registered the remaining shapes while constraining the shape prior.

11.a Implementation

The compositional warp used in this paper was constructed by composing a sequence of the grid based diffeomorphisms introduced by Cootes et al [37]. These diffeomorphisms can be viewed as an extension to standard linear interpolation, where the interpolation coefficients are transformed by a suitable kernel $k(r)$ which ensures smoothness across the grid boundaries. The displacement of a 2D point $\boldsymbol{x} \in \mathbb{R}^2$ is given by

$$\boldsymbol{u}(\boldsymbol{x}, \boldsymbol{d}) = \sum_{m=0}^{1}\sum_{n=0}^{1} k_n(v)k_m(w)\boldsymbol{d}_{i+n,j+m} = \sum_{m=0}^{1}\sum_{n=0}^{1} a_{i+m,j+n}(\boldsymbol{x})\boldsymbol{d}_{i+n,j+m} = \begin{bmatrix} \boldsymbol{a}(\boldsymbol{x})^\top & \boldsymbol{0} \\ \boldsymbol{0} & \boldsymbol{a}(\boldsymbol{x})^\top \end{bmatrix} \boldsymbol{d} \tag{11.14}$$

where $k_0(r) = k(r)$, $k_1(r) = 1 - k(r)$, i and j are the local indices of the neighboring grid points, v and w are relative positions of $\boldsymbol{x}$ in the neighborhood and $\boldsymbol{d}$ and $\boldsymbol{d}_{i,j}$ are all the displacements and the displacement of the (i, j)-node, respectively. For this problem the kernel $k(r) = \frac{1}{2}(1 + \cos(\pi r))$ was chosen. According to Cootes et. al. [37] this kernel ensures diffeomorphism as long as no node is displaced more than $1/\pi$ of the original node spacing.

11.a.1 Image registration

To drive the registration between a reference image R and a target image I we apply the sum-of-squared-differences (SSD) as our similarity measure and the Mahalanobis distance $\|.\|_\Sigma$ as our regularization term

$$\begin{aligned} F(\boldsymbol{t}) &= \frac{1}{2}\sum_{\boldsymbol{x}}(R(\boldsymbol{x}) - I(\boldsymbol{\varphi}(\boldsymbol{x},\boldsymbol{t}))^2 + \alpha\|\boldsymbol{t}\|^2_\Sigma \\ &= \frac{1}{2}\sum_{\boldsymbol{x}} E^2(\boldsymbol{x},\boldsymbol{t}) + \alpha\|\boldsymbol{t}\|^2_\Sigma. \end{aligned} \tag{11.15}$$

To achieve a fast optimization we apply the inverse compositional optimization approach by Baker et al. [16] to the cost function. Thus, we obtain a minimum by iteratively minimizing

$$F_{ic}(\boldsymbol{t}) = \frac{1}{2}\sum_{\boldsymbol{x}}(R(\boldsymbol{\varphi}(\boldsymbol{x},\Delta\boldsymbol{t})) - I(\boldsymbol{\varphi}(\boldsymbol{x},\boldsymbol{t}))^2 + \alpha\|\boldsymbol{t} - \frac{\partial \boldsymbol{t}'}{\partial \Delta\boldsymbol{t}}\Delta\boldsymbol{t}\|^2_\Sigma \tag{11.16}$$

with respect to $\Delta\boldsymbol{t}$ and updating $\boldsymbol{t}$ according to

$$\boldsymbol{\varphi}(\boldsymbol{x},\boldsymbol{t}') \leftarrow \boldsymbol{\varphi}(\boldsymbol{x},\boldsymbol{t}) \circ \boldsymbol{\varphi}^{-1}(\boldsymbol{x},\Delta\boldsymbol{t}). \tag{11.17}$$

In [78] we showed how $\boldsymbol{t}'$ can be derived from (11.17).

By performing a first-order Taylor-expansion on $R(\boldsymbol{\varphi}(\boldsymbol{x},\Delta\boldsymbol{t})$ around $\boldsymbol{x}$ in (11.16), taking the derivatives wrt. $\Delta\boldsymbol{t}$ and setting them equal to zero we get

$$\Delta\boldsymbol{t} = \boldsymbol{H}^{-1}\left[\sum_{\boldsymbol{x}} \boldsymbol{SD}(\boldsymbol{x})^\top E(\boldsymbol{x},\boldsymbol{t}) + \alpha\frac{\partial \boldsymbol{t}'}{\partial \Delta\boldsymbol{t}}^\top \Sigma^{-1}\boldsymbol{t}\right] \tag{11.18}$$

where

$$\boldsymbol{SD}(\boldsymbol{x}) = \nabla R(\boldsymbol{x})\frac{\partial \boldsymbol{\varphi}(\boldsymbol{x},\boldsymbol{0})}{\partial \boldsymbol{t}} \tag{11.19}$$

and

$$\boldsymbol{H} = \sum_{\boldsymbol{x}} \boldsymbol{SD}(\boldsymbol{x})^\top \boldsymbol{SD}(\boldsymbol{x}) + \alpha\left[\frac{\partial \boldsymbol{t}'}{\partial \Delta\boldsymbol{t}}\right]^\top \Sigma^{-2}\left[\frac{\partial \boldsymbol{t}'}{\partial \Delta\boldsymbol{t}}\right]. \tag{11.20}$$

The advantages with this inverse compositional approach is that $\boldsymbol{SD}(\boldsymbol{x})$ can be pre-computed as it is not dependent on $\boldsymbol{t}$.

Chapter 12

Generating Quality Tetrahedral Meshes from Binary Volumes

Mads Fogtmann Hansen, Jakob Andreas Bærentzen and Rasmus Larsen

Abstract

This paper presents two new quality measures for tetrahedra which are smooth and well-suited for gradient based optimization. Both measures are formulated as a distance from the regular tetrahedron and utilize the fact that the covariance of the vertices of a regular tetrahedron is isotropic. We use these measures to generate high quality meshes from signed distance maps. This paper also describes an approach for computing (smooth) signed distance maps from binary volumes as volumetric data in many cases originate from segmentation of objects from imaging techniques such as CT, MRI, etc. The mesh generation is split into two stages; a candidate mesh generation stage and a compression stage, where the surface of the candidate mesh is moved to the zero iso-surface of the signed distance maps, while one of the quality measures ensures that the quality remains high.

We apply the mesh generation algorithm on four examples (torus, Stanford dragon, brain mask, and pig back) and report the dihedral angle, aspect ratio and radius-edge ratio. Even though, the algorithm incorporates none of the mentioned quality measures in the compression stage it receives a good score for all these measures. The minimum dihedral angle is in none of the examples smaller than 15^o.

12.1 Introduction

High quality tetrahedral mesh generation is an important element in many medical imaging applications such as virtual surgery [47, 90, 157], image registration [23, 110] and biological modeling [36, 105]. Creation of meshes, which can sustain large soft tissue deformations, is challenging due to high demands in accuracy, efficiency and structural integrity. Efficiency is achieved by having only the minimum required resolution in all areas of the mesh. High resolution is required in high curvature areas near the interface of the object, while lower resolution is sufficient in areas far from the interface and in areas with low curvature. Accuracy and structural integrity are primarily a matter of ensuring that the number of very anisotropic tetrahedra are kept at an absolute minimum. Such tetrahedra will often be biased[1] or/and invert under deformation. Unfortunately, efficiency does not go hand-in-hand with accuracy and structural integrity as anisotropic tetrahedra will emerge when large and small tetrahedra are in close proximity of each other.

In this paper, we propose to generate quality meshes from signed distance maps (SDMs) by generating a candidate mesh as proposed by Molino et al. [109] and subsequently compressing the candidate mesh to the surface of the object. The compression is formulated as a gradient based optimization problem where the surface points of the candidate mesh iteratively are moved to zero iso-surface of SDM. A selected quality measure is applied during the compression to regularize the evolution in order to ensure that the quality of the final mesh is high.

An extensive number of quality measures for triangles and tetrahedra can be found in the literature, c.f. [120, 145] for surveys. Most of these measures are non-smooth, only piecewise smooth or difficult to differentiate, and thus not suited for gradient based optimization. Therefore, we propose two new quality measures for tetrahedra which essentially measure the distance or deviation from a given tetrahedron to the regular tetrahedron. They are both differentiable (smooth) and rotation- and scale-invariant.

In many of the above mentioned applications the objects to be tesselated are segmented from medical images and therefore represented as binary volumes. We convert a binary volume to a SDM by computing all distances in the volume to the nearest zero-crossing voxel, fitting an implicit function to a suitable narrow band of the zero-crossing distance map and finally computing the distances to the zero iso-surface of the implicit function.

[1] They exhibit a referred direction of deformation

12.2 Related work

Early mesh generation in 2D was pioneered with the Delaunay triangulation [142], and it is probably the most widely used technique for 2D mesh generation today. The extension of the Delaunay triangulation to 3D [143, 172] has unfortunately proven to be unsuitable for many practical application as it admits so-called slivers which are collapsed tetrahedra with a negligible volume. Several methods for sliver removal [28, 52] have been proposed yet none of these methods have proven to work convincingly [142]. Another problem with Delaunay triangulation is that it tessellates the entire convex region of the set of input points, and thus it does not conform to the boundary of the object. Constrained Delaunay methods [29, 59, 144] have been proposed but they are complex and maybe too complex for unstructured mesh generation.

A number of unstructured mesh generation techniques implement a two stage strategy which is similar to our approach. Neugebauer and Klein [114] use a marching cube mesh as a candidate mesh, Radovitzky and Ortiz [124] use a face-centered cubic lattice, Molino et al. [109] use a body-centered cubic (BCC) lattice followed by a subdivision strategy and finally Fuchs [64] uses a Delaunay triangulation of vertices placed on a BCC lattice.

In general, two types of strategies have been suggested for the compression: projection and evolution. Neugebauer and Klein [114] and Grosskopf and Neugebauer [69] implement projection strategies while Kobbelt et al. [88], Wood et al. [176] and Molino et al. [109] apply evolution strategies using connectivity, spring forces or Laplacian smoothing to regularize the evolution. Molino et al. [109] also suggest using aspect ratio (defined as the shortest altitude divided by the longest edge) as a regularizer in a discrete optimization scheme.

12.3 Methods

We wish to construct a tetrahedral mesh representation of an object Ω given a signed distance map or binary volume representation of the object. For now we will assume a SDM representation is available and later in this section present an approach for converting a binary volume to a SDM. Formally, we define the Euclidian SDM of an object Ω as a function

$$\Phi(x) = \operatorname{sgn}(x) \min_{y \in \Gamma} \|x - y\|,$$

where

$$\text{sgn}(x) = \begin{cases} -1 & x \in \Omega \\ 1 & x \notin \Omega \end{cases}$$

and Γ is the interface/boundary of the object.

A candidate mesh is generated as described in Molino et al. [109]. A BCC lattice covering the boundary box of the object is chosen as an initial mesh. Tetrahedra, which are certain to be outside the object, are removed and the resolution of the mesh is increased in the high curvature areas of the SDM of the object using a Red-Green subdivision approach. More tetrahedra are removed in a final step, such that (i) the boundary is a manifold, (ii) no tetrahedra have all four nodes on the boundary, and (iii) no interior edge connects to boundary nodes, cf. [109] for a detailed description. The process is illustrated in Figure 12.4.

In the compression phase the surface points of the candidate mesh are moved towards the zero iso-surface of the signed distance map (SDM) while a regularizer is applied to ensure a high mesh quality. This is done by minimizing the functional

$$F(\Delta V) = \sum_{1}^{N_s} \Phi(V_{s_i} + \Delta V_{s_i})^2 + \gamma \sum_{i=1}^{N_t} r(V_{T_i} + \Delta V_{T_i}), \tag{12.1}$$

where V are the vertices of the candidate mesh, ΔV are the displacements of the vertices, s is the set of boundary vertices, T_i contains the id's of the vertices of the ith tetrahedron and r is a regularizer, which measures the quality of a single tetrahedron.

12.3.1 The quality of a tetrahedron

As mentioned, we are interested in generating meshes which are suitable for large deformations, and as such we wish to define the quality of a tetrahedron in terms of its ability to handle large deformations. In general, if a mesh is biased, such that the tetrahedra are primarily elongated in one direction, the mesh will tend to be either more soft or stiff in the thin direction [109]. Essentially, the optimal tetrahedron is a regular (equilateral) tetrahedron. It is however not possible to tessellate a 3D Euclidian space with regular tetrahedra.
Therefore, we wish to describe the quality of a tetrahedron in terms of its distance from a regular tetrahedron. A unique property of a regular tetrahedron is that the covariance matrix of the vertices is isotropic.

Theorm 12.1 *The covariance matrix Σ_T of the vertices of a tetrahedron T is isotropic $\Sigma_T = sI$ iff T is a regular tetrahedron, where s is a scaling factor.*

PROOF. Let T be an arbitrary tetrahedron represented by a 3x4 matrix Q containing the four vertices of T. Without loss of generality we will assume that the barycenter of T lies in the origin. Thus, we must prove that

$$\Sigma_T = QQ^T = I, \tag{12.2}$$

iff T is a regular tetrahedron. s is neglected as it is just a scaling factor.

The regular tetrahedron $\tilde{Q}$ represented by the vertices $(-\frac{1}{\sqrt{2}}, -\frac{1}{\sqrt{12}}, \frac{1}{\sqrt{6}})$, $(\frac{1}{\sqrt{2}}, -\frac{1}{\sqrt{12}}, \frac{1}{\sqrt{6}})$, $(0, \frac{\sqrt{3}}{2}, 0)$ and $(0, -\frac{1}{\sqrt{12}}, -\frac{\sqrt{2}}{\sqrt{3}})$ is a solution to Eq. 12.2.

For any Q there exists a transformation matrix A such that $Q = A\tilde{Q}$. If Q fulfills Eq. 12.2 we get

$$QQ^T = A\tilde{Q}\tilde{Q}^T A = AA^T = I.$$

Thus, A is a rotation matrix, which implies that all solutions are geometrically equivalent. It follows that all solutions are regular tetrahedra.

In contrast to the regular tetrahedron, an elongated tetrahedron has a high variance in the stretched direction and smaller variation perpendicular to that direction. As such an eigenvalue decomposition of the covariance matrix of an elongated tetrahedron will give one eigenvalue (corresponding to the stretched direction) which is relative large compared to the two remaining eigenvalues. The normalized covariance matrix of a regular tetrahedron has eigenvalue 1 with multiplicity 3 (isotropic). This implies that the disparity of the eigenvalues is related to the degree of anisotropy of a tetrahedron. Inspired by the *Riemannian elastic* [122] and the *St Venant-Kirchoff elastic* [33] energies we propose to use the measures

$$\begin{aligned} r_{log}(V) &= \frac{3}{4}\mathrm{tr}\left(\log^2\left(\frac{\Sigma(V)}{\det(\Sigma(V))^{\frac{1}{3}}}\right)\right) \\ &= \frac{1}{4}\left(3\sum_{i=1}^{3}\log(\lambda_i)^2 - \left(\sum_{i=1}^{3}\log(\lambda_i)\right)^2\right), \end{aligned} \tag{12.3}$$

and

$$
\begin{aligned}
r_{eig}(V) &= \frac{1}{4}\mathrm{tr}\left(\left(\frac{\Sigma(V)}{\det(\Sigma(V))^{\frac{1}{3}}} - I\right)^2\right) \\
&= \frac{1}{4}\left(3 + \frac{\sum_{i=1}^{3}\lambda_i^2}{(\prod_{i=1}^{3}\lambda_i)^{\frac{2}{3}}} - 2\frac{\sum_{i=1}^{3}\lambda_i}{(\prod_{i=1}^{3}\lambda_i)^{\frac{1}{3}}}\right),
\end{aligned} \tag{12.4}
$$

where $\Sigma(V)$ is the covariance of the vertices V (represented by a $3x4$ matrix), λ_i is the ith eigenvalue of covariance matrix Σ and log is the natural logarithm (matrix logarithm when applied to a matrix). The term $\frac{\Sigma}{\det(\Sigma)^{\frac{1}{3}}}$ will be denoted the normalized covariance matrix. The two measures r_{log} and r_{eig} are similar to the above mentioned elastic energies with the exception that the *Cauchy-green* deformation tensor has been replaced by the normalized covariance matrix. Note, that both measures are rotation-invariant as they are based purely on the eigenvalues of the covariance matrix, and scale-invariant as we normalize the covariance matrix. Figure 12.1 illustrates how the two quality measures behave when a tetrahedron deviates from the regular tetrahedron. A nice property of both measures is that they will evaluate to *infinity* when V describes a collapsed tetrahedron. Furthermore, both quality measures will return zero when applied to a regular tetrahedron.

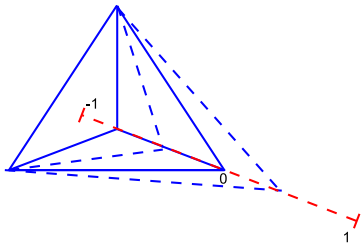

(a) Deformation illustration.

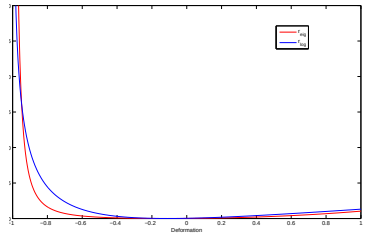

(b) Quality as a function of deformation.

Figure 12.1: Comparison plot of quality measures. Tetrahedra were generated by moving a vertex along the line defined by the normal and the barycenter of the opposite face (regular triangle). The deformation has been scaled such that -1 corresponds to the collapsed tetrahedron and 0 corresponds to the regular tetrahedron.

Given the eigenvalue decomposition $\Sigma = RLR^T$, we can compute the derivative of the measures with respect to Σ by

$$
\partial_\Sigma r_{log} = \frac{1}{2}RL^{-1}\left(3\log(L) - I\sum_{i=1}^{3}\log(\lambda_i)\right)R^T.
$$

and

$$\partial_\Sigma r_{eig} = \frac{1}{2}\left(\left(\frac{\sum_{i=1}^3 \lambda_i}{(\prod_{i=1}^3 \lambda_i)^{\frac{1}{3}}} - \frac{\sum_{i=1}^3 \lambda_i^2}{(\prod_{i=1}^3 \lambda_i)^{\frac{2}{3}}}\right)\Sigma^{-1} - \frac{1}{(\prod_{i=1}^3 \lambda_i)^{\frac{1}{3}}} I + \frac{1}{(\prod_{i=1}^3 \lambda_i)^{\frac{2}{3}}}\Sigma\right)$$

Let P_o denote the projection matrix which centers a tetrahedron such that its barycenter lie in the origin. Hence, $E(V) = VP_oP_o^TV^T$. Thus, the derivatives of the measures with respect to V are

$$\partial_V r_{log} = 2P_oP_o^TV^T\partial_\Sigma r_{log}$$

and

$$\partial_V r_{eig} = 2P_oP_o^TV^T\partial_\Sigma r_{eig}.$$

12.3.2 Converting a binary volume to a signed distance map

A binary volume can be converted to a discretized SDM by computing the Euclidian signed distance $\Phi_{zc}(x)$ from all voxels in the binary volume to the nearest zero-crossing voxel, fitting an implicit surface $I_{srf}(x, w)$ to a suitable narrow band of $\Phi_{zc}(x)$, and finally computing the distances $\tilde{\Phi}(x)$ from all voxels to the zero iso-surface of $I_{srf}(x, w)$.

In this paper, we model the implicit surface $I_{srf}(x, w)$ with a set of cubic B-spline basis functions placed on a regular lattice. The weight parameters w are estimated by minimizing

$$F(w) = \sum_{i=1}^{N} C(x_i, w) + \alpha(\|\nabla I_{srf}(x_i, w)\| - 1)^2, \tag{12.5}$$

where

$$C(x, w) = \begin{cases} (\Delta d(x, w) - \frac{1}{2}s)^2 & \textbf{if } \Delta d(x, w) > \frac{1}{2}s \\ (\Delta d(x, w) + \frac{1}{2}s)^2 & \textbf{if } \Delta d(x, w) < -\frac{1}{2}s \\ 0 & \textbf{otherwise} \end{cases},$$

$\Delta d(x, w) = \Phi_{zc}(x) - I_{srf}(x, w)$ and s is the width of the voxels. The reason to use $C(x, w)$ as measure of the 'fit' and not the usual *least-squares* fit is that the error of $d_{zc}(x)$ is uniformly distributed. The term $(\|\nabla I_{srf}(x_i, w)\| - 1)$ provides

a natural regularization, especially in the zero-crossing areas, as $\|\Phi(x)\| = 1$ is a fundamental property of the Euclidian distance field. The property is not applied as a hard constraint as the B-spline will not be able to fulfill the constraint in the entire narrow band, and the narrow band might contain areas where the true Euclidian distance field is discontinuous.

Given the implicit surface we can find the shortest distance from any voxel x to the zero level set of I_{srf} using the nearest zero-crossing voxel as an initial guess of y. Thus, the task is to find the point y which minimizes $\tilde{\Phi}^2(x, y) = \|x - y\|^2$ s.t. $I_{srf}(y, w) = 0$. This problem can be solved with the Augmented Lagrangian method [99]. Alternatively, y can be updated iteratively with $-\tau dy$, where dy is given by

$$dy = \nabla I_{srf}(y, w) I_{srf}(y, w) + \beta(I - nn^T)(x - y), \tag{12.6}$$

and $n = \frac{\nabla I_{srf}(y,w)}{\|I_{srf}(y,w)\|}$ is normal of the iso-surface at the point y. The first term of dy pushes the point y towards the zero iso-surface, while the second term tries to minimize the distance between x and y by moving y in the tangential plane of the surface. A suitable τ can be found with line-search. Selecting $\beta = 0.1$ seems to work in most cases.

12.4 Implementation issues

If Eq. 12.1 is differentiable it can be minimized by a gradient based optimization scheme. As the discrete representation of the SDM is obviously not differentiable we wrap the SDM with a cubic B-spline interpolator such that the signed distances and derivatives can be evaluated in the entire Euclidean space. Furthermore, as the regularization term in Eq. 12.1 works independently on each tetrahedron it does not directly discourage overlap between the tetrahedra in a mesh. We handle this issue by having the regularizer return *infinity* if an inversion/overlap occurs. This is theoretically correct as our measures evaluate to *infinity* in the case of a collapsed tetrahedron - in an evolution based approach a tetrahedron must collapse before it can invert. We minimize Eg. 12.1 using a limited memory BFGS optimizer.

	Torus	Dragon	Brain	Carcass
MiDA	36^o	19^0	26^o	15^o
MaDA	144^o	157^0	146^o	165^o
MaRE	1.1	2.3	1.5	2.2
AvRE	0.7	0.8	0.8	0.8
MaAR	3.3	6.7	4.4	7.9
AvAR	1.8	1.9	1.8	2.1

Table 12.1: Quality of generated meshes using r_{log}.

12.5 Results

To test the quality measures, we have selected four examples. The first example is the torus where the SDM was computed directly from the parametrization of the torus. The second example is the Stanford dragon where the SDM was computed from the polygonal mesh. The third example is a brain mask which was extracted from an MRI of a human brain. The final example is a half pig back which was extracted from a CT scan by thresholding the background. The SDMs of the two last examples were computed as described in Section 12.3.2.

The resulting tetrahedral meshes are displayed in Figures 12.2, 12.3, 12.4 and 12.5. The meshes shown in the figures were generated with r_{eig}. Tables 12.1 and 12.2 list the minimum and maximum dihedral angles (MiDA and MaDA), the maximum and average aspect ratio (MaAR and AvAR) as well as the maximum and average radius-edge[2] ratio (MaRE and AvRe) for r_{log} and r_{eig}, respectively. From Tables 12.1 and 12.2 we note that r_{eig} in general obtain slightly better results than r_{log}.

Molino et al. [109] report the MiDA, MaDA MaAR and AvAR for a tetrahedral mesh of the Stanford dragon consisting of approximately 500k elements (comparable to our dragon mesh) as shown in Table 12.3. In the case of the Stanford dragon our measures r_{log} and r_{eig} obtain better scores for MiDA and AvAR and a worse score for MaDa than the two approaches in Molino et al. Futhermore, Molino et al. are able to obtain only a lower MaAR when minimizing the aspect ratio. It should be noted that our approach regardless of the quality measure is able to obtain a lower AvAR than Molino et al., even though they use the aspect ratio as a regularizer. The elastic regularizer reported in Molino et al. is likewise able to obtain a better AvAR which indicates that our applied optimization procedure fails to produce the optimal result.

[2]Radius of circum-cycle over the minimum edge length

	Torus	Dragon	Brain	Carcass
MiDA	36^o	19^o	27^o	16^o
MaDA	144^o	159^o	144^o	163^o
MaRE	1.1	2.4	1.3	2.3
AvRE	0.8	0.8	0.8	0.8
MaAR	3.1	6.4	3.9	7.9
AvAR	1.8	1.9	1.8	2.0

Table 12.2: Quality of generated meshes using r_{eig}.

	Elastic regularizer	Aspect ratio
MiDA	13^o	16^o
MaDA	154^o	150^o
MaAR	7.6	5.3
AvAR	2.2	2.3

Table 12.3: Quality of dragon mesh (500K elements) reported in [109]. Two different regularizers were applied in the compression phase; one which uses elastic springs and one which tries to minimize the aspect ratio.

12.6 Discussion

We have proposed two new quality measures and tested them on four examples. In section 12.5 Results we compared our results for the Stanford dragon with the results presented in [109]. It should be stated that this comparison may not be fair, as we have not used the same SDM or candidate mesh as Molino et al [109]. Our final dragon mesh is visually close to identical with the dragon mesh in [109], and the numbers of the tetrahedra in the two meshes are almost equal. Thus, we believe that the comparison is quite fair. In the future, we will test the proposed measures in different applications and develop them further. Eg. it is possible to incorporate a weighting matrix into the quadratic form of the measures allowing for preferred deviations from the regular tetrahedron

$$r_W(V) = \frac{3}{4}\mathrm{tr}\left(\log\left(\frac{\Sigma(V)}{\det(\Sigma(V))^{\frac{1}{3}}}\right) W \log\left(\frac{\Sigma(V)}{\det(\Sigma(V))^{\frac{1}{3}}}\right)\right)$$

and to normalize the covariance matrix with its trace (sum of eigenvalues) instead of its determinant (product of eigenvalues)

$$r_{tr}(V) = \frac{3}{4}\mathrm{tr}\left(\log^2\left(3\frac{\Sigma(V)}{\mathrm{tr}(\Sigma(V))}\right)\right).$$

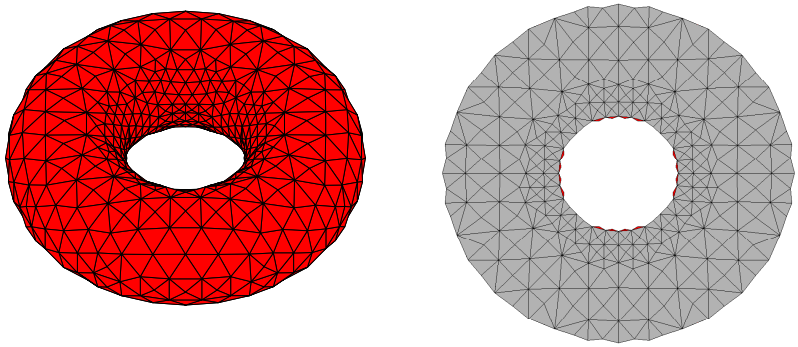

(a) Full (b) Sliced

Figure 12.2: Tetrahedral mesh of torus.

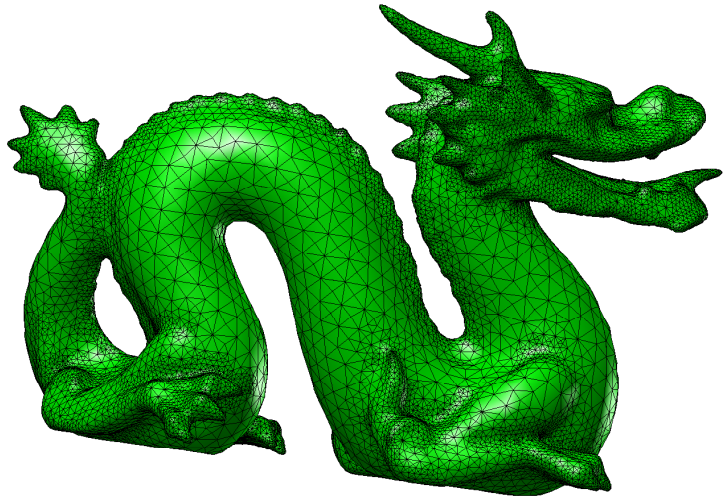

Figure 12.3: Tetrahedral mesh of dragon (540K elements).

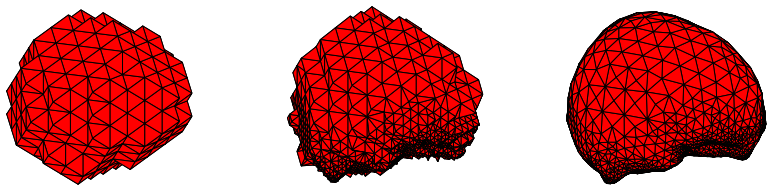

(a) Initial (b) Candidate (c) Final

Figure 12.4: Tetrahedral mesh from mask of human brain (80K elements).

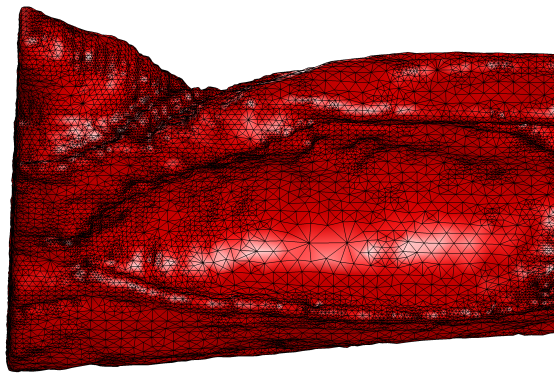

Figure 12.5: Tetrahedral mesh of half pig back (280k elements).

Part III

Discussion

Chapter 13

Discussion

This chapter discusses the presented results w.r.t. the objectives and ends the thesis with a conclusion.

13.1 Discussion

The applications presented in the thesis rely on spatial correspondences obtained from elastic image matching. This naturally implies that the accuracy and the reliability of the applications depend on the accuracy and the reliability of the applied image matching. The intra-subject registrations made on the Thisted data set were implicitly validated by checking the quantity of local compression and expansion. As the deformations were nearly incompressible and the visual differences between reference images and deformable template images were minimal, it was concluded that the estimated deformations were good approximations of the real deformations. No validation has been performed on the inter-subject registrations made by the deformable atlas. The lack of validation of these registrations is the primary short-coming of this thesis project and should be conducted as soon as possible.

A couple of reappearing problems were visually identified in the inter-subject registrations, but they were mostly contributed to poor data quality rather

than limitations in the deformation modeling. An inherit conclusion from these problems is, that the used data set is suboptimal for the purpose of image registration. The author believes that the following observations should be taken into consideration before acquiring new data:

- The low out plane resolution geometrically distorts structures such as the ribs and smooths the spatial image derivatives in the out plane direction.
- It is not always possible to register areas in the proximity of rapid skin surface oscillations.
- Topological difference between the scans of the pork middles greatly complicates the inter-subject registration of the scans or renders it even impossible.
- Deformation due to gravity can be reduced by placing the products, which are to be scanned, in a half pipe resembling the shape of the non-slaughtered pig carcasses.

The first objective of the thesis was to construct a deformable pig atlas from CT scans of pigs carcasses which can be used to study the variation of pigs. The deformable atlas has currently been applied to spatially normalize 299 CT scans of the pork middle and contains five anatomical masks traced upon the reference pig. In addition to virtual cutting, the atlas presents the opportunity to perform a range of studies on the biological variation of pigs, e.g. the statistical extraction of predictors with application to the sorting of pig carcasses. A determination of the value and quality of the atlas awaits a future validation of the quality of the registrations.

The second objective and the main application of the thesis involved the construction of a virtual cutting tool/atlas with the capacity of performing identical virtual cuts on the database of pigs. The cutting atlas uses a mixture of anatomical mask transference, mathematical morphology and simple geometric measures to define cuts. The usage of masks for representing anatomical regions and products provides an elegant and easy way of constructing even complex cuts. The finite element representation of the transformation between reference and template allows for a straightforward transferral of the anatomical masks from the reference frame to the frames of the targets, as the inverse transformation can be explicitly computed. The cutting tool is robust and flexible under the assumption that the recovered spatial correspondences are *correct*.

The final objective was the development of a methodology for comparing virtual and real products. The method can serve as a form for certification tool of the virtual products to raise confidence in the ability of the virtual products

to simulate the real products from the abattoirs. The method requires the estimation of the deformation between the output products and the input product. The deformation in the presented example was unfortunately too large for the image matching criteria alone to drive the registration, and thus required the assistance of landmarks. The dependence on manual intervention is largely unacceptable which demands for a future effort in ensuring a minimal deformation between input product and output products at the time of the scanning. The approach combined with the virtual cutting atlas can facilitate the development of new cutting robots by defining a goal cut in the cutting atlas prior to the development. That is, instead of evaluating the accuracy of the virtual cuts we evaluate the accuracy of the cutting robot against the goal cut defined in the cutting atlas.

The papers included in chapters 9-11 can primarily be considered to be a product of preliminary studies and academic development of the author. They have not been directly applied in the applications of the thesis but they do contain interesting theoretical work in the field of morphology. Chapter 12 presented a tetrahedra tessellation approach which is an essential part of the foundation of the developed image registration framework, RegLab.

13.2 Conclusion

The thesis represents a gateway between the worlds of medical image analysis and meat science, which can be beneficial for both sides. The meat science community can adapt many of the methodologies developed by the medical imaging community and use them to obtain new and useful knowledge, as exemplified by this thesis. Likewise, an interdisciplinary collaboration is helpful for the medical image community as fewer restrictions apply for data acquisition on animals. Thus, the meat science community and industry can supply the researcher in medical imaging with larger and better data sets for test and development of new methods.

Part IV

Appendix

Appendix A

Derivatives

The chapter lists the derivatives of the elasticity energies used in the thesis w.r.t. the Jacobian $\boldsymbol{J}$ of the relative displacement, i.e.

$$\boldsymbol{F} = \boldsymbol{I} + \nabla \boldsymbol{u}(\boldsymbol{x}) = \boldsymbol{I} + \boldsymbol{J}. \tag{A.1}$$

I have tried to write the derivatives in a form which is easy to implement. In some cases, the computation of the derivatives requires the computation of the Green-Lagrangian tensor $\boldsymbol{C} = \boldsymbol{F}^T\boldsymbol{F} = \boldsymbol{U}^2$ and its eigenvalue decomposition $\boldsymbol{C} = \boldsymbol{V}\boldsymbol{D}\boldsymbol{V}^T$. Note, the eigenvalues in the diagonal of $\boldsymbol{D}$ are the squared principal stretches.

1.1 St. Vernant Kirchoff and Riemannian elasticity

The energies and their derivatives will be written in the general anisotropic form of Eq. 4.47. That is, St. Vernant Kirchoff elasticity is on the form

$$r_{svk} = \frac{1}{4}\|\text{vect}(\boldsymbol{C} - I))\|^2_{\boldsymbol{Q}}, \tag{A.2}$$

and Riemannian elasticity is on the form

$$r_{rie} = \frac{1}{4}\|\text{vect}(\log(\boldsymbol{C}))\|^2_{\boldsymbol{Q}}. \tag{A.3}$$

The derivative of r_{svk} w.r.t. $\boldsymbol{J}$ is

$$\partial_{\boldsymbol{J}} r_{svk} = (\boldsymbol{I} + \boldsymbol{J})\text{mat}(\boldsymbol{Q}\text{vect}(\boldsymbol{C} - I)) \tag{A.4}$$

The derivative of r_{rie} w.r.t. $\boldsymbol{J}$ is

$$\partial_{\boldsymbol{J}} r_{rie2} = (\boldsymbol{I} + \boldsymbol{J})\boldsymbol{C}^{-1}\text{mat}(\boldsymbol{Q}\text{vect}(\log(\boldsymbol{C}))), \tag{A.5}$$

where $\log(\boldsymbol{C}) = \boldsymbol{V}\log(\boldsymbol{D})\boldsymbol{V}^T$ and $\boldsymbol{C}^{-1} = \boldsymbol{V}\boldsymbol{D}^{-1}\boldsymbol{V}^T$.

Note, to construct isotropic elasticity energies use a $\boldsymbol{Q}$ on the form shown in Eq. 4.37.

1.2 Volumetric elasticity

The derivative of r_{vol} w.r.t. $\boldsymbol{J}$ is

$$\partial_{\boldsymbol{J}} r_{\text{vol}} = 2M(\det(\boldsymbol{F})^K - 1)^{2M-1}\det(\boldsymbol{F})\boldsymbol{F}^{-1} \tag{A.6}$$

The derivative of $r_{\log}$ w.r.t. $\boldsymbol{J}$ is

$$\partial_{\boldsymbol{J}} r_{\log} = 2M\log(\det(\boldsymbol{F}))^{2M-1}\boldsymbol{F}^{-1} \tag{A.7}$$

1.3 Ogden material model

The derivative of Ogden material model w.r.t. $\boldsymbol{J}$ is

$$\partial_{\boldsymbol{J}} r_{\text{ogd}} = (\boldsymbol{I} + \boldsymbol{J})\boldsymbol{V}\left(\sum_p^M \mu_p \boldsymbol{D}^{\frac{\alpha_p}{2}-1}\right)\boldsymbol{V}^T. \tag{A.8}$$

1.4 Normalized Ogden material model

In the normalized Ogden material model, the principal stretches ε_i is replaced by their normalized version $\tilde{\varepsilon_i} = \varepsilon_i(\prod_{j=1}^{N} \varepsilon_j)^{-\frac{1}{N}}$. The derivative w.r.t. $\boldsymbol{J}$ is

$$\partial_{\boldsymbol{J}} r_{\mathrm{ogd2}} = (\boldsymbol{I} + \boldsymbol{J})\boldsymbol{V} \left(\sum_{p}^{M} \det(\boldsymbol{C})^{-\frac{\alpha_p}{2N}} \mu_p \left(\boldsymbol{D}^{\frac{\alpha_p}{2}-1} - \frac{1}{3}\mathrm{tr}\left(\boldsymbol{D}^{\frac{\alpha_p}{2}}\right) \boldsymbol{D}^{-1} \right) \right) \boldsymbol{V}^T. \tag{A.9}$$

Bibliography

[1] T. W. Anderson. *An introduction to Statistical Analysis.* Wiley-Interscience, 2003.

[2] Aristotle, A. L. Peck, and D. M. Balme. *Historia Animalium.* Harvard University Press, 2004.

[3] J. Ashburner and K. J. Friston. Voxel-Based Morphometry – The Methods. *Neuroimage*, 11(6):805–821, 2000.

[4] Danish Meat Association. Danish Bacon and Meat Council. `http://www.dbmc.co.uk`.

[5] Danish Meat Association. Årsberetning 2006-2007 (In Danish). Technical report, Danish Meat Association, 2007.

[6] Danish Meat Association. Statistisk 2006-2007 (In Danish). Technical report, Danish Meat Association, 2007.

[7] ATTEC. Pork middle cutter. `http://www.attec.dk/Middle-cutter-18.aspx`.

[8] L. Attrup. Krise i svinebranchen rammer slagterierne (In danish). *Børsen*, 2008.

[9] L. Attrup. Kriseramte svinebønder skærer ned (In danish). *Børsen*, 2009.

[10] I. Babuska and M. Suri. The hp Version of the Finite Element Method with Quasiuniform Meshes. Technical report, The Defense Technical Information Center, 1986.

[11] A. Bærentzen and H. Aanæs. Signed Distance Computation using the Angle Weighted Pseudo-normal. *IEEE Transactions on Visualization and Computer Graphics*, 11(3):243–253, 2005.

[12] J. A . Bærentzen. Robust Generation of Signed Distance Fields from Triangle Meshes. *Proceedings of the 4th International Workshop on Volume Graphics*, pages 167–239, 2005.

[13] R. Bajscy and S. Kovacic. Toward an Individualized Brain Atlas Elastic Matching. Technical report, University of Pennsylvania, 1986.

[14] R. Bajscy and S. Kovacic. Multiresolution Elastic Matching. *Computer Vision, Graphics, and Image Processing*, 46:1–21, 1989.

[15] R. Bajscy, R. Lieberson, and M. Reivich. A Computerized System for the Elastic Matching of Deformed Radiographic Images to Idealized Atlas Images. *Computer Assisted Tomography*, 5:618–625, 1983.

[16] S. Baker and I. Matthews. Lucas-Kanade 20 Years On: A unifying Framework. Technical report, Carnegie Mellon University, 2002.

[17] P. J. Besl and H. D. McKay. A Method for Registration of 3-D Shapes. *IEEE Transaction on Pattern Analysis and Machine*, 14(2):239–256, 1992.

[18] A. Bharatha, M. Hirose, N. Hata, S. K. Warfield, M. Ferrant, K. H. Zou, E. Suarez-Santana, J. Ruiz-Alzola, A. D'Amico, R. A. Cormack, R. Kikinis, F. A. Jolesz, and C. M. C Tempany. Evaluation of Three-Dimensional Finite Element-based Deformable Registration of Pre-and Intraoperative Prostate Imaging. *Medical Physics*, 28:2551–2560, 2001.

[19] P. Y. Bondiau, G. Malandain, S. Chanalet, P. Y. Marcy, J. L. Habrand, F. Fauchon, P. Paquis, A. Courdi, O. Commowick, and I. Rutten. Atlas-based Automatic Segmentation of MR Images: Validation Study on the Brainstem in Radiotherapy Context. *International Journal of Radiation Oncology, Biology, Physics*, 61:289–298, 2005.

[20] M. Bro-Nielsen. *Medical Image Registration and Surgery Simulation.* PhD thesis, Technical University of Denmark, 1996.

[21] M. Bro-Nielsen and S. Cotin. Real-time Volumetric Deformable Models for Surgery Simulation using Finite Elements and Condensation. *Proceedings of the Computer Graphics Forum*, 15:57–66, 1996.

[22] M. Bro-Nielsen, H. T. M. Inc, and M. D. Rockville. Finite Element Modeling in Surgery Simulation. *Proceedings of the IEEE*, 86:490–503, 1998.

[23] K. K. Brock, M. B. Sharpe, L. A. Dawson, S. M. Kim, and D. A. Jaffray. Accuracy of Finite Element Model-based Multi-Organ Deformable Image Registration. *Medical Physics*, 32:1647–1659, 2005.

[24] C. Broit. *Optimal Registration of Deformed Images.* PhD thesis, University of Pennsylvania, 1981.

[25] V. A. Cardenas, A. L. Boxer, L. L. Chao, M. L. Gorno-Tempini, B. L. Miller, M. W. Weiner, and C. Studholme. Deformation-Based Morphometry Reveals Brain Atrophy in Frontotemporal Dementiae. *Archives of Neurology*, 64(6):873–877, 2007.

[26] V. A. Cardenas, C. Studholme, S. Gazdzinski, T. C. Durazzo, and D. J. Meyerhoff. Deformation-based Morphometry of Brain Changes in Alcohol Dependence and Abstinence. *NeuroImage*, 34(3):879–887, 2007.

[27] Y. Chen and G. Medioni. Object Modeling by Registration of Multiple Range Images. *Proceedings of IEEE International Conference on Robotics and Automation, 1991*, 3(9–11):2724–2729, 1991.

[28] S. W. Cheng, T. K. Dey, H. Edelsbrunner, M. A. Facello, and S. H. Teng. Silver Exudation. *ACM*, 47(5):883–904, 2000.

[29] L. P. Chew. Constrained Delaunay Triangulations. *Algorithmica*, 4(1):97–108, 1989.

[30] Z. H. Cho, J. P. Jones, and M. Singh. *Foundations of Medical Imaging*. Wiley-Interscience, 1993.

[31] G. E. Christensen. *Deformable Shape Models for Anatomy*. PhD thesis, Washington University, 1994.

[32] G. E. Christensen, M. I. Miller, and M. Vannier. Synthesis of an Individualized Cranial Atlas with Dysmorphic Shape. *Proceedings of the Workshop of Mathematical Methods in Biomedical Image Analysis, 1996*, pages 309–318, 1996.

[33] P. G. Ciarlet. *Mathematical Elasticity, Volume I*. Studies in Mathematics and its Applications. Elsevier, 1988.

[34] O. Commowick, R. Stefanescu, P. Fillard, V. Arsigny, N. Ayache, X. Pennec, and G. Malandain. Incorporating Statistical Measures of Anatomical Variability in Atlas-to-Subject Registration for Conformal Brain Radiotherapy. *Proceedings of the 8th International Conference on Medical Image Computing and Computer-Assisted Intervention (LNCS)*, 3750:927–934, 2005.

[35] T. F. Cootes, G. J. Edwards, and C. J. Taylor. Active Appearance Models. *Proceedings of the 5th European Conference on Computer Vision (LNCS)*, 1407:484–498, 1998.

[36] T. F. Cootes, C. J. Taylor, D. H. Cooper, and J. Graham. Active Shape Models – Their Training and Application. *Computer Vision and Image Understanding*, 61(1):38–59, 1995.

[37] T. F. Cootes, C. J. Twinning, and C. J. Taylor. Diffeomorphic Statistical Shape Models . *Proocedings of the 15th British Machine Vision Conference*, 1:447–456, 2004.

[38] R. Courant. Variational Methods for Solution of Equilibrium and Vibration. *Bulletin of the American Mathematical Society*, 49:1–43, 1943.

[39] Danish Crown. The Danish Crown product catalog. `http://www.danishcrown.com/page11358.aspx`.

[40] W. R. Crum, R. I. Scahill, and N. C. Fox. Automated Hippocampal Segmentation by Regional Fluid Registration of Serial MRI: Validation and Application in Alzheimer's Disease. *Neuroimage*, 13(5):847–855, 2001.

[41] A. Cuzol, P. Hellier, and E. Mémin. A Novel Parametric Method for Non-Rigid Image Registration. *Proceedings of Information Processing in Medical Imaging, 2005 (LNCS)*, 3565:456–467, 2005.

[42] P. A. Dabnichki, A. D. Crocombe, and S. C. Hughes. Deformation and Stress Analysis of Supported Buttock Contact. *Proceedings of the Institution of Mechanical Engineers*, 208:9–17, 1994.

[43] E. d'Agostino, F. Maes, D. Vandermeulen, and P. Suetens. A Viscous Fluid Model for Multimodal Non-Rigid Image Registration using Mutual Information. *Medical Image Analysis*, 7(4):565–575, 2003.

[44] E. d'Agostino, F. Maes, D. Vandermeulen, and P. Suetens. Non-rigid Atlas-to-Image Registration by Minimization of Class-Conditional Image Entropy. *Proceedings of the 7th International Conference on Medical Image Computing and Computer-Assisted Intervention (LNCS)*, 3216:745–753, 2004.

[45] S. Darkner, M. Vester-Christensen, R. Larsen, and C. Nielsen. Automated 3D Rigid Registration of Open 2D Manifolds. *Proceedings of the 9th International Conference on Medical Image Computing and Computer-Assisted Interventation, Workshop: From Statistical Atlases to Personalized Models*, pages 19–22, 2006.

[46] R. H. Davies, C. J. Twining, T. F. Cootes, J. Waterton, and C. J. Taylor. A Minimum Description Length Approach to Statistical Shape Modelling. *IEEE Transactions on Medical Imaging*, 21(5):525–537, 2002.

[47] S. De, Y .J. Lim, M. Manivannan, and M. A. Srinivasan. Physically Realistic Virtual Surgery Using the Point-Associated Finite Field (PAFF) Approach. *PRESENCE: Teleoperators and Virtual Environments*, 15(3):294–308, 2006.

[48] M. de Bruijne, M. T. Lund, L. B. Tankó, P. C. Pettersen, and M. Nielsen. Quantitative Vertebral Morphometry using Neighbor-Conditional Shape Models. *Medical Image Analysis*, 11(5):503–512, 2007.

[49] P. F. D. D'Haese, V. Duay, R. Li, A. B. d'Aische, T. E. Merchant, A. J. Cmelak, E. F. Donnelly, K. J. Niermann, B. M. Macq, and B. M. Dawant. Automatic Segmentation of Brain Structures for Radiation Therapy Planning. *Proceedings of SPIE Medical Imaging 2003: Image Processing*, 5032:517–526, 2003.

[50] E. H. Dill. *Continuum Mechanics: Elasticity, Plasticity, Viscoelasticity.* CRC Press, 2006.

[51] I. L. Dryden and K. V. Mardia. *Statistical Shape Analysis.* Wiley, 1998.

[52] H. Edelsbrunner and D. Guoy. An Experimental Study of Sliver Exudation. *Engineering with Computers*, 18(3):229–240, 2002.

[53] J. Ehrhardt, H. Handels, T. Malina, B. Strathmann, W. S. J. Plötz, and Pöppl. Atlas-based Segmentation of Bone Structures to Support the Virtual Planning of Hip Operations. *International Journal of Medical Informatics*, 64(2-3):439–447, 2001.

[54] M. Ferrant, S. K. Warfield, C. R. G. Guttmann, R. V. Mulkern, F. A. Jolesz, and R. Kikinis. 3D Image Matching Using a Finite Element Based Elastic Deformation Model. *Proceedings of the 2nd International Conference on Medical Image Computing and Computer-Assisted Intervention (LNCS)*, 1679:202–209, 1999.

[55] J. H. Ferziger and M. Perić. *Computational methods for fluid dynamics.* Springer New York, 2002.

[56] B. Fischer and J. Modersitzki. Fast Diffusion Registration. *AMS Contemporary Mathematics: Inverse Problems, Image Analysis, and Medical Imaging*, 313:117–129, 2002.

[57] A.W. Fitzgibbon. Robust Registration of 2D and 3D Point Sets. *Proceedings of the British Machine Vision Conference*, 2:411–420, 2001.

[58] T. P. Fletcher, C. Lu, S. M. Pizer, and S. Joshi. Principal Geodesic Analysis for the Study of Nonlinear Statistics of Shape. *IEEE Transactions on Medical Image Analysis*, 23(8):995–1005, 2004.

[59] L. De Floriani and E. Puppo. An On-line Algorithm for Constrained Delaunay Triangulation. *Graphical Models and Image Processing*, 54(4):290–300, 1992.

[60] M. Fornefett, K. Rohr, and H. S. Stiehl. Elastic Registration of Medical Images using Radial Basis Functions with Compact Support. *Proceedings of the IEEE Computer Society Conference on Computer Vision and Pattern Recognition, 1999*, 1:402–407, 1999.

[61] M. Fornefett, K. Rohr, and H. S. Stiehl. Radial Basis Functions with Compact Support for Elastic Registration of Medical Images. *Image and Vision Computing*, 19(1-2):87–96, 2001.

[62] N. C. Fox, W. R. Crum, R. I. Scahill, J. M. Stevens, J. C. Janssen, and M. N. Rossor. Imaging of Onset and Progression of Alzheimer's Disease with Voxel-Compression Mapping of Serial Magnetic Resonance Images. *The Lancet*, 358(9277):201–205, 2001.

[63] P. A. Freeborough and N. C. Fox. Modeling Brain Deformations in Alzheimer Disease by Fluid Registration of Serial 3D MR Images. *Computer Assisted Tomography*, 22(5):838–843, 1998.

[64] A. Fuchs. Automatic Grid Generation with Almost Regular Delaunay Tetrahedra. *Proceedings of the 7th International Meshing Roundtable*, pages 133–147, 1998.

[65] T. Gaens, F. Maes, D. Vandermeulen, and P. Suetens. Non-rigid Multimodal Image Registration Using Mutual Information. *Proceedings of the 1st International Conference on Medical Image Computing and Computer-Assisted Interventation (LNCS)*, 1496:1099–1106, 1998.

[66] D. T. Gering, A. Nabavi, R. Kikinis, N. Hata, L. J. O'Donnell, W. E. L. Grimson, F. A. Jolesz, P. M. Black, and W. M. Wells III. An Integrated Visualization System for Surgical Planning and Guidance Using Image Fusion and an Open MR. *Magnetic Resonance Imaging*, 13(6):967–975, 2001.

[67] J. C. Gower. Generalized Procrustes Analysis. *Psychometrika*, 1975.

[68] S. Granger and X. Pennec. Multi-scale EM-ICP: A Fast and Robust Approach for Surface Registration. *Proceedings of the 7th European Conference on Computer Vision (LNCS)*, 2353:69–73, 2002.

[69] S. Grosskopf and P. S. Neugebauer. Fitting Geometrical Deformable Models to Registered Range Images. *Proceedings of the European Workshop on 3D Structure from Multiple Images of Large-Scale Environments*, pages 266–274, 1998.

[70] B. Guo and I. Babuška. The HP Version of the Finite Element Method. *Computational Mechanics*, 1(1):21–41, 1986.

[71] E. Haber and J. Modersitzki. Numerical Methods for Volume Preserving Image Registration. *Inverse Problems*, 20(5):1621–1638, 2004.

[72] E. Haber and J. Modersitzki. A Multilevel Method for Image Registration. *SIAM Journal on Scientific Computing*, 27(5):1594–1607, 2006.

[73] E. Haber and J. Modersitzki. Intensity Gradient Based Registration and Fusion of Multi-Modal Images. *Proceedings of the 9th International Conference on Medical Image Computing and Computer-Assisted Intervention (LNCS)*, 4191:726–733, 2006.

[74] M. F. Hansen. Quality Estimation and Segmentation of Pig Backs. Master's thesis, Technical University of Denmark, 2005.

[75] M. F. Hansen, M. R. Blas, and R. Larsen. Mahalanobis Distance based Iterative Closest Point. *Proceedings of SPIE Medical Imaging 2007: Image Processing*, 6512, 2007.

[76] M. F. Hansen, J. A. Bærentzen, and R. Larsen. Generating Quality Tetrahedral Meshes from Binary Volumes. *Proceedings of the International Conference on Computer Vision and Applications, 2009*, 2009.

[77] M. S. Hansen, B. Glocker, N. Navab, and R. Larsen. Adaptive Parametrization of Multivariate B-splines for Image Registration. *Proceedings of the IEEE Computer Society Conference on Computer Vision and Pattern Recognition, 2009*, 2009.

[78] M. S. Hansen, M. F. Hansen, and R. Larsen. Diffeomorphic Statistical Deformation Models. *Proceedings of the 11th International Conference on Computer Vision Workshop: Non-rigid Registration and Tracking through Learning*, pages 1–8, 2007.

[79] T. Hastie, R. Tibshirani, and J. Friedman. *The elements of statistical learning*. Springer, 2001.

[80] D. L. Hill, D. J. Hawkes, M. J. Gleeson, T. C. Cox, A. J. Strong, W. L. Wong, C. F. Ruff, N. D. Kitchen, D. G. Thomas, and A. Sofat. Accurate Frameless Registration of MR and CT Images of the Head: Applications in Planning Surgery and Radiation Therapy. *Radiology*, 191(2):447–454, 1994.

[81] T. Hu. *Reality-based Soft Tissue Probing: Experiments and Computational Model for Application to Minimally Invasive Surgery*. PhD thesis, Drexel University, 2006.

[82] S. Joshi, B. Davis, M. Jomier, and G. Gerig. Unbiased Diffeomorphic Atlas Construction for Computational Anatomy. *Neuroimage*, 23:151–160, 2004.

[83] G. E. Karniadakis and S. J. Sherwin. *Spectral/HP Element Methods for CFD*. Oxford University Press, 1999.

[84] D. G. Kendall. *Shape and Shape Theory*. Wiley, 1999.

[85] R. G. Keys. Cubic Convolution Interpolation for Digital Image Processing. *IEEE Transactions on Acoustics Speech and Signal Processing*, 29(6):1153–1160, 1981.

[86] S. J. Kiebel, J. Ashburner, J. B. Poline, and K. J. Friston. MRI and PET Coregistration - A Cross Validation of Statistical Parametric Mapping and Automated Image Registration. *Neuroimage*, 5(4):271–279, 1997.

[87] N. C. Kjærsgaard. *Optimization of the Raw Material Use at Danish Slaughterhouses*. PhD thesis, Technical University of Denmark, 2008.

[88] L. P. Kobbelt, J. Vorsatz, U. Labsik, and H. P. Seidel. A Shrink Wrapping Approach to Remeshing Polygonal Surfaces. *Computer Graphics Forum*, 18:119–130, 1999.

[89] R. M. Koch, M. H. Gross, F. R. Carls, D. F. von Büren, G. Fankhauser, and Y. I. H. Parish. Simulating Facial Surgery using Finite Element Models. *Proceedings of the 23rd annual conference on Computer graphics and interactive techniques*, pages 421–428, 1996.

[90] U. Kühnapfel, H. K. Çakmak, and H. Maaß. Endoscopic Surgery Training using Virtual Reality and Deformable Tissue Simulation. *Computers & Graphics*, 24(5):671–682, 2000.

[91] J. Kybic. *Elastic Image Registration using Parametric Deformation Models*. PhD thesis, Swiss Federal Institute of Technology, 2001.

[92] J. Kybic and M. Unser. Fast parametric elastic image registration. *IEEE Transactions on Image Processing*, 12(11):1427–1442, 2003.

[93] D. Laroche, S. Delorme, T. Anderson, and R. Diraddo. In-Vivo Validation of a Stent Implantation Numerical Model. *Studies in Health Technology and Informatics*, 125:265–70, 2007.

[94] S. Lee, G. Wolberg, K. Y. Chwa, and S. Y. Shin. Image Metamorphosis with Scattered Feature Constraints. *IEEE Transactions Visualization and Computer Graphics*, 2(4):337–354, 1996.

[95] D. Lim, F. Lin, R. Hendrix, and M. Makhsous. Finite Element Analysis for Evaluation of Internal Mechanical Responses in Buttock Structure in a True Sitting Posture: Development and Validation. *Proceedings of the 29th International conference on Rehabilitation Engineering and Assistive Technology Society of North America*, pages 22–26, 2006.

[96] T. Lindeberg. Scale-space for discrete signals. *IEEE Transactions on Pattern Analysis and Machine Intelligence*, 12(3):234–254, 1990.

[97] T. Lindeberg. *Scale-Space Theory in Computer Vision*. Kluwer, 1994.

[98] M. Lorenzo-Valdes, G. I. Sanchez-Ortiz, R. Mohiaddin, and D. Rueckert. Atlas-Based Segmentation and Tracking of 3D Cardiac MR Images Using Non-rigid Registration. *Proceedings of the 5th International Conference on Medical Image Computing and Computer-Assisted Intervention (LNCS)*, 2488:642–650, 2002.

[99] K. Madsen, H. B. Nielsen, and O. Tingleff. Optimization with Constraints. Technical report, Technical university of Denmark, 2004.

[100] F. Maes, A. Collignon, D. Vandermeulen, G. Marchal, and P. Suetens. Multimodality Image Registration by Maximization of Mutual Information. *IEEE Transactions on Medical Imaging*, 16(2):187–198, 1997.

[101] J. A. Maldjian, P. J. Laurienti, R. A. Kraft, and J. H. Burdette. An Automated Method for Neuroanatomic and Cytoarchitectonic Atlas-based Interrogation of fMRI Data Sets. *Neuroimage*, 19(3):1233–1239, 2003.

[102] S. Marsland, C. J. Twining, and C. J. Taylor. Groupwise Non-rigid Registration Using Polyharmonic Clamped-Plate Splines. *Proceedings of the 6th International Conference on Medical Image Computing and Computer-Assisted Interventation (LNCS)*, 2879:771–779, 2003.

[103] G. Matheron. *Traité de géostatistique appliquée*, volume 1. Editions Technip, 1962.

[104] J. C. Mazziotta, A. W. Toga, A. Evans, P. Fox, and J. Lancaster. A Probabilistic Atlas of the Human Brain: Theory and Rationale for Its Development The International Consortium for Brain Mapping (ICBM). *Neuroimage*, 2:89–101, 1995.

[105] T. McInerney and D. Terzopoulos. Deformable Models in Medical Image Analysis: A survey. *Medical Image Analysis*, 1(2):91–108, 1996.

[106] H. P. Meinzer, P. Schemmer, M. Schobinger, M. Nolden, T. Heimann, B. Yalcin, G. M. Richter, T. Kraus, M. W. Buchler, and M. Thorn. Computer-based Surgery Planning for Living Liver Donation. *International archives of photogrametry remote sensing and spatial information sciences*, 35(5):291–295, 2004.

[107] Merriam-Webster. *The Merriam-Webster Dictionary*. Merriam-Webster, 2006.

[108] J. Modersitzki. *Numerical Methods for Image Registration*. Oxford University Press, 2004.

[109] N. Molino, R. Bridson, J. Teran, and R. Fedkiw. A Crystalline, Red Green Strategy for Meshing Highly Deformable Objects with Tetrahedra. *Proceedings of the 12th International Meshing Roundtable*, pages 103–114, 2003.

[110] J. Montagnat and H. Delingette. 4D Deformable Models with Temporal Constraints: Application to 4D Cardiac Image Segmentation. *Medical Image Analysis*, 9(1):87–100, 2005.

[111] T. H. Mosbech, B. K. Ersbøll, and L. B. Christensen. Quantification and Validation of Soft Tissue Deformation. *Proceedings of SPIE Medical Imaging 2009: Image Processing Biomedical Applications in Molecular, Structural, and Functional Imaging*, 2009.

[112] C. J. Mummery, K. Patterson, C. J. Price, J. Ashburner, R. S. J. Frackowiak, and J. R. Hodges. A Voxel-based Morphometry Study of Semantic Dementia: Relationship Between Temporal Lobe Atrophy and Semantic Memory. *Annals of Neurology*, 47(1):36–45, 2000.

[113] R. Narayanan, J.A. Fessler, H. Park, and C.R. Meyer. Diffeomorphic Nonlinear Transformations: A Local Parametric Approach for Image Registration. *Proceedings of Information Processing in Medical Imaging, 2005 (LNCS)*, 3565:174–85, 2005.

[114] P. J. Neugebauer and K. Klein. Adaptive Triangulation of Objects Reconstructed from Multiple Range Images. *Proceedings of the IEEE Visualization 1997*, pages 41–44, 1997.

[115] R. W. Ogden. Large Deformation Isotropic Elasticity-On the Correlation of Theory and Experiment for Incompressible Rubberlike Solids. *Proceedings of the Royal Society of London*, 326(1567):565–584, 1972.

[116] H. Ólafsdóttir, T. A. Darvann, N. V. Herman, E. Oubel, B. K. Ersbøll, A. F. Frangi, P. Larsen, C. A. Perlyn, G. M. Morriss-Kay, and S. Kreiborg. Computational Mouse Atlases and their Application to Automatic Assessment of Craniofacial Dysmorphology Caused by the Crouzon Mutation Fgfr2. *Anatomy*, 211(1):37–52, 2007.

[117] C. W. J. Oomens, O. Bressers, E. M. H. Bosboom, C. V. C. Bouten, and D. Bader. Can Loaded Interface Characteristics Influence Strain Distributions in Muscle Adjacent to Bony Prominences? *Computer Methods in Biomechanics and Biomedical Engineering*, 6(3):171–180, 2003.

[118] C. W. J. Oomens, D. H. Van Campen, and H. J. Grootenboer. A Mixture Approach to the Mechanics of Skin. *Biomechanics*, 20(9):877–885, 1987.

[119] L. Pantoni, A. M. Basile, G. Pracucci, K. Asplund, J. Bogousslavsky, H. Chabriat, T. Erkinjuntti, F. Fazekas, J. M. Ferro, M. Hennerici, J. O'brien, P. Scheltens, M. C. Visser, L. O. Wahlund, G. Waldemar, A. Wallin, and D. Inzitari. Impact of Age-Related Cerebral White Matter Changes on the Transition to Disability - The LADIS Study: Rationale, Design and Methodology. *Neuroepidemiology*, 24(1–2):51–62, 2005.

[120] V. N. Parthasarathy, C. M. Graichen, and A. F. Hathaway. A Comparison of Tetrahedron Quality Measures. *Finite Elements in Analysis and Design*, 15(3):255–261, 1994.

[121] A. T. Patera. A Spectral Element Method for Fluid Dynamics-Laminar Flow in a Channel Expansion. *Computational Physics*, 54:468–488, 1984.

[122] X. Pennec, R. Stefanescu, V. Arsigny, P. Fillard, and N. Ayache. Riemannian Elasticity: A Statistical Regularization Framework for Nonlinear Registration. *Proceedings of the 8th International Conference on Medical Image Computing and Computer-Assisted Interventation (LNCS)*, 3750:943–950, 2005.

[123] G. Picinbono, H. Delingette, and N. Ayache. Nonlinear and Anisotropic Elastic Soft Tissue Models for Medical Simulation. *Proceedings of the IEEE International Conference on Robotics and Automation, 2001*, 2:1370–1375, 2001.

[124] R. Radovitzky and M. Ortiz. Tetrahedral Mesh Generation Based on node Insertion in Crystal Lattice Arrangements and Advancing-Front-Delaunay Triangulation. *Computer Methods in Applied Mechanics and Engineering*, 187(3-4):543–569, 2000.

[125] A. Roche, G. Malandain, X. Pennec, and N. Ayache. The Correlation Ratio as a New Similarity Measure for Multimodal Image Registration. *Proceedings of the First International Conference on Medical Image Computing and Computer-Assisted Intervention (LNCS)*, 1496:1115–1124, 1998.

[126] G. K. Rohde, A. Aldroubi, and B. M. Dawant. The Adaptive Bases Algorithm for Intensity-based Nonrigid Image Registration. *IEEE Transactions on Medical Imaging*, 22(11):1470–1479, 2003.

[127] T. Rohlfing, R. Brandt, C. R. Maurer Jr, and R. Menzel. Bee Brains, B-splines and Computational Democracy: Generating an Average Shape Atlas. *Proceedings of the IEEE Workshop on Mathematical Methods in Biomedical Image Analysis*, pages 187–194, 2001.

[128] T. Rohlfing, C. R. Maurer Jr, D. A. Bluemke, and M. A. Jacobs. Volume-Preserving Nonrigid Registration of MR Breast Images using Free-Form Deformation with an Incompressibility Constraint. *IEEE Transactions on Medical Imaging*, 22(6):730–741, 2003.

[129] T. Rohlfing and C. R. Maurer. Intensity-Based Non-rigid Registration Using Adaptive Multilevel Free-Form Deformation with an Incompressibility Constraint. *Proceedings of the 4th International Conference on Medical Image Computing and Computer-Assisted Interventation (LNCS)*, 2208:111–119, 2001.

[130] T. Rohlfing, E. V. Sullivan, and A. Pfefferbaum. Deformation-based Brain Morphometry to Track the Course of Alcoholism: Differences Between Intra-Subject and Inter-Subject Analysis. *Psychiatry Research: Neuroimaging*, 146(2):157–170, 2006.

[131] F. Rousseau, O. A. Glenn, B. Iordanova, C. Rodriquez-Carranza, D. B. Vigneron, J. A. Barkovich, and C. Studholme. Registration-based Approach for Reconstruction of High-Resolution in Utero Fetal MR Brain Images. *Academic Radiology*, 13(9):1072–1081, 2006.

[132] D. Rueckert, M. J. Clarkson, D. L. G. Hill, and D. J. Hawkes. Non-rigid Registration using Higher-Order Mutual Information. *Proceedings of SPIE Medical Imaging 2000: Image Processing*, 3979, 2000.

[133] D. Rueckert, A. F. Frangi, and J. A. Schnabel. Automatic Construction of 3D Statistical Deformation Models of the Brain using Nonrigid Registration. *IEEE Transactions on Medical Imaging*, 22(8):1014–1025, 2003.

[134] D. Rueckert, C. Hayes, C. Studholme, P. Summers, M. Leach, and D. J. Hawkes. Non-rigid Registration of Breast MR Images Using Mutual Information. *Proceedings of the 1st International Conference on Medical Image Computing and Computer-Assisted Interventation (LNCS)*, 1496:1144–1152, 1998.

[135] D. Rueckert, L. I. Sonoda, C. Hayes, D. L. G. Hill, M. O. Leach, and D. J. Hawkes. Nonrigid Registration using Free-Form Deformations: Application to Breast MR Images. *IEEE Transactions on Medical Imaging*, 18(8):712–21, 1999.

[136] S. Rusinkiewicz and M. Levoy. Efficient Variants of the ICP Algorithm. *Proceedings of the 3rd International Conference on 3-D Imaging and Modeling*, pages 145–152, 2001.

[137] P. A. Sarma. Non-Linear Material Models for Tracheal Smooth Muscle Tissue. *Bio-Medical Materials and Engineering*, 13(3):235–245, 2003.

[138] R. I. Scahill, J. M. Schott, J. M. Stevens, M. N. Rossor, and N. C. Fox. Mapping the Evolution of Regional Atrophy in Alzheimer's Disease: Unbiased Analysis of Fluid-Registered Serial MRI. *Proceedings of the National Academy of Sciences, 2002*, 99:4703, 2002.

[139] J . A. Schnabel, C. Tanner, A. D. Castellano-Smith, A. Degenhard, M. O. Leach, D. R. Hose, D. L. G. Hill, and D. J. Hawkes. Validation of Nonrigid Image Registration using Finite-Element Methods: Application to Breast MR Images. *IEEE Transactions on Medical Imaging*, 22(2):238–247, 2003.

[140] J. A. Schnabel, D. Rueckert, M. Quist, J. M. Blackall, A. D. Castellano-Smith, T. Hartkens, G. P. Penney, W. A. Hall, H. Liu, C. L. Truwit, F. A. Gerritsen, D. L. G. Hill, and D. J. Hawkes. A Generic Framework for Non-rigid Registration Based on Non-uniform Multi-level Free-Form Deformations. *Proceedings of the 4th International Conference on Medical Image Computing and Computer-Assisted Interventation (LNCS)*, 2208:573–581, 2001.

[141] S. Schwartz and R. Bajscy. Three-Dimensional Elastic Matching of Ventricles. *Proceedings of the 6th annual conference and Exposition: Computer Graphics*, 3, 1985.

[142] J. R. Shewchuk. Triangle: Engineering a 2D Quality Mesh Generator and Delaunay Triangulator. *Applied Computational Geometry: Towards Geometric Engineering*, 1148:203–222, 1996.

[143] J. R. Shewchuk. Tetrahedral Mesh Generation by Delaunay Refinement. *Proceedings of the 14th annual symposium on Computational geometry*, pages 86–95, 1998.

[144] J. R. Shewchuk. Constrained Delaunay Tetrahedralizations and Provably Good Boundary Recovery. *Proceedings of the 11th International Meshing Roundtable*, pages 193–204, 2002.

[145] J. R. Shewchuk. What is a Good Linear Element? Interpolation, Conditioning, and Quality Measures. *Proceedings of the 11th International Meshing Roundtable*, pages 115–126, 2002.

[146] A. M. Siddiqui and M. Saleem. Registration of Local Deformations in Images. *Proceedings of the 2nd International Conference on Electrical Engineering, 2008*, pages 1–6, 2008.

[147] M. Sonka and J. M. Fitzpatrick. *Handbook of Medical Imaging.* SPIE Press, 2000.

[148] C. O. S. Sorzano, P. Thevenaz, and M. Unser. Elastic Registration of Biological Images using Vector-Spline Regularization. *IEEE Transactions on Biomedical Engineering*, 52(4):652–663, 2005.

[149] R. Souvenir and R. Pless. Isomap and Nonparametric Models of Image Deformation. *Proceedings of the IEEE Workshop on Motion and Video Computing, 2005.*, 2:195–200, 2005.

[150] C. Studholme, V. Cardenas, R. Blumenfeld, N. Schuff, H. J. Rosen, B. Miller, and M. Weiner. Deformation Tensor Morphometry of Semantic Dementia with Quantitative Validation. *Neuroimage*, 21(4):1387–1398, 2004.

[151] C. Studholme, R. T. Constable, and J. S. Duncan. Accurate Alignment of Functional EPI Data to Anatomical MRI using A physics-based Distortion Model. *IEEE Transactions on Medical Imaging*, 19(11):1115–1127, 2000.

[152] C. Studholme, C. Drapaca, B. Iordanova, and V. Cardenas. Deformation-based Mapping of Volume Change from Serial Brain MRI in the Presence of Local Tissue Contrast Change. *IEEE Transactions on Medical Imaging*, 25(5):626–639, 2006.

[153] C. Studholme, D. L. G. Hill, and D. J. Hawkes. Automated 3-D Registration of MR and CT Images of the Head. *Medical Image Analysis*, 1(2):163–175, 1996.

[154] C. Studholme, D. L. G. Hill, and D. J. Hawkes. An Overlap Invariant Entropy Measure of 3D Medical Image Alignment. *Pattern Recognition*, 32(1):71–86, 1999.

[155] C. Studholme, E. Novotny, I. G. Zubal, and J. S. Duncan. Estimating Tissue Deformation between Functional Images Induced by Intracranial Electrode Implantation Using Anatomical MRI. *Neuroimage*, 13(4):561–576, 2001.

[156] Q. Sun, F. Lin, S. Al-Saeede, L. Ruberte, E. Nam, R. Hendrix, and M. Makhsous. Finite Element Modeling of Human Buttock-Thigh Tissue in a Seated Posture. *Proceedings of the 2005 Summer Bioengineering Conference*, pages 22–26, 2005.

[157] N. Suzuki, A. Hattori, T. Ezumi, A. Uchiyama, T. Kumano, A. Ikemoto, Y. Adachi, and A. Takatsu. Simulator for Virtual Surgery using Deformable Organ Models and Force Feedback System. *Studies in Health Technology and Informatics*, 50:227–233, 1998.

[158] M. Tada, N .Nagai, and T .Maeno. Material Properties Estimation of Layered Soft Tissue Based on MR Observation and Iterative FE Simulation. *Proceedings of the 8th International Conference on Medical Image Computing and Computer-Assisted Intervention (LNCS)*, 3750:633–40, 2005.

[159] C. Tanner, J. A. Schnabel, A. Degenhard, A. D. Castellano-Smith, C. Hayes, M. O. Leach, D. R. Hose, D. L. G. Hill., and D. J. Hawkes. Validation of Volume-Preserving Non-rigid Registration: Application to Contrast-Enhanced MR-Mammography. *Proceedings of the 5th International Conference on Medical Image Computing and Computer-Assisted Intervention (LNCS)*, 2488:307–314, 2002.

[160] SFK Technology. AutoFom: Fully Automatic Ultrasonic Carcass Grading for Pork Slaughterhouses. Technical report, SFK Technology, 2009.

[161] C. Then, J. Menger, G. Benderoth, M. Alizadeh, T. J. Vogl, F. Hübner, and G. Silber. A Method for a Mechanical Characterisation of Human Gluteal Tissue. *Technology and Health Care*, 15(6):385–398, 2007.

[162] P. Thevenaz and M. Unser. Optimization of Mutual Information for Multiresolution Image Registration. *IEEE Transactions on Image Processing*, 9(12):2083–2099, 2000.

[163] J. P. Thirion. Image Matching as a Diffusion Process: An Analogy with Maxwell's Demons. *Medical Image Analysis*, 2(3):243–260, 1998.

[164] P. M. Thompson, R. P. Woods, M. S. Mega, and A. W. Toga. Mathematical/Computational Challenges in Creating Deformable and Probabilistic Atlases of the Human Brain. *Human Brain Mapping*, 9(2):81–92, 2000.

[165] T. Vercauteren, X. Pennec, A. Perchant, and N. Ayache. Non-parametric Diffeomorphic Image Registration with the Demons Algorithm. *Proceedings of the 10th International Conference on Medical Image Computing and Computer-Assisted Intervention (LNCS)*, 4792:319–326, 2007.

[166] M. Vester-Christensen, S. G. Erbou, S. Darkner, and R. Larsen. Accelerated 3D Image Registration. *Proceedings of SPIE Medical Imaging 2007: Image Processing*, 6512, 2007.

[167] M. Vester-Christensen, S. G. H. Erbou, M. F. Hansen, E. V. Olsen, L. B. Christensen, M. Hviid, B. K. Ersbøll, and R. Larsen. Virtual Dissection of Pig Carcasses. *Meat Sciences*, 81:699–704, 2008.

[168] M. Vester-Christension. *Image Registration and Optimization in the Virtual Slaughterhouse*. PhD thesis, Technical University of Denmark, 2008.

[169] P. Viola and W. M. Wells. Alignment by Maximization of Mutual Information. *International Journal of Computer Vision*, 24(2):137–154, 1997.

[170] P. A. Viola. Alignment by Maximization of Mutual Information. Technical report, Massachusetts Institute of Technology, 1995.

[171] G. Wahba. *Spline Models for Observational Data*. CBMS-NSF Regional Conference Series in Applied Mathematics, 1990.

[172] N. P. Weatherhill and O. Hassan. Efficient Three-Dimensional Delaunay Triangulation with Automatic Point Creation and Imposed Boundary Constraints. *International journal for numerical methods in engineering*, 37(12):2005–2039, 1994.

[173] St. Weiss, M. Bajka, A. Nava, E. Mazza, and P. Niederer. A Finite Element Model for the Simulation of Hydrometra. *Technology and Health Care*, 12(3):259–267, 2004.

[174] W .M. Wells, P. Viola, H. Atsumi, S. Nakajima, and R. Kikinis. Multimodal Volume Registration by Maximization of Mutual Information. *Medical Image Analysis*, 1(1):35–51, 1996.

[175] M. Wierzbicki and T. M. Peters. Determining Epicardial Surface Motion Using Elastic Registration: Towards Virtual Reality Guidance of Minimally Invasive Cardiac Interventions. *Proceedings of the 6th International Conference on Medical Image Computing and Computer-Assisted Interventation (LNCS)*, 2878:722–729, 2003.

[176] Z. J. Wood, P. Schroder, D. Breen, and M. Desbrun. Semi-Regular Mesh Extraction from Volumes. *Proceedings of the IEEE Visualization 2000*, pages 275–282, 2000.

[177] R. P. Woods. Characterizing Volume and Surface Deformations in an Atlas Framework: Theory, Applications, and Implementation. *Neuroimage*, 18(3):769–788, 2003.

[178] R. P. Woods, S. T. Grafton, C. J. Holmes, S. R. Cherry, and J. C. Mazziotta. Automated Image Registration: I. General Methods and Intrasubject, Intramodality Validation. *Computer Assisted Tomography*, 22(1):139–152, 1998.

[179] O. C. Zienkiewicz and R. L. Taylor. *The Finite Element Method*. Butterworth-Heinemann, 2000.